J Therm Spray Tech (2019) 28:1789–1850
https://doi.org/10.1007/s11666-019-00939-0

REVIEW

# Advances in Corrosion-Resistant Thermal Spray Coatings for Renewable Energy Power Plants: Part II—Effect of Environment and Outlook

**Esmaeil Sadeghi**[1] · **Nicolaie Markocsan**[1] · **Shrikant Joshi**[1]

Submitted: 18 June 2019 / in revised form: 19 September 2019 / Published online: 13 November 2019


**Abstract** High-temperature corrosion of critical components such as water walls and superheater tubes in biomass/waste-fired boilers is a major challenge. A dense and defect-free thermal spray coating has been shown to be promising to achieve a high electrical/thermal efficiency in power plants. The field of thermal spraying and quality of coatings have been progressively evolving; therefore, a critical assessment of our understanding of the efficacy of coatings in increasingly aggressive operating environments of the power plants can be highly educative. The effects of composition and microstructure on high-temperature corrosion behavior of the coatings were discussed in the first part of the review. The present paper that is the second part of the review covers the emerging research field of performance assessment of thermal spray coatings in harsh corrosion-prone environments and provides a comprehensive overview of the underlying high-temperature corrosion mechanisms that lead to the damage of exposed coatings. The application of contemporary analytical methods for better understanding of the behavior of corrosion-resistant coatings is also discussed. A discussion based on an exhaustive review of the literature provides an unbiased commentary on the advanced accomplishments and some outstanding issues in the field that warrant further research. An assessment of the current status of the field, the gaps in the scientific understanding, and the research needs for the expansion of thermal spray coatings for high-temperature corrosion applications is also provided.

✉ Esmaeil Sadeghi
esmaeil.sadeghi@hv.se

[1] Department of Engineering Science, University West, 461 53 Trollhättan, Sweden

**Keywords** advanced characterization · environments · high-temperature corrosion · renewable energy power plants · thermal spray coatings

## Introduction

In part II of the review, the roles of various atmospheres and substances in high-temperature corrosion of metallic coatings and the protection strategies used to make the coatings less vulnerable to high-temperature corrosion are firstly discussed in this section. Where possible, this review emphasizes quantitative understanding in a form that can be used to obtain reusable insights. Second section reviews the characterization techniques that have already been used or may be used in high-temperature coating research. The important issues associated with the different experimental approaches are identified, and the advantages and limitations are detailed while providing recommendations for their use in corrosion-resistant coating research. In third section, the opportunities for new research in the field of thermal spray coatings enabled by the recent advances in experimental methodology and scientific understanding of the underlying corrosion mechanisms are discussed.

There are review papers on different aspects of coatings, including wear (Ref 1) or erosion-corrosion performance (Ref 2), hot corrosion (Ref 3), low-temperature corrosion (Ref 4) and corrosion in supercritical boilers (Ref 5). However, there are no comprehensive reviews on the interaction between various high-temperature corrosive environments and thermal spray coatings in renewable energy power plants. The key concept behind presenting a comprehensive review of the subject is to provide the researchers in the field with a platform for the new research ideas that may stem based on the recent advances and from

the translation of recent work carried out in other fields. Indeed, the previous and current research tendencies in the field of corrosion-resistant coatings are examined, recognizing the discernible knowledge gaps and at the same time seeking to identify the subsequent advancements and research directions in the field.

## Corrosion in Boilers

As discussed in the first part of the review paper, the corrosion in the boiler is mainly caused by the interactions of chlorides, sulfates, polysulfates, and sulfides with alloying elements and their oxides, which limits the steam temperature, and accordingly, the thermal/electrical efficiency of the power plants. Owing to a large number of gaseous, solid, and even liquid compounds that are concurrently present in boilers, various competing corrosion reactions can occur simultaneously. Hence, the prediction of corrosion rates or the type of corrosion attack is challenging. Nevertheless, through a combination of simplified and controlled laboratory exposures, the significant features associated with the fireside corrosion of superheater tubes in full-scale power plants can be highlighted. Although S-containing compounds (Ref 6) may also have an impact on alloy performance, the main mechanisms associated with material failure in biomass/waste-fired boilers involve the Cl-containing compounds present in the gaseous, liquid, or solid states, which are briefly explained as follows.

### Cl-Induced Corrosion

The corrosion problems related to biomass and waste-fired boilers have been reported to be mainly caused by Cl (Ref 7-11). There are three corrosion mechanisms concerning the effect of Cl which are addressed in this review, including (1) Cl-induced active corrosion (Ref 12), (2) electrochemical (Ref 13), and (3) molten-salt-based mechanisms (Ref 14, 15).

#### *Cl-Induced Active Corrosion*

According to Nielsen (Ref 16), the level of HCl when firing biomass fuels usually ranges between 100 and 1000 ppm, whereas it is even higher during waste incineration (Ref 17). In atmospheres containing both HCl and $O_2$, accelerated corrosion has been observed and a common hypothesis is that $Cl_2$ forms according to the Deacon reaction (Eq 1) (Ref 12). This is normally a very slow reaction but could be catalyzed by an oxidized metal surface. $Cl_2$ can also be formed by a reaction between a Cl-containing salt deposit, like KCl, and a previously formed oxide scale (like $Cr_2O_3$) in the presence of $O_2$, according to Eq 2 or in the presence of $O_2$ and $H_2O$, according to Eq 3.

$$2HCl + \frac{1}{2}O_2 = Cl_2 + H_2O \qquad \Delta G_f(Cl_2) \approx 0.4\,\text{kJ/mol at } 600\,^\circ\text{C} \qquad \text{(Eq 1)}$$

$$\frac{1}{2}Cr_2O_3(s) + 2KCl(s) + \frac{5}{4}O_2(g) = K_2CrO_4(s) + Cl_2(g) \qquad \Delta G_f(K_2CrO_4) \approx 73.8\,\text{kJ/mol at } 600\,^\circ\text{C} \qquad \text{(Eq 2)}$$

$$\frac{1}{2}Cr_2O_3(s) + 2KCl(s) + \frac{3}{4}O_2(g) + H_2O(g) = K_2CrO_4(s) + 2HCl(g) \qquad \Delta G_f(K_2CrO_4) \approx 73.5\,\text{kJ/mol at } 600\,^\circ\text{C} \qquad \text{(Eq 3)}$$

It was also proposed by Lee and McNallan (Ref 18) and further investigated by Grabke and Zahs (Ref 19) that Cl-containing compounds react with the alloying elements present in the boiler components and trigger accelerated corrosion through the "Cl-induced active corrosion" (or "active corrosion") mechanism, which is schematically illustrated in Fig. 1. The $Cl_2$ sourced from the Deacon process (Eq 1) or the alkali chlorides (Eq 2 and 3) diffuses through the defects in the oxide scale (e.g., cracks and pores) toward the metal/scale interface. The formation of metal chlorides can be accelerated wherever less oxygen (i.e., a lower $O_2$ partial pressure; $pO_2$) is present. At temperatures above $\sim$ 400 °C, evaporation of the metal chlorides and their subsequent outward diffusion toward the gas phase can occur. The gaseous metal chlorides convert into oxides wherever more oxygen (i.e., higher $pO_2$) is available. The new oxides form within the cracks and pores of the existing oxide scale, leading to subsequent cracking and spallation of the oxide scale (Ref 19).

Considering the thermodynamics of the Me-Cl-O system (where Me is a metal), metal oxides are stable at high $pO_2$, while metal chlorides can be expected in the regions with low $pO_2$ (Ref 8). Chemical analyses of the corrosion products formed in oxidizing–chloridizing environments have confirmed that metal chlorides are frequently observed at the metal/deposit interface (low $pO_2$), while the outer part of the deposit (high $pO_2$) contains mainly metal oxides (Ref 20). In other words, there is an inward diffusion of $Cl_2$ through the scale and a subsequent accumulation of $Cl_2$ at the metal/deposit interface. In this proposed mechanism, the molecular $Cl_2$ must diffuse through the oxide layer, presumably through large defects such as cracks and pores. In an oxidizing–chloridizing environment, the stability of metal oxides and chlorides depends on the partial pressures of $O_2$ and $Cl_2$. At the metal/deposit interface, $pO_2$ is low and metal chlorides are stable. If the system is assumed to consist of only Ni and Cr, the metallic chlorides are formed according to Eq 4-6:

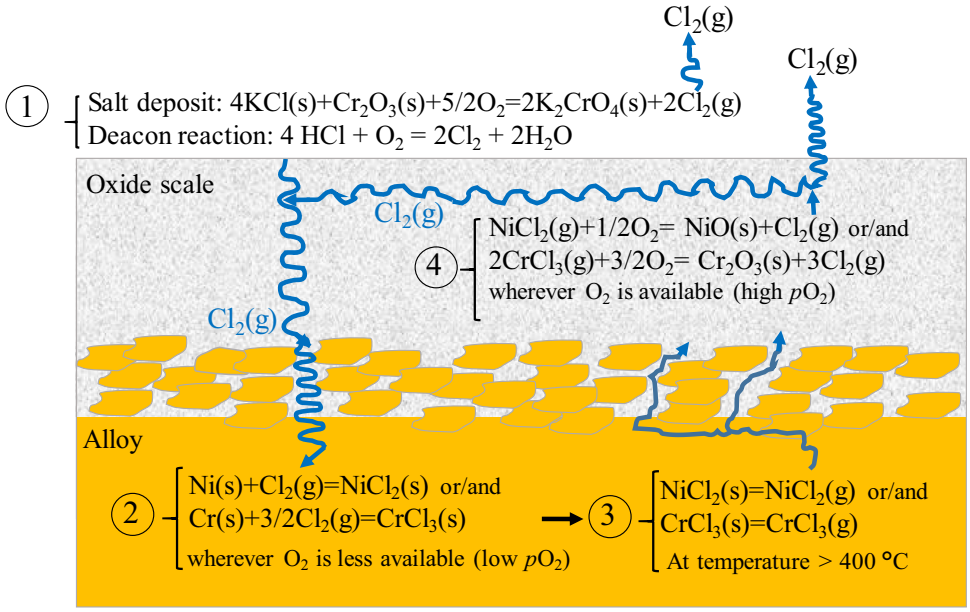


**Fig. 1** Schematic of the "Cl-induced active corrosion" mechanism in an alloy containing Ni and Cr

$$\mathrm{Ni(s) + Cl_2(g) = NiCl_2(s)} \quad \Delta G_f(\mathrm{NiCl_2}) \approx -173.9\,\mathrm{kJ/mol\ at\ 600\,^{\circ}C} \qquad \text{(Eq 4)}$$

$$\mathrm{Cr(s) + Cl_2(g) = CrCl_2(s)} \quad \Delta G_f(\mathrm{CrCl_2}) \approx -287.0\,\mathrm{kJ/mol\ at\ 600\,^{\circ}C} \qquad \text{(Eq 5)}$$

$$\mathrm{2Cr(s) + 3Cl_2(g) = 2CrCl_3(s)} \quad \Delta G_f(\mathrm{CrCl_3}) \approx -371.6\,\mathrm{kJ/mol\ at\ 600\,^{\circ}C} \qquad \text{(Eq 6)}$$

At elevated temperatures, the vapor pressures of metal chlorides can be significant and volatile chlorides (Eq 7 and 8) diffuse toward the O-rich outer part of the scale (high $pO_2$), where they are destabilized according to Eq 9 and 10 (Ref 12):

$$\mathrm{CrCl_3(s) = CrCl_3(g)} \qquad \text{(Eq 7)}$$

$$\mathrm{NiCl_2(s) = NiCl_2(g)} \qquad \text{(Eq 8)}$$

$$\mathrm{CrCl_3(g) + O_2(g) = \frac{1}{2}Cr_2O_3(s) + Cl_2(g)} \quad \Delta G_f(\mathrm{Cr_2O_3}) \approx -127.8\,\mathrm{kJ/mol\ at\ 600\,^{\circ}C} \qquad \text{(Eq 9)}$$

$$\mathrm{NiCl_2(g) + \frac{1}{2}O_2(g) = NiO(s) + Cl_2(g)} \quad \Delta G_f(\mathrm{NiO}) \approx -50.9\,\mathrm{kJ/mol\ at\ 600\,^{\circ}C} \qquad \text{(Eq 10)}$$

Although the Cl cycle is frequently used for describing the corrosion in oxidizing–chlorinating environments, there are concerns with this proposed mechanism. Folkeson et al. (Ref 21) argued that it is unlikely that a low $pO_2$ can be established at the metal/oxide interface if molecular transport is taking place. This would assume that the oxide is permeable to the bulky $Cl_2$ molecule while being impermeable to the smaller $O_2$ molecule (O–O bond length is ~ 1.48 Å and Cl–Cl bond length is ~ 1.99 Å). The initiation of corrosion, i.e., the breakdown of the Cr-rich protective oxide, which is initially present on chromia-forming alloys, cannot be explained by this mechanism. Moreover, the $Cl_2$ and $K_2CrO_4$ formed through the proposed mechanism (Eq 1-3) are not thermodynamically favored, and the reactions are non-spontaneous (Ref 22). The latter argument is still under debate, and will be discussed later.

*Electrochemical Mechanism*

In another proposed theory, known as the "electrochemical-based" mechanism (Ref 23), the transport of Cl through the oxide scale is considered to occur in the ionic form (of $Cl^-$) rather than in the molecular form (of $Cl_2$), especially during the initial stages. The corresponding anodic process at the metal/oxide interface produces outward diffusing cations (like $Cr^{2+}$). The alkali chlorides react with Cr in the protective oxide scale to form $K_2CrO_4$ during the early stages, leading to Cr-depleted oxides and breakaway oxidation. The mechanism would then be explained by HCl dissociating at the oxide scale/gas interface according to the cathodic process (Eq 11 and 12):

$$\mathrm{Cr = Cr^{2+}(oxide) + 2e^-} \qquad \text{(Eq 11)}$$

Reaction at the oxide scale surface:

$$\mathrm{\frac{1}{2}Cr_2O_3 + 2KCl(s) + \frac{5}{4}O_2(g) + 2e^- = K_2CrO_4(s) + 2Cl^-} \qquad \text{(Eq 12)}$$

After this initial step, $Cl^-$ diffuses through the oxide grain boundaries toward the metal/oxide interface via electrochemical reactions (Ref 13). At the locations within

the coating where $Cl^-$ and $Cr^{2+}$ come in contact with each other, the following reactions occur (Eq 13 and 14):

$$Cr^{2+} + Cl^- = CrCl_2(s) \quad \text{(Eq 13)}$$

$$CrCl_2(s) = CrCl_2(g) \quad \text{(Eq 14)}$$

The overall reaction (for the case of Cr oxidation) is given by Eq 15. Similar steps can be anticipated for the formation of $CrCl_3$ instead of or along with $CrCl_2$.

$$\frac{1}{4}Cr_2O_3 + 2KCl(s) + \frac{13}{8}O_2(g) + \frac{3}{2}Cr = K_2CrO_4(s) + CrCl_2(g) \quad \text{(Eq 15)}$$

$$\Delta G_f(K_2CrO_4) \approx -77.4\,\text{kJ/mol at } 600\,^\circ\text{C}$$

*Molten-Salt-Based Mechanism*

In boilers, corrosion by molten salts can be expected when low-melting compounds/mixtures are formed on the alloy surface. The experimental work of Ishitsuka and Nose (Ref 24) revealed that Fe, Ni, and Cr oxides are soluble in molten alkali chlorides and that the solubility is determined by the level of basicity and the presence of water vapor. Field exposures (Ref 25) and laboratory tests (Ref 26, 27) have identified fused $ZnCl_2$ and $PbCl_2$ as major concerns in the temperature range 300-400 °C, since these are known to have low melting points and form low-melting eutectic mixtures with other salts. During combustion, Pb and Zn may react with S and Cl to form sulfates and chlorides in the flue gases. Such compounds are of particular importance owing to the formation of low-melting (eutectic) salt mixtures. These low-melting solid or gaseous compounds can exist in the flue gases and may condense on the colder surfaces of the superheater or water wall tubes and form a corrosive product when passing through the convective parts of the boiler (Ref 27). The various compounds and eutectic mixtures that may lead to molten-salt corrosion in biomass and waste-fired boilers are summarized in Table 1 (Ref 28). In an actual boiler environment, even more complex mixtures that are not found in binary or ternary phase diagrams may be present. Although molten chlorides are more frequently encountered owing to their lower melting points, both chloride and sulfate melts can form on superheater tubes during waste incineration.

Waste wood consists of different types of wood fractions, and can also include high amounts of Pb and Zn. Pb- and Zn-containing compounds present in the ash lower the melting points of the sulfates, polysulfates, chlorides, and mixtures thereof that are present in the deposits, and can, therefore, increase the corrosion rates (Ref 30). Pb forms lead-potassium chlorides in the deposits, which are thought to corrode the furnace walls (Ref 31-33). There are two known solid Pb-K-Cl compounds, $K_2PbCl_4$ and $KPb_2Cl_5$. The former was observed during laboratory testing, whereas the latter was found in boiler heat transfer surfaces. However, the detailed formation mechanism of the Pb-K-Cl species in boiler environments is still unknown. In laboratory corrosion experiments, the interaction of $K_2SO_4$ and $PbCl_2$, leading to the formation of the caracolite-type compound $K_3Pb_2(SO_4)_3Cl$, has also been observed (Ref 32); see Eq 16. Temperature gradients may play a vital role in $PbCl_2$-induced corrosion using local melt formation and the proximity of the molten phase to the tube surface (Ref 33).

$$2PbCl_2(g/l/s) + 3K_2SO_4(s) = K_3Pb_2(SO_4)_3Cl(s) + 3KCl(g/s) \quad \text{(Eq 16)}$$

Based on laboratory studies, $ZnCl_2$ has been proven to be as corrosive as $PbCl_2$ at similar temperatures (Ref 34). However, Zn oxidizes easily in areas where corrosion has been found to be most severe (Ref 35). ZnO was found as a corrosion product but at temperatures higher than the usual furnace wall material temperatures (Ref 34). Therefore, it is assumed that the main corrosion issues encountered when firing recovered waste wood are predominantly caused by the Pb associated with Cl (Ref 36). A summary of the three corrosion mechanisms commonly proposed in Cl-containing environments is given in Fig. 2.

## Role of Water Vapor

Chromia-forming alloys usually exhibit superior corrosion resistance in dry environments at high temperatures (below 850 °C), with the protective chromia scale acting as a barrier, separating the environment and the alloy, resulting in a low oxidation rate. However, the protective properties of this oxide are usually limited when water vapor is also present in the environment. Oxidation in a water–vapor-laden environment is particularly severe in the presence of oxygen. For example, the combination of $O_2$ and water vapor has been shown to destroy this type of oxide, leading to breakaway corrosion ($pH_2O$ = 0.02-0.04 atm, which is reported to be sufficient (Ref 37) for the breakaway corrosion). Several mechanisms have been proposed to address the effect of water vapor in accelerating the corrosion, although the exact role of water vapor in accelerating the corrosion attack is still debated. A couple of explanations given in the literature are enumerated as follows:

1. Dissociation mechanism (and bridge mechanism): formation of $O_2$ through $H_2O = H_2 + 1/2O_2$ and its diffusion through oxide pores and cracks (Ref 38)
2. $H^+$ or $OH^-$ incorporation in the oxide (rather than the big $O^{2-}$), leading to faster oxygen diffusion (Ref 39)

**Table 1** Melting points of compounds and the low-melting mixtures expected in biomass and waste-fired boilers (Ref 29)

| Single compounds | Melting point, °C | Salt mixtures | Melting point, °C |
|---|---|---|---|
| $ZnCl_2$ | 283 | KCl-$ZnCl_2$ | 230 |
| $PbCl_2$ | 489 | NaCl-$ZnCl_2$ | 262 |
| $FeCl_2$ | 673 | KCl-$FeCl_2$ | 355 |
| $ZnSO_4$ | 730 | NaCl-$FeCl_2$ | 370 |
| KCl | 775 | $K_2SO_4$-$ZnSO_4$-$Na_2SO_4$ | 388 |
| NaCl | 801 | KCl-$PbCl_2$ | 412 |
| $CrCl_2$ | 821 | NaCl-$PbCl_2$ | 415 |
| $Na_2SO_4$ | 884 | NaCl-$CrCl_2$ | 437 |
| $NiCl_2$ | 1001 | KCl-$CrCl_2$ | 462 |
| $K_2SO_4$ | 1076 | KCl-$NiCl_2$ | 508 |
| $CaSO_4$ | 1400 | NaCl-$NiCl_2$ | 560 |
| $PbSO_4$ | 1170 | KCl-NaCl | 657 |

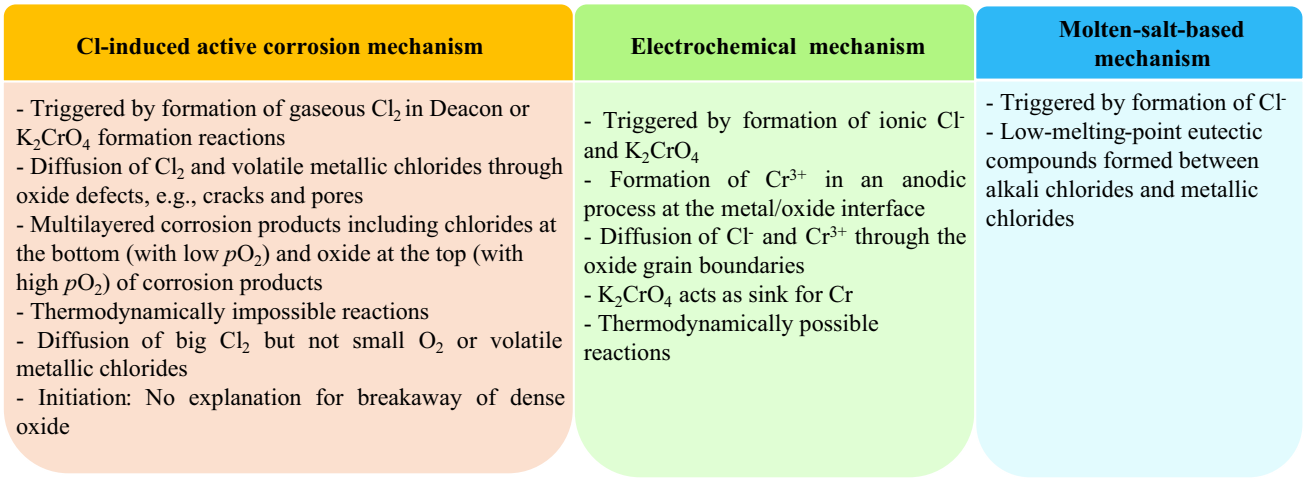


**Fig. 2** Summary of the three proposed corrosion mechanisms in Cl-containing environments

3. Vaporization mechanism: formation of volatile $Fe(OH)_3$ or $CrO_2(OH)_2$, for instance, based on $Cr_2O_3(s) + O_2(g) + H_2O(g) \rightarrow CrO_2(OH)_2(g)$ (Ref 40, 41)
4. Surface reaction mechanism, leading to preferential adsorption at inner scale surfaces (Ref 41)
5. Changes in grain size of the oxide scale (Ref 42-45)
6. Growth stress mechanism, leading to scale microcracking (Ref 46, 47)
7. Cation diffusion due to the introduction of proton defects in the scale (Ref 48)
8. Inward diffusion of $OH^-$ or $H_2O$, leading to the formation of whiskers at low $pO_2$ (Ref 49)

Most of the mechanisms presented above are derived from exposures performed in environments containing both $O_2$ and $H_2O$. Only a few studies investigated the effect of water vapor in low $O_2$ activity environments containing $H_2$ and $H_2O$ (Ref 42, 50). Torbjörn et al. (Ref 51) found that the effect of water vapor can vary depending on the availability of $O_2$ in the environment. In an $O_2$-poor condition, water serves as the main oxidant that is reduced to $OH^-$ and $H_2$ at the scale/gas interface. The $e^-$ required for this reaction is supplied by the anodic reaction (alloy corrosion). Finally, the addition of water vapor affects the transport properties of the scale. Molecular $H_2O$ may also diffuse through the oxide and reach the substrate. In an $O_2$-rich condition, $O_2$ acts as the main oxidant. Based on Wagner theory (which suggests that the surface reactions are close to equilibrium) (Ref 52), $O_2$ is cathodically reduced, whereas $H_2O$ cannot be reduced. However, in the early stages of oxidation, the Wagner theory might not be valid and $H_2O$ can be more reactive than $O_2$.

## Role of S

S does not play a vital role in biomass or WtE boilers (Ref 53). Indeed, S recirculation is a new technology for reducing corrosion and dioxin formation (highly toxic environmental persistent organic pollutants) in such boilers

(Ref 53). S is mainly found in flue gases such as $SO_2$, and most of it is transported to the flue gas for cleaning downstream. A minor fraction of S (typically a few percents) can be found in the form of $SO_3$. The direct oxidation of $SO_2$ to $SO_3$ with $O_2$ in the gas phase is thermodynamically feasible but in practice, in the conditions prevailing in large parts of an incinerator furnace/boiler system, the kinetics of this gas-phase reaction is unfavorable for a substantial amount of $SO_3$ to be formed (Ref 54). While fly ash and $Fe_2O_3$ (which can be present in the fly ash) can catalyze the conversion of $SO_2$ to $SO_3$, the conversion rates are nevertheless low. A maximum conversion of about 2% was observed at 700 °C, and the residence time was about 1 s (Ref 54). $SO_3$ can be formed alternatively through the Griffin reaction (Eq 16), in which $SO_2$ reacts with the $Cl_2$ formed through the Deacon reaction (Eq 1):

$$Cl_2(g) + H_2O(g) + SO_2(g) = 2HCl(g) + SO_3(g) \quad \text{(Eq 17)}$$

Information on the conversion rates of this reaction is, however, scarce to non-existent in the literature. The most likely option for $SO_2$ is to convert to sulfates through a gas-to-solid reaction in/on the deposits present on heat-exchanging surfaces, known as the "sulfation reaction" (Eq 17) (Ref 55):

$$2(Na, K)Cl(s) + SO_2(g) + \frac{1}{2}O_2(g) + H_2O(g) = (Na, K)_2SO_4(s) + 2HCl(g) \quad \text{(Eq 18)}$$

In more detail, $SO_2$, $O_2$, and $H_2O$ are first adsorbed on the wall deposits, where $SO_2$ can react with $O_2$. The formed $SO_3$ then reacts with adsorbed $H_2O$ to form $H_2SO_4$, which in turn reacts with the NaCl (or KCl) already present in the deposit. As a result, solid $Na_2SO_4$ and gaseous HCl are formed as the final products.

## Role of the Environment

The operating atmosphere in a boiler includes either oxidizing or reducing depending on the oxygen partial pressure ($pO_2$). An oxidizing atmosphere is a condition in which a sufficient level of oxygen is available for oxidation reactions. A reducing atmosphere is a gaseous environment with a negligible amount of oxygen, which may also contain reactive gases such as H2 or CO. Usually, reducing condition is dominant in the lower part of the boiler (near to the bed), while oxidation resulting from gas-deposit-metal reactions is important in the upper part of the boiler. In general, poor fuel balance resulting from poor fineness can result in areas of reducing atmosphere in the furnace, which results in localized areas where ash melts into a slag, due to lower melting points caused by a reducing atmosphere (Ref 56). In the next sections, the corrosion behavior of the thermal spray coatings in the two atmospheres will be discussed.

## Oxidizing Environments

### *Ambient Air With and Without a Salt Deposit*

Jafari et al. (Ref 57) and Sadeghimeresht et al. (Ref 58) studied the high-temperature corrosion of four HVAF-sprayed coatings, Ni21Cr, Ni5Al, Ni21Cr9Mo-$SiO_2$, and Ni21Cr7AlY, in ambient air environment after 168 h of exposure at 600 °C with and without a KCl deposit. While the weight gains of the coatings were almost similar in ambient air without KCl, Ni21Cr9Mo-$SiO_2$ showed the highest value; see Fig. 3(a) and (b). When KCl was introduced to the environment, the weight gain significantly increased in all the coatings, highlighting the major contribution of KCl in hastening coating failures. While the corrosion performances of the chromia-forming Ni21Cr and Ni21Cr7AlY coatings were better than that of the alumina-forming Ni5Al coating in the absence of KCl, the results showed slightly better corrosion behavior of Ni5Al in the presence of KCl. Similar to the case of exposure without KCl, Ni21Cr9Mo-$SiO_2$ exposed to KCl revealed the highest weight change, indicating the formation of more corrosion products at the surface, which can be a sign of an unacceptable corrosion performance.

Figure 3(a) shows the typical microstructure of the HVAF coatings exposed to the ambient air environment at 600 °C after 168 h. It confirms that the splat boundaries of the coating allow much rapid diffusion of the corrosive species than what can occur through the splats. For this reason, the initial oxidation at the splat boundaries is typically higher than that occurring in the core of the splats. The protectiveness of the oxide formed at the splat boundaries depends on the composition of the oxide and the extent to which it inhibits the easy inward diffusion of the corrosive species through the splat boundaries.

After the exposure in ambient air without KCl, a layer of NiO with a small content of $Al_2O_3$ was detected on Ni5Al, while $Cr_2O_3$ was the main oxide scale formed on Ni21Cr and Ni21Cr9Mo-$SiO_2$; see Table 2. The mixed oxide scale formed on the Ni21Cr7AlY coating showed the best oxidation resistance owing to the formation of the thin and slow-growing $Al_2O_3$ scale along with $Cr_2O_3$. In general, the oxidation resistance of the coatings, obtained only through kinetic studies, revealed the following order (from the smallest to the largest damage): Ni21Cr7AlY $\approx$ Ni21Cr $>$ Ni5Al $>$ Ni21Cr9Mo-$SiO_2$.

When KCl was introduced into the ambient air environment (Ref 57), Ni5Al showed a slightly lower weight change than Ni21Cr; see Fig. 3(b). The corrosion

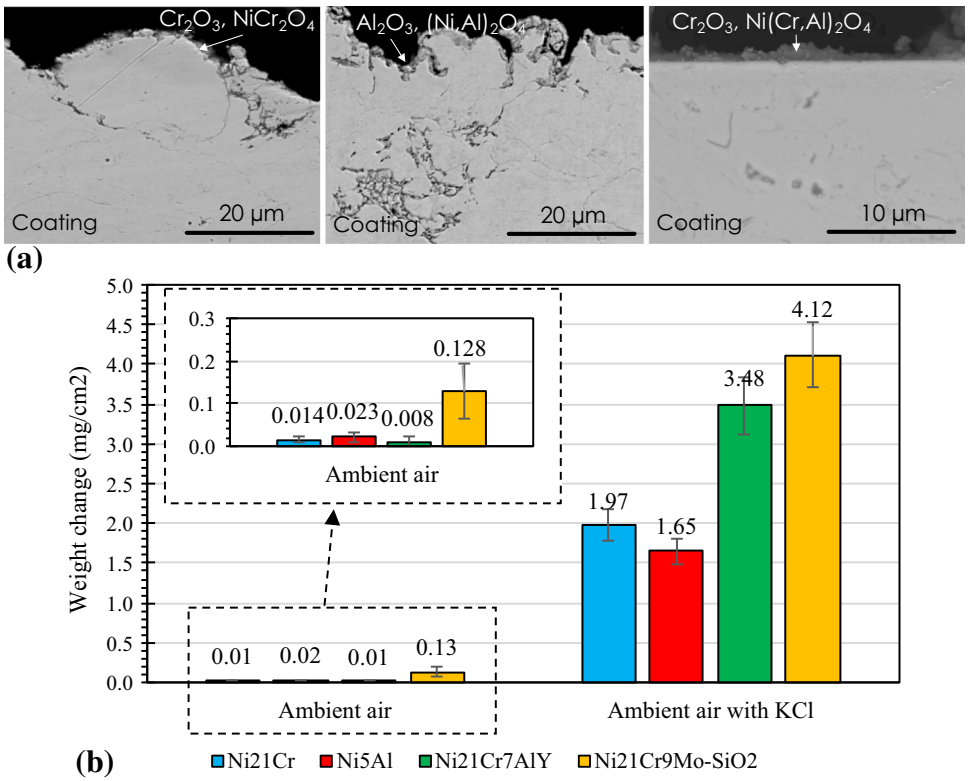


**Fig. 3** (a) Oxidation within the splat boundaries in the HVAF-sprayed Ni21Cr, Ni5Al, and Ni21Cr7AlY coatings exposed to ambient air at 600 °C for 168 h and (b) weight change in HVAF-sprayed Ni21Cr, Ni5Al, Ni21Cr7AlY, and Ni21Cr9Mo-$SiO_2$ coatings in ambient air after exposure for 168 h at 600 °C with and without KCl (Ref 57, 58). Reprinted with permission from Elsevier

performances of the coatings based on the kinetics only revealed the following order (from the highest resistance to the lowest): Ni5Al > Ni21Cr > Ni21Cr7AlY > Ni21Cr9Mo-$SiO_2$. The chromia-forming coatings were found to be prone to degradation by an "electrochemical" mechanism, in addition to the "Cl-induced active corrosion" mechanism. The exposed coatings remained attached to the substrate after the test and slowed the access of the corrosive agents to the coating/substrate interface.

Bedi et al. (Ref 59) investigated the effect of Cr addition in two HVOF-sprayed Ni-20Cr and Ni-50Cr coatings. High-temperature corrosion studies were conducted in an ambient air environment containing $Na_2SO_4$-60%$V_2O_5$ at 700 °C for 50 cycles (each cycle comprised 1 h of heating followed by 20 min of cooling). The Ni-50Cr coated substrate was found to be more successful in reducing the corrosion rate, compared to the Ni-20Cr coating, although the diffusion of Fe from the substrate to the coating was observed. Singh et al. (Ref 60) studied an HVOF-sprayed $Cr_3C_2$-25NiCr-25(WC-Co) coating; see Fig. 4. The high-temperature corrosion and oxidation behaviors of bare and coated boiler steels were investigated at 700 °C for 50 cycles in ambient air with the presence of $Na_2SO_4$-82%$Fe_2(SO_4)_3$ molten salt as a simulated boiler condition. The coating showed the ability to retain its microstructural features even after the exposures to air, molten salt, and actual boiler environments. The formation of phases, including $Cr_2O_3$, $NiCr_2O_4$, and $NiWO_4$, was reported as the reason for the best corrosion performance of the coating. Song et al. (Ref 61) studied a liquid-fueled HVOF-sprayed Ni50Cr coating deposited using three different processing parameters. Short-term (4 h) and long-term (100 h) air oxidation tests of the coatings at 700 °C showed that oxides with different morphologies formed on them. Chromia was the main corrosion product in all the three coatings. The coating with medium porosity and oxygen content showed the best oxidation performance.

**Table 2** Corrosion products formed on the surfaces of coatings exposed to ambient air for 168 h at 600 °C (Ref 57, 58)

| Coatings | Corrosion products | |
|---|---|---|
| | Without KCl | With KCl |
| Ni5Al | NiO, $Al_2O_3$ | NiO, $Al_2O_3$ |
| Ni21Cr | NiO, $Cr_2O_3$ | NiO, $NiCr_2O_4$, $Cr_2O_3$ |
| Ni21Cr7AlY | NiO, $Cr_2O_3$, $Al_2O_3$, $Ni(Al,Cr)_2O_4$ | NiO, $Cr_2O_3$, $Al_2O_3$, $NiCr_2O_4$, $NiCl_2$ |
| Ni21Cr9Mo-$SiO_2$ | NiO, $Cr_2O_3$, $MoO_3$ | NiO, $Cr_2O_3$, $NiCr_2O_4$, $MoO_3$, $K_2CrO_4$ |

Fantozzi et al. (Ref 62) studied the decomposition of carbides in HVOF- and HVAF-sprayed $Cr_3C_2$-50NiCr-MoNb coatings and its effect on their high-temperature corrosion. The two processes were used to obtain microstructures with different levels of carbide decompositions; see Fig. 5(a). Moreover, secondary carbide precipitation was induced as the coatings were also heat-treated in inert Ar atmosphere. The as-sprayed and heat-treated self-standing coatings were covered with KCl and exposed to the air environment at 550 °C for 4 and 72 h. In the initial stage of the corrosion, the actual metal binder composition was probably the corrosion rate-controlling factor. In the second stage, the formation of a network of fine secondary carbide precipitates and their fast degradation was the rate-controlling factor. It was shown that the level of carbide decomposition highly affected the corrosion resistance of the coatings; see Fig. 5(b). HVAF showed better results compared to HVOF owing to its lower spray temperature.

Jiang et al. (Ref 63) investigated Fe-based amorphous coatings on a T91 substrate by using the APS process; see Fig. 6(a). The corrosion behavior of the coating in hot $Na_2SO_4 + K_2SO_4$ salts at 700 °C was investigated. The highest hot corrosion resistance was a result of the amorphous composite microstructure and the high contents of elemental Cr and Ni, which contributed to the formation of protective oxides of Cr and Ni, such as $Cr_2O_3$, NiO, and $NiCr_2O_4$. No significant corrosion rate differences were observed in the stable stage between the coatings with thicknesses of 250 and 380 μm, suggesting that a Fe-based amorphous coating with a thickness within the range 250-380 μm can provide enough protection in the corrosive environment considered; see Fig. 6(b).

The Cl-induced high-temperature corrosion behavior of amorphous Fe-based coatings (FeCrNiMoBSiC) sprayed by the HVAF and HVOF techniques was also investigated; see Fig. 7(a) and (b) (Ref 64). The typical thermal spray coating features, e.g., splat boundaries and pores, can be seen in both the coatings. The HVAF and HVOF coatings both revealed laminar microstructures. No distinct gaps at the HVOF and HVAF coating/substrate interfaces were observed, revealing good integrity of the interfaces, which is an indication of the high adhesion of the coatings to the substrates in case of both the processes (Ref 64). The dark

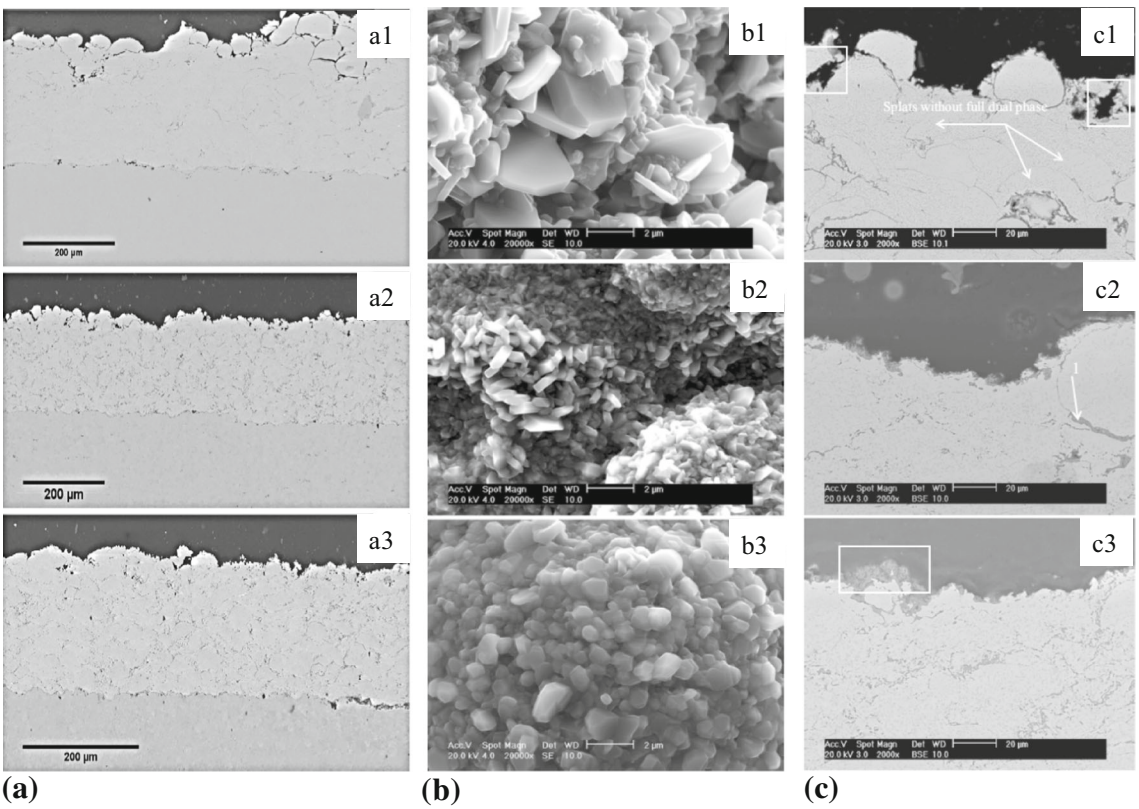


**Fig. 4** SEM images of the cross sections of coatings: (a1) coating #1; (a2) coating #2; (a3) coating #3, (b) top morphologies of (b1) coating #2; (b2) coating #3; and (b3) powder after 100-h exposure, and (c) cross sections of (c1) coating #1; (c2) coating #2; and (c3) coating #3 after 100-h exposure (Ref 61). Coating #1 was produced with oxygen flow rate of 900 l/min and kerosene flow rate of 0.4 l/min. Coating #2 was produced with oxygen flow rate of 878 l/min and kerosene flow rate of 0.445 l/min. Coating #3 was produced with oxygen flow rate of 920 l/min and kerosene flow rate of 0.47 l/min. Reprinted with permission from Elsevier

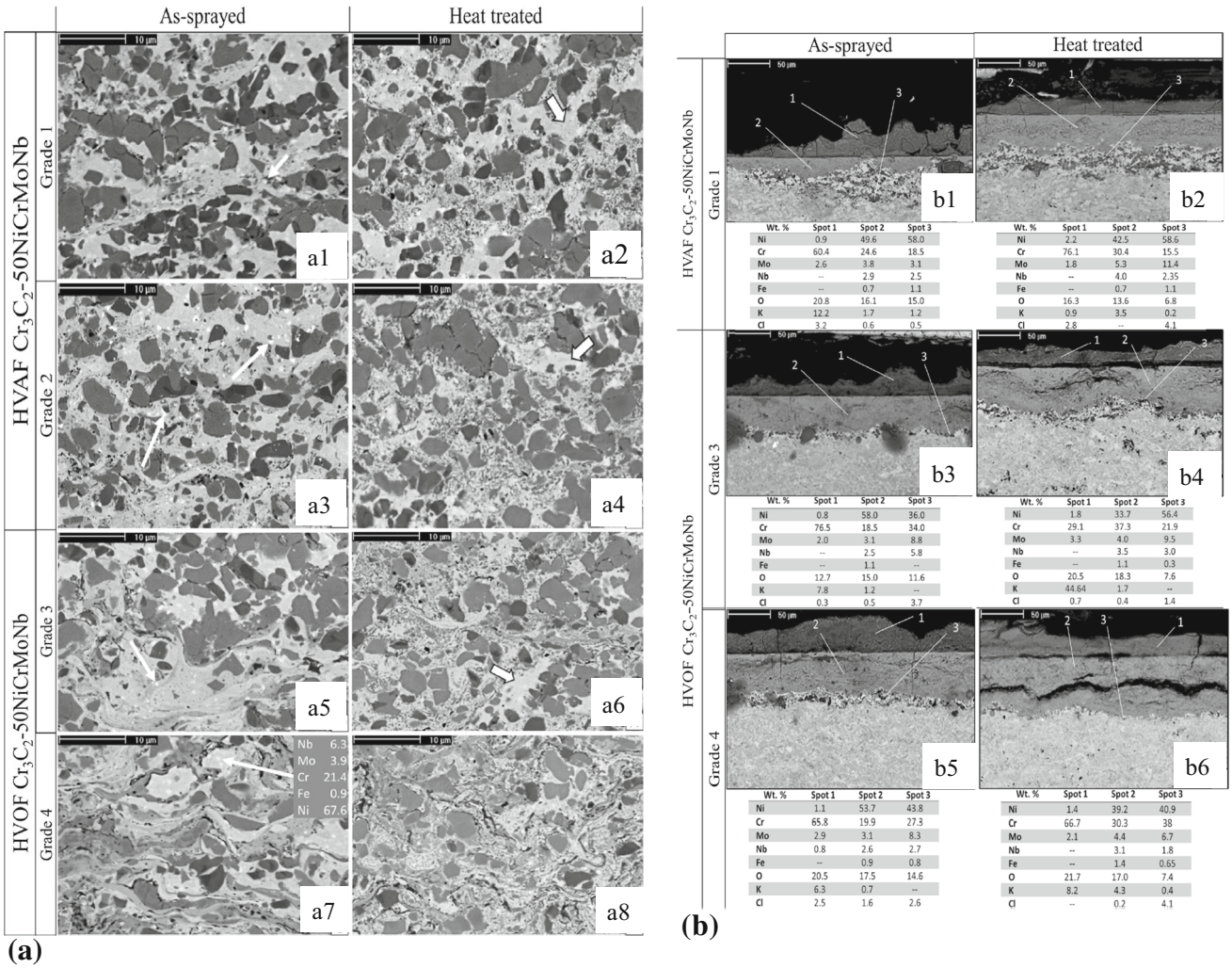


**Fig. 5** SEM (BSE) images of the cross sections of the as-sprayed [HVAF 1 (a1), HVAF 2 (a3), HVOF 3 (a5), HVOF 4 and EDX analysis of a NbC particle (a7)] and heat-treated coatings [HVAF 1 (a2), HVAF 2 (a4), HVOF 3 (a6), HVOF 4 (a8)]. The heat treatment was performed in an inert atmosphere (Ar-5 vol.% $H_2$) at 700 °C for a duration of 5 h. The thick arrows point to the areas where no precipitation was observed. The thin arrows point to the NbC particles. (b) Comparison of the corrosion fronts of the coatings after 72 h of exposure at 550 °C under KCl and 12% humidity of the air. On the left column, the HVAF 1, HVOF 3, and HVOF 4 coatings tested in the as-sprayed condition are shown (b1, b3, b5, respectively), while on the right column those obtained after heat treatment (b2, b4, b6, respectively) are presented (Ref 62). The particle size in HVAF 1, HVAF 2, HVOF 3 and HVOF 4 was 15-45, 5-30, 15-45 and 5-30 μm, respectively. Reprinted with permission from Elsevier

regions noted at the coating/substrate interface were attributed to the alumina particles embedded during grit blasting of the substrates. It was already shown that the adhesion of the coating to the substrate, which is caused by the high spray velocities of HVAF and HVOF, is not adversely affected by the presence of such grit particles (Ref 65). The microstructures of the HVAF- and HVOF-sprayed Fe-based coatings seem to be slightly affected by the ambient air environment in the absence of KCl. The oxide scales formed on both the coatings were uniform and continuous. Moreover, thin and continuous layers of the oxide scale entirely covered the surfaces of both the HVAF and HVOF coatings. The thickness of the oxide scale formed on the HVAF coating was around 1.5 μm, whereas it was about 2 μm on the exposed HVOF coating. As indicated by EDS, the scales were found to be rich in Fe, Cr, and O, indicating the formation of (Fe, Cr)-rich oxide scales. It can also be seen that mixed corrosion products with similar thicknesses of ~ 20 μm formed on the surfaces of both the HVAF and HVOF coatings. It can be clearly observed that all the coatings were affected in the presence of KCl. This type of degradation was not observed in the coatings in the absence of KCl. The weight changes (in $mg/cm^2$) in the HVAF and HVOF coatings exposed to corrosive environments with and without KCl are shown in Fig. 7(c). The results showed that higher

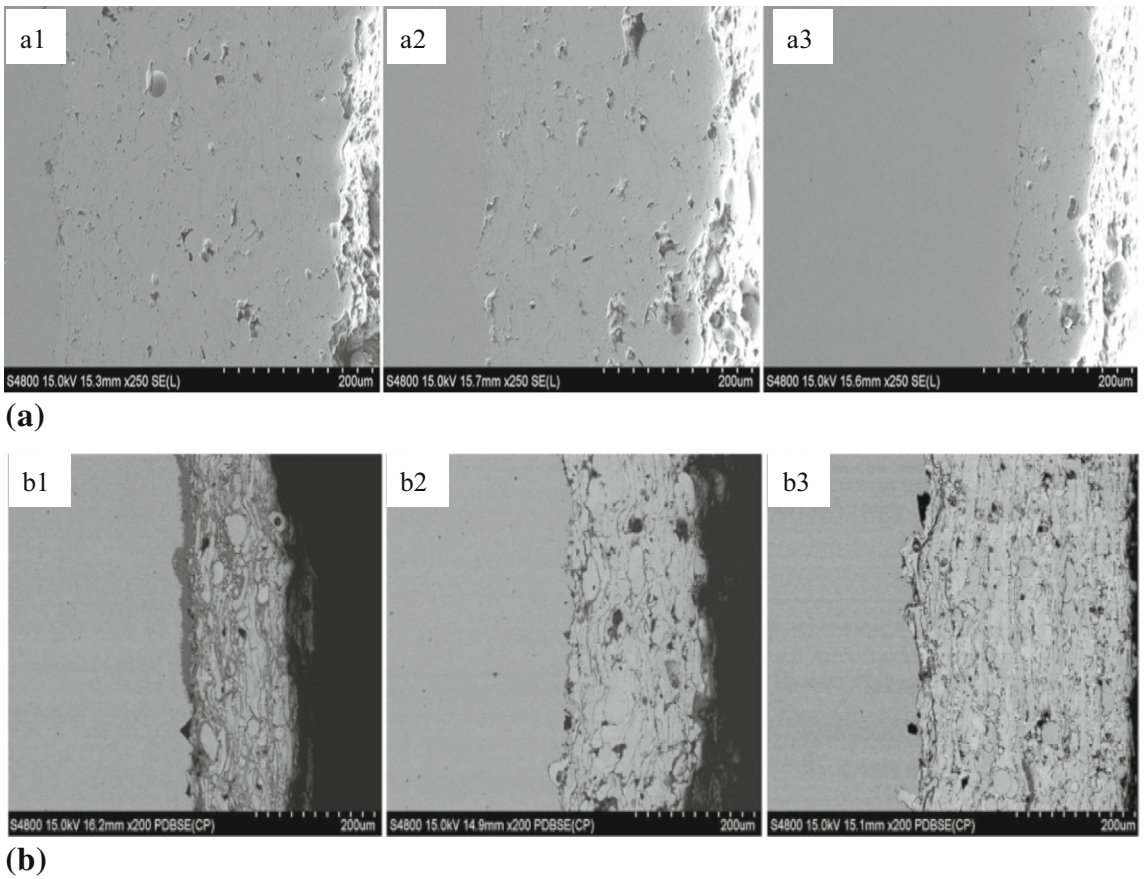


**Fig. 6** Cross-sectional microstructures of Fe-based amorphous coatings with different thicknesses: (a1) ~ 380, (a2) ~ 270, (a3) ~ 100 μm, and (b) SEM cross-sectional images of the coatings of different thicknesses after hot corrosion: (b1) ~ 100, (b2) ~ 270, (b3) ~ 380 μm (Ref 63). Reprinted with permission from Elsevier

weight gains were recorded in the presence of KCl for both the coatings, reflecting the substantial effect of KCl on corrosion damage. The weight gains of both the coatings followed similar trends in the absence of KCl. In the case of exposure without KCl, the rates of weight gain increased during the early stages and then reduced as the exposure time increased. The HVAF coating showed a lower weight change in the presence or absence of KCl compared to the HVOF coating, indicating that the former was probably more successful in combating corrosion. The weight of the HVOF coating exposed to KCl showed a significant loss upon increasing the exposure time from 96 to 168 h, while the weight loss was less for the HVAF coating.

In general, when a coating is exposed to a simple oxidizing environment such as ambient air, an oxide film of chromia or alumina (depending on the coating composition) forms that thickens on the coating surface and progressively isolates the coating from its environment. The corrosion mechanism in ambient air environment containing $O_2$ is as follows: (1) absorption of $O_2$ at the metal surface, (2) dissolution of $O_2$ in the metal and nucleation of oxide islands on the surface, and finally, (3) lateral growth of the oxide islands to form a continuous layer of the oxide. If the oxide remains crack-free and stable, the rate of oxidation is often inversely proportional to the oxide thickness, which is known as the "parabolic" rate law (Ref 52). The parabolic rate law arises when the rate of an oxidation reaction is limited by the ionic diffusion through a thickening oxide film. Although electrons must also move across the film to sustain the oxidation process, most metal oxides (with the notable exception of $Al_2O_3$) are good electronic conductors, resulting in an ionic diffusion through the semiconductor oxide "electrolyte" between the coating and its environment becoming the rate-limiting step.

When a coating of complex chemical composition is exposed to an oxidizing environment, all the metal atoms on its surface tend to be oxidized. To the extent that these oxides form a barrier to further oxidation, the subsequent reactions only oxidize the most reactive elements of the alloy, such as Cr and Al. The minor constituents of the surface oxide alter the corrosion rate by acting as dopants in the semiconductor oxide and changing the diffusion rates of anions and cations across this oxide (Ref 66).

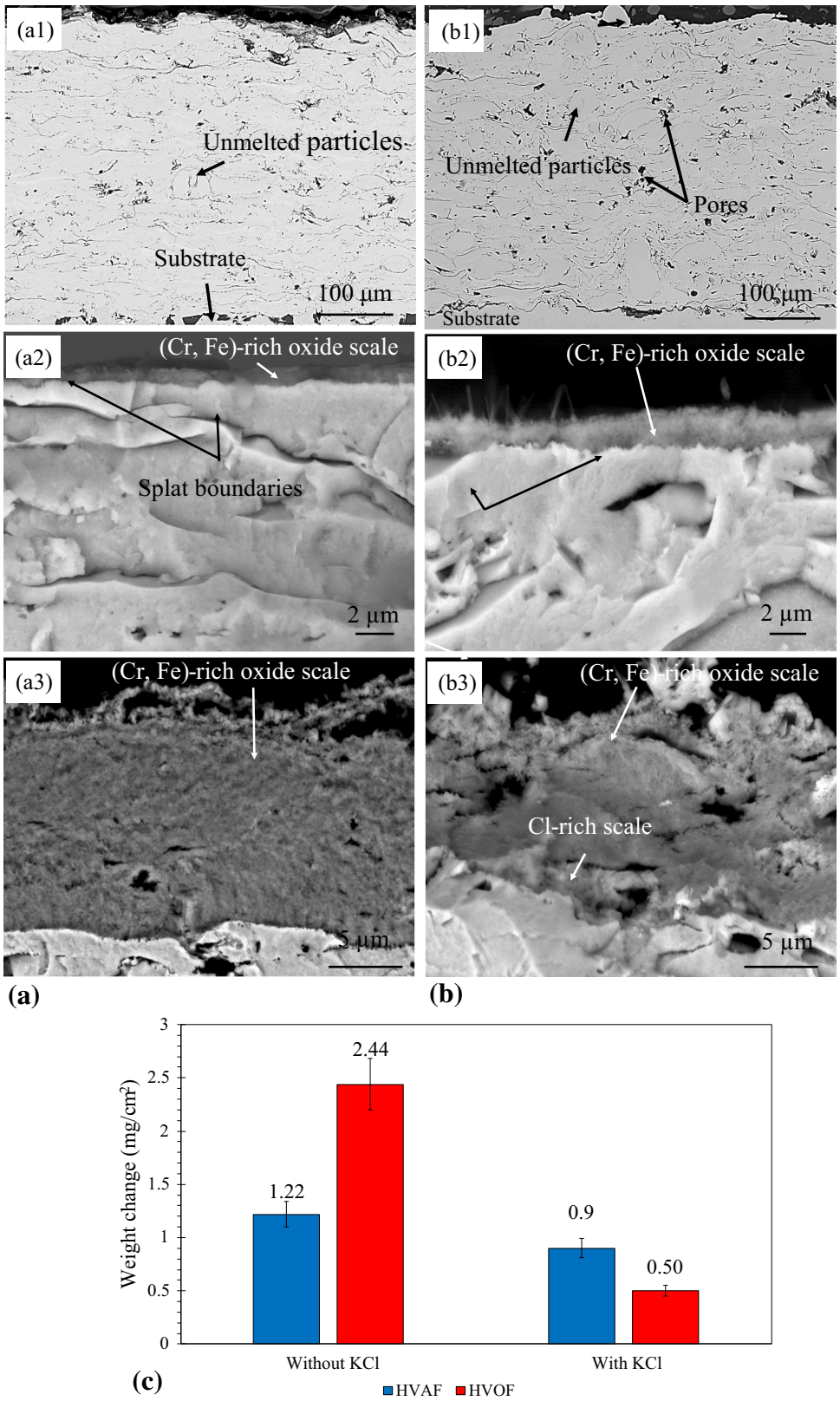


**Fig. 7** (a) Cross sections of as-sprayed and exposed (a) HVAF, (b) HVOF-sprayed amorphous FeCrNiMoBSiC coatings, (a1) as-sprayed HVAF, (a2) HVAF exposed to ambient air (600 °C, 168 h), (a3) HVAF exposed to ambient air + KCl (600 °C, 168 h); (b1) as-sprayed HVOF, (b2) HVOF exposed to ambient air (600 °C, 168 h), and (b3) HVOF exposed to ambient air + KCl (600 °C, 168 h); and (c) weight changes in the two coatings in ambient air after 168 h of exposure at 600 °C with and without KCl (Ref 64). Reprinted with permission from Elsevier

*Ambient Air Containing a Mixed Salt*

Aguero et al. (Ref 67) investigated the effect of the coating composition exposed to a mixed salt. The coatings included a slurry-applied diffusion aluminide, a Cr aluminide, as well as HVOF-sprayed Fe50Cr, Ni20Cr, and Ni5Al coatings. The coatings were exposed to 550 °C for up to 528 h in a flowing model biomass oxy-combustion atmosphere containing 60%$CO_2$-30%$H_2O$-8%$O_2$-2%$N_2$ (vol.%) with 400 vppm HCl and 2 vppm $SO_2$. The samples were covered with KCl-$K_2SO_4$ before the exposure. The microstructure of the exposed coatings is shown in Fig. 8. The studied materials and coatings can be ordered based on the thickness of the oxide scale spallation and the degradation of the coating as follows (from higher to lower degradation): Ni5Al > Cr aluminide > Ni20Cr > Fe50Cr > Aluminide. Both composition and morphology played important roles, and well-behaved high Al- and Cr-containing coatings were observed.

Varis et al. (Ref 68) investigated the corrosion behavior of HVOF and wire arc-sprayed NiCr and FeCr coatings under simplified biomass combustion conditions; see Fig. 9(a). The coatings were sprayed by using two HVOF guns, namely carbide jet system (CJS) and diamond jet (DJ) hybrid. The corrosion tests were performed in ambient air environment with a salt mixture (KCl–$K_2SO_4$), which was observed in the coated specimens that were then heat-treated for 168 h at two temperatures (550 and 600 °C) in two gas atmospheres (air and air + 30% $H_2O$). The corrosion resistance of the HVOF-sprayed Ni50Cr, Ni21Cr, and wire arc-sprayed Fe30Cr coatings was rather promising and comparable to the performance of Sanicro 28 steel; see Fig. 9(b).

*Water Vapor With and Without a Salt Deposit*

Ni-based coatings alloyed with ~ 20 wt.% Cr (Ref 69) are widely used for protecting components against oxidation in dry environments, as an oxide scale of $Cr_2O_3$ (Ref 70) can potentially protect the coating and the substrate from further oxidation. However, water vapor is present in many environments that are of industrial relevance (e.g., boilers).

Sadeghimeresht et al. (Ref 71-74) investigated the isothermal oxidation behaviors of HVAF-sprayed Ni21Cr, Ni5Al, and Ni21Cr7AlY coatings in 5% $O_2$ + 20% $H_2O$ + $N_2$ at 600 °C for 168 h. As shown in Fig. 10, unlike the other two coatings, the alumina-forming Ni5Al showed a weight loss when KCl was added, due to the formation of a volatile species, which is explained later. All the coatings succeeded in maintaining their integrity with the substrate during the exposure.

A thin Cr-rich oxide scale (a mixed layer of $NiCr_2O_4$ and $Cr_2O_3$) formed on the Ni21Cr coating, whereas a thin scale of $Al_2O_3$ mixed with $NiAl_2O_4$ and $NiCr_2O_4$ formed on the Ni21Cr7AlY coating; see Table 3. While signs of internal oxidation in the Ni21Cr7AlY coating were observed, no breakaway oxidation occurred in the three exposed coatings in the presence of water vapor without KCl (Fig. 10). The effect of water vapor was insignificant in such a low $pO_2$ environment (5 vol.%) owing to the large Cr or Al reservoir and the continued growth of a Cr-rich oxide or $Al_2O_3$. Once KCl was introduced, the formation of $K_2CrO_4$ was detected on both Ni21Cr and Ni21Cr7AlY coatings; however, Ni5Al showed a weight loss, most probably due to the formation of a volatile species such as KCl (g) or $NiCl_2$ (g). As the microstructure of the Ni5Al coating was less affected by KCl compared to the other two coatings where $K_2CrO_4$ formed, the formation of KCl (g) could be expected as the main reason for the weight loss. The splat boundaries were found to be the main diffusion paths for the corrosive species; see Table 3.

Sundararajan et al. (Ref 75) investigated a two-layered NiCr (undercoat) and Al (topcoat) APS-deposited coating on modified 9Cr-1Mo steel. The aim was to fill the pores produced by 50Ni-50Cr undercoat with the Al topcoat during steam oxidation. The steam-oxidized samples revealed Ni and Cr diffusion toward the Al coating structure that changed the topcoat to NiAl intermetallics. Although the two-layered coating exhibited an excellent performance against steam oxidation for the base steel substrate until 3000 h of the test, the top layers of the coating underwent significant internal oxidation. The two-layered coating transforms into a three-layered structure during the steam oxidation; see Fig. 11. During the initial stages of steam oxidation, Ni diffused from the NiCr undercoat to the Al topcoat and formed NiAl intermetallics as a continuous layer. Upon increasing the temperature or the duration, the newly formed continuous NiAl layer experiences (1) a morphological change to form a grain-like structure and (2) internal oxidation of the surface. The NiCr undercoat appeared to be intact, except for the increased formation of oxides at the inner splat boundaries. The oxides at the splat boundaries were mainly those of Cr.

Oksa et al. (Ref 76) investigated HVOF-sprayed NiCr, Alloy 625, Ni-21Cr-10 W-9Mo-4Cu, and Fe-based partly amorphous alloy SHS9172 (Fe-25Cr-15 W-12Nb-6Mo); see Fig. 12(a). The coatings were sprayed by using two HVOF guns, CJS and DJ hybrid. High-temperature corrosion testing was carried out in NaCl-KCl-$Na_2SO_4$ salt and controlled $H_2O$ atmosphere at 575 and 625 °C. Based on the test results (see Fig. 12b and c), it is observed that the optimization of the coating structure and selection of suitable chemical composition are critical. The spray technique and spray parameters have strong influences on, e.g., the porosity, lamellar cohesion, melting state, oxidation, and adherence of the coating and thus impact the

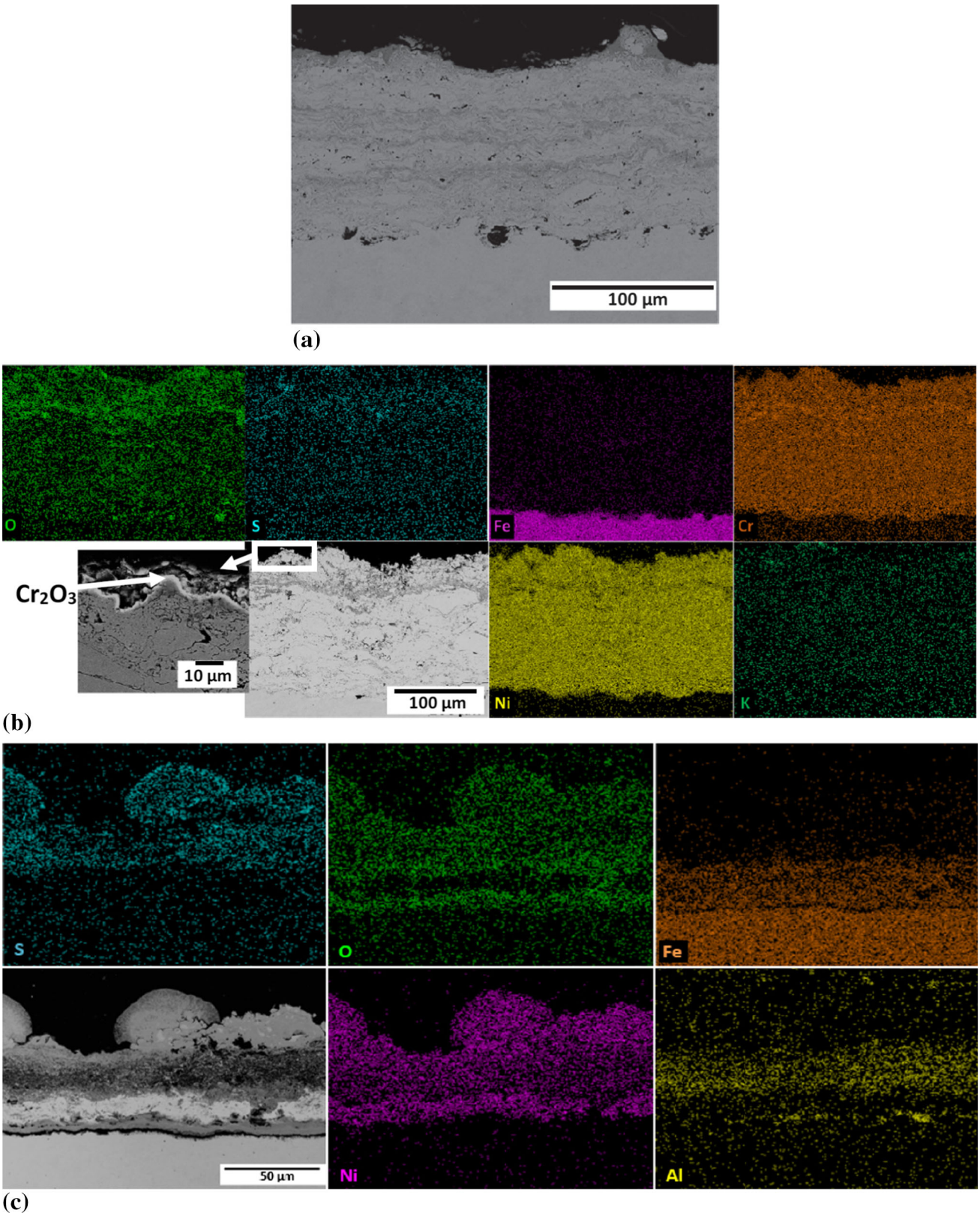


**Fig. 8** SEM (SE mode) cross section and element mapping of HVOF-sprayed (a) Fe50Cr, (b) Ni20Cr and (c) Ni5Al coatings exposed to biomass corrosion at 550 °C for 528 h (Ref 67). Reprinted with permission from Elsevier

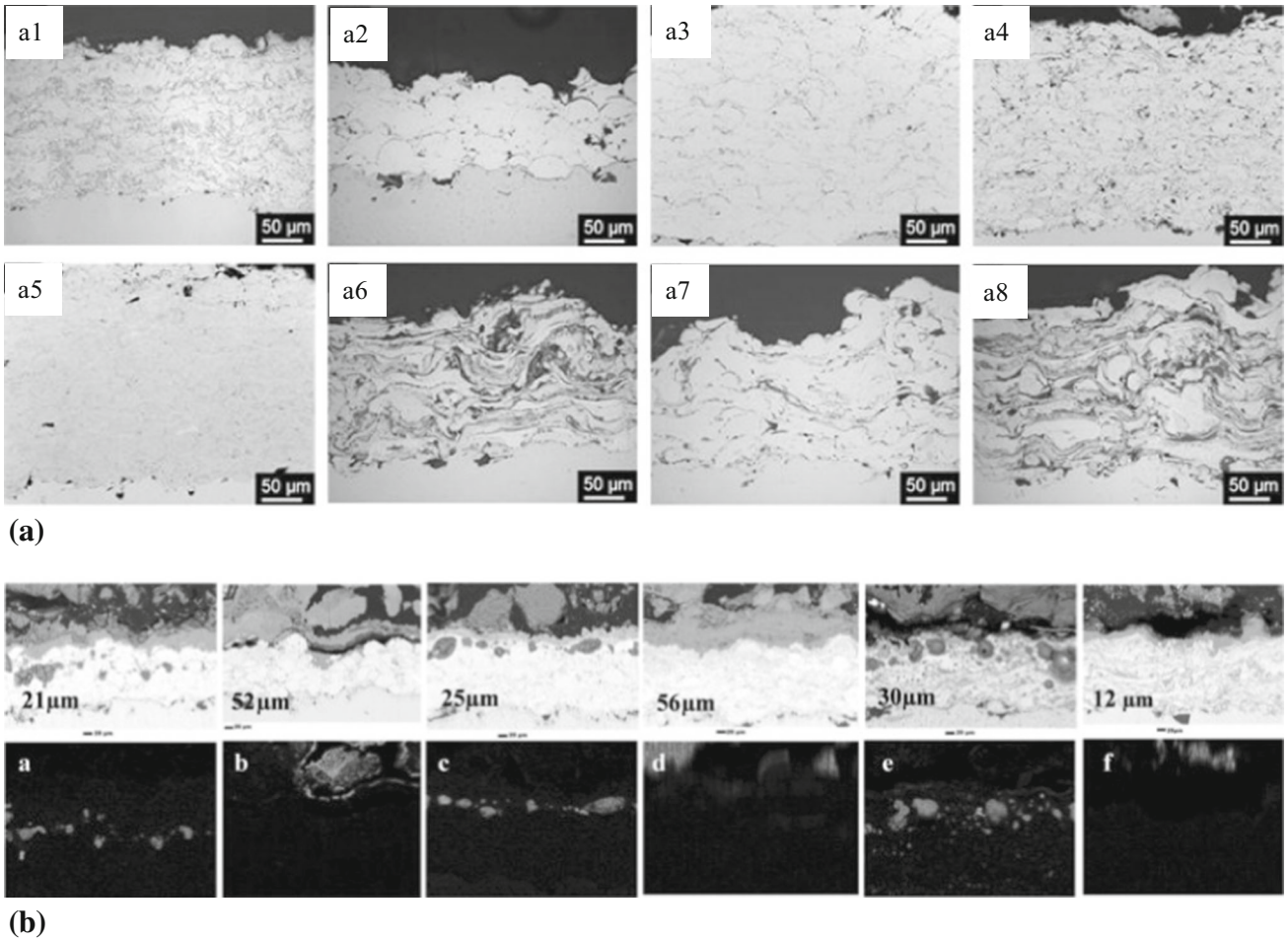


**Fig. 9** (a) Optical micrographs of (a1) HVOF (DJ hybrid)-sprayed Ni50Cr (hot), (a2) HVOF (DJ hybrid)-sprayed Ni50Cr (cold), (a3) HVOF (CJS)-sprayed Ni50Cr, (a4) HVOF (CJS)-sprayed Ni21Cr, (a5) HVOF (CJS)-sprayed Fe25Cr, (a6) wire arc-sprayed Ni45Cr, (a7) wire arc-sprayed Fe30Cr (amorphous), and (a8) wire arc-sprayed Fe13Cr; (b) SEM images and Cl EDX maps of NiCr coatings after exposures: (a) HVOF Ni50Cr-cold exposed to air at 600 °C, (b) HVOF Ni50Cr-cold exposed to air + 30% $H_2O$ at 600 °C, (c) HVOF Ni50Cr-hot exposed to air at 600 °C, (d) HVOF Ni50Cr-hot exposed to air + 30% $H_2O$ at 600 °C, (e) wire arc-sprayed Ni45Cr exposed to air at 600 °C, and (f) wire arc-sprayed Ni45Cr exposed to air + 30% $H_2O$ at 600 °C. The corrosion/oxide layer thicknesses are also included in the upper image (Ref 68). Reprinted with permission from Elsevier

corrosion protection properties. Dense HVOF coatings can offer good protection to low-alloy boiler tube materials even in harsh conditions, in which molten salts may be present, and thus increase the lifetime of the boiler tubes. Low porosity and good lamellar cohesion are very important in the case of thermal spray coatings, as the lamellar boundaries act as corrosion paths and detachment of the lamellae may be high in harsh corrosion conditions. Therefore, a detailed optimization of the coating structure with a suitable chemical composition should be carried out carefully.

There is limited information regarding the oxidation of NiCr alloys in a wet environment in the literature. Although it was proposed that Ni-based coatings might be unaffected by the presence of water vapor (Ref 77, 78), it was shown elsewhere that in the presence of water vapor, an increase in the oxidation rate of a NiCr-based coating with the addition of Al could be detected (Ref 79). It was further shown that the degree of material degradation due to water vapor depends on the partial pressure of oxygen in the test environment. At low $pO_2$, the formation of less-protective oxides such as NiO could be reduced and, thereby, the Cr content required to form the protective Cr-rich scale would be lower (Ref 44).

The Ni21Cr coating studied by Sadeghimeresht et al. (Ref 72) had a Cr content of ≈ 21 wt.%. A thin and protective oxide scale rich in Cr was expected to form, as also reported in the literature (Ref 81). It seems that with 21% Cr, the depletion in Cr was relatively small, and the breakaway was avoided (Ref 82).

A Ni21Cr7AlY coating had similarly shown lower weight gain compared to a Ni21Cr coating exposed to dry

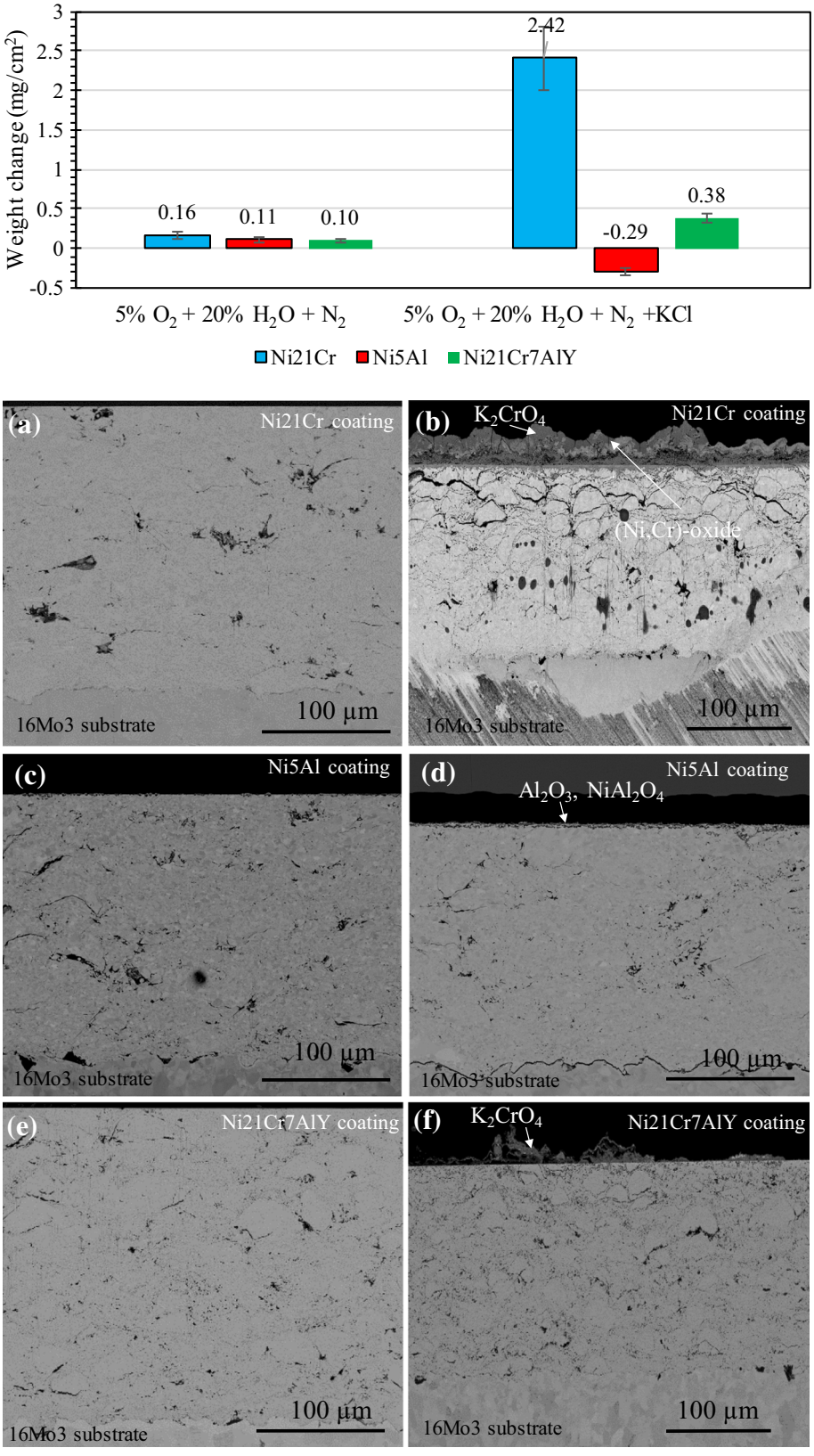


**Fig. 10** Weight changes in HVAF-sprayed Ni21Cr, Ni5Al, and Ni21Cr7AlY, coatings in a moisture-laden environment after exposure for 168 h at 600 °C, with and without KCl, and back-scattered cross-sectional SEM images of the Ni21Cr and Ni21Cr7AlY coatings oxidized in $N_2$ + 5% $O_2$ + 20% $H_2O$ at 600 °C for 168 h. (a), (c), and (e) represent the coatings exposed in the absence of KCl, whereas the coatings shown in (b), (d), and (f) were exposed to KCl. The cross sections were prepared by using the broad ion beam (BIB) milling technique (Ref 71, 72). Reprinted with permission from Elsevier

**Table 3** Corrosion products formed on the surface of the coatings exposed to a moisture-laden environment for 168 h at 600 °C (Ref 71, 72)

| Coatings | Corrosion products | |
|---|---|---|
| | Without KCl | With KCl |
| Ni21Cr | $Cr_2O_3$, $NiCr_2O_4$ | $CrCl_3$, $NiCr_2O_4$, $K_2CrO_4$ |
| Ni5Al | NiO, $Al_2O_3$, $NiAl_2O_4$ | $Al_2O_3$, $NiAl_2O_4$ |
| Ni21Cr7AlY | $Al_2O_3$, $Ni(Cr,Al)_2O_4$ | $Ni(Cr,Al)_2O_4$, $K_2CrO_4$ |

ambient air environment at 600 °C for 168 h (Ref 58). The lower weight change in the Ni21CrAlY coating in the presence of water vapor (Ref 72) results in a better corrosion performance of alumina-forming coatings in both dry and wet environments. Galerie et al. (Ref 83) have reported a low rate of NiO growth when $H_2O$ is the only oxidant present due to slow phase boundary reaction for the insertion of oxide ions into the scale. In any case, the concentration of Cr needed to form an external scale is expected to decrease with decreasing growth rate of NiO. While it was previously found that water vapor addition enhances the growth rate of the Cr-rich scale (Ref 44), it was shown by Sadeghimeresht et al. (Ref 72) that water vapor increased the oxidation rate. Considering the simultaneous effect of oxygen and water vapor, high $pO_2$ could be more beneficial as it encourages the formation of the protective oxide scale, whereas adding water vapor interrupts the protectiveness of the formed oxide scale.

Due to the formation of oxides within the coatings, particularly Ni21Cr7AlY, a potential mechanism to explain the role of water vapor might be that $H_2O$ led hydrogen to dissolve into the coating's defects such as pores through splat boundaries. The dissolved hydrogen is supposed to enhance oxygen diffusivity in the pores, thereby enhancing internal oxidation of the coating (Ref 45).

*Hydrochloric Acid (HCl) With and Without a Salt Deposit*

Uusitalo et al. (Ref 84) investigated the oxidation performances of five HVOF-sprayed coatings (Ni49Cr2Si, Ni57CrMoSiB, Ni21Cr9MoFe, Fe15Al2Cr, and Ni50Cr) and the effect of laser remelting; see Fig. 13. The oxidation tests were performed in an oxidizing atmosphere of 20%$H_2O$-3%$O_2$ (vol.%) containing 500 vppm HCl and balance Ar. The test temperature was 550 °C and the test duration 1000 h. The homogeneous and dense coatings obtained in the cases of high Cr contents performed well and protected the substrate material; see Fig. 13. The corrosive species were able to penetrate some of the HVOF coatings and attack the substrate via an interconnected network of voids and oxides at the splat boundaries. Laser melting remarkably increased the corrosion resistance of HVOF coatings by homogenizing the structure of the coating; see Fig. 13(e).

Paul et al. (Ref 85) investigated the corrosion behaviors of four HVOF-sprayed Ni-based coatings (Ni17Cr3B4-Si5Fe, Alloy 718; Ni19Cr3Mo5Nb, Alloy 625; Ni21Cr8-Mo4Nb, and Alloy C-276; Ni16Cr16Mo5Fe4 W) in simulated high-temperature biomass combustion conditions. The corrosion performances of the coatings varied when tested at ~ 525, 625, and 725 °C in $K_2SO_4$-KCl mixture and gaseous HCl-$H_2O$-$O_2$ containing environments. The Alloy 625, NiCrBSiFe, and Alloy 718 coatings performed better than the alloy C-276 coating at 725 °C, which exhibited very little corrosion resistance, resulting in degradation that was similar to that of uncoated P91. Alloy 625 performed the best among these coating materials, with the overall order at 725 °C being as follows: Alloy 625 > NiCrBSiFe > Alloy 718 > Alloy C-276. Although the Alloy C-276 coating performed poorly in the corrosion test environment of 725 °C, at lower temperatures (i.e., below the eutectic temperature of the salt mixture) it outperformed the other coatings studied, as the predominant mechanism changes from molten-salt corrosion to gaseous corrosion. Both mechanisms are shown in Fig. 14.

Bai et al. (Ref 8) studied the corrosion behavior of HVOF-sprayed $\beta$-NiAl coatings in a synthetic gas

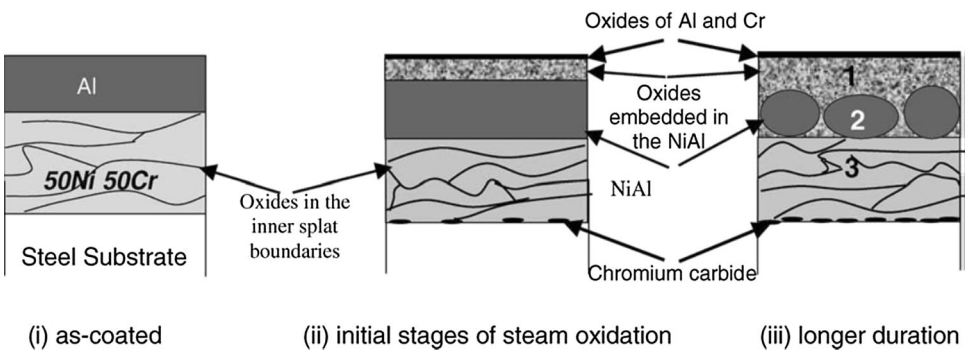


**Fig. 11** Schematic view of the change in two-layered Ni-Cr and Al coatings during steam oxidation (Ref 75). Reprinted with permission from Elsevier

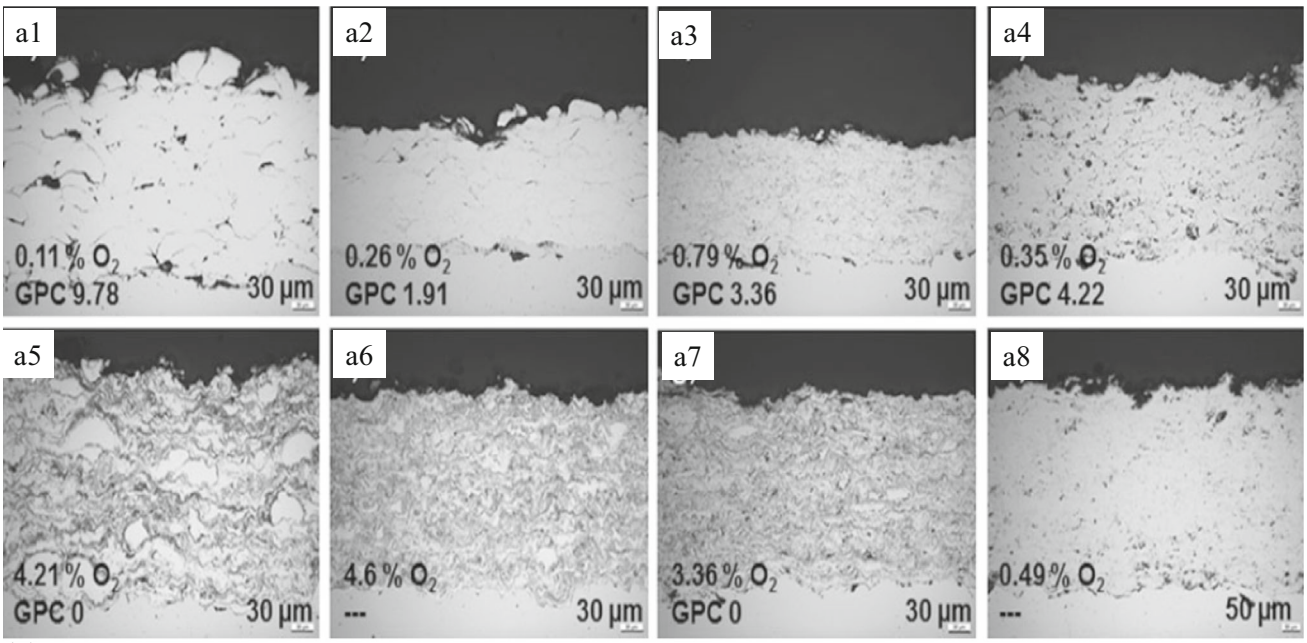
a1
0.11 % O2
GPC 9.78
30 µm
a2
0.26 % O2
GPC 1.91
30 µm
a3
0.79 % O2
GPC 3.36
30 µm
a4
0.35 % O2
GPC 4.22
30 µm
a5
4.21 % O2
GPC 0
30 µm
a6
4.6 % O2
---
30 µm
a7
3.36 % O2
GPC 0
30 µm
a8
0.49 % O2
---
50 µm

(a)

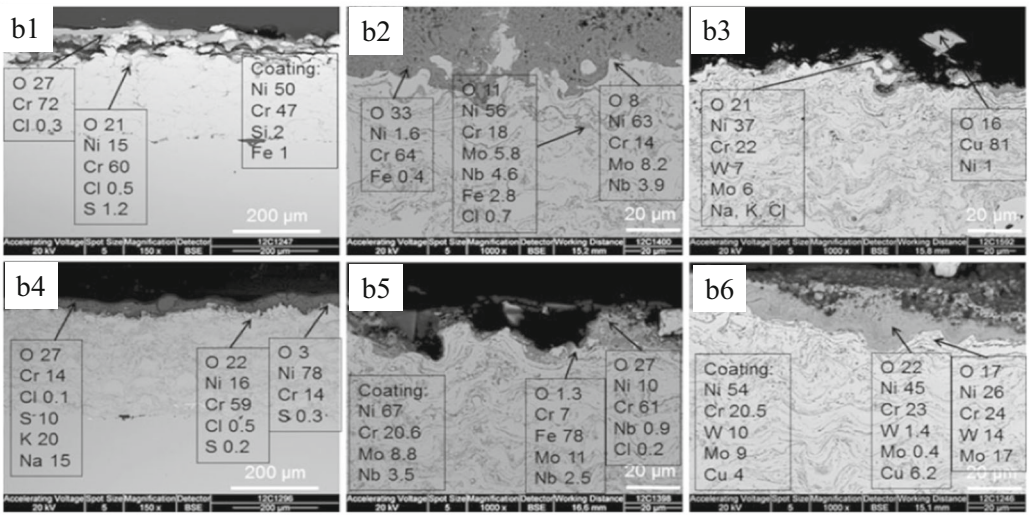
b1
O 27
Cr 72
Cl 0.3
O 21
Ni 15
Cr 60
Cl 0.5
S 1.2
Coating:
Ni 50
Cr 47
Si 2
Fe 1
200 µm
b2
O 33
Ni 1.6
Cr 64
Fe 0.4
O 11
Ni 56
Cr 18
Mo 5.8
Nb 4.6
Fe 2.8
Cl 0.7
O 8
Ni 63
Cr 14
Mo 8.2
Nb 3.9
20 µm
b3
O 21
Ni 37
Cr 22
W 7
Mo 6
Na, K, Cl
O 16
Cu 81
Ni 1
20 µm
b4
O 27
Cr 14
Cl 0.1
S 10
K 20
Na 15
O 22
Ni 16
Cr 59
Cl 0.5
S 0.2
O 3
Ni 78
Cr 14
S 0.3
200 µm
b5
Coating:
Ni 67
Cr 20.6
Mo 8.8
Nb 3.5
O 1.3
Cr 7
Fe 78
Mo 11
Nb 2.5
O 27
Ni 10
Cr 61
Nb 0.9
Cl 0.2
20 µm
b6
Coating:
Ni 54
Cr 20.5
W 10
Mo 9
Cu 4
O 22
Ni 45
Cr 23
W 1.4
Mo 0.4
Cu 6.2
O 17
Ni 26
Cr 24
W 14
Mo 17
20 µm

(b)

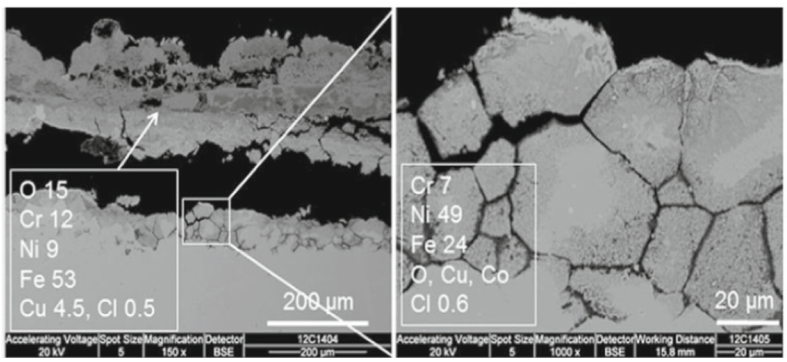
O 15
Cr 12
Ni 9
Fe 53
Cu 4.5, Cl 0.5
200 µm
Cr 7
Ni 49
Fe 24
O, Cu, Co
Cl 0.6
20 µm

(c)

◀**Fig. 12** Optical images of the coatings before testing. (a1) NiCr-CJS, (a2) Alloy 625-CJS, (a3) Diam4006-CJS, (a4) SHS9172-CJS, (a5) NiCr-DJ, (a6) Alloy 625-DJ, (a7) Diam4006-DJ, and (a8) SHS9172-DJ. Oxygen content (wt.%) and viscous gas permeability coefficients (GPC) of the coatings (a7 and a8 not measured) (Ref 76); (b) SEM images (BSE mode) obtained after the testing: (b1) NiCr-CJS (575 °C), (b2) Alloy 625-DJ (575 °C), (b3) Diam4006-DJ (575 °C), (b4) NiCr-DJ (575 °C), (b5) Alloy 625-DJ (625 °C), and (b6 and Diam4006-DJ (625 °C). Penetration of corrosion through lamellar boundaries and detachment of outer lamellae due to the corrosion reactions can be seen in micrograph (a) (Ref 76); and (c) SEM images (BSE mode) of San 25 after exposure at 575 °C, and EDX point analysis of the corrosion product (Ref 76). Reprinted with permission from Elsevier

containing 500 ppm HCl with 10 wt.% KCl ash deposit at 700 °C for 250 h based on the thermodynamics. It was found that the formation of both volatile $AlCl_3$ (g) and $NiCl_2$ (g) would contribute to the fast growth of $Al_2O_3$, especially at the coating/substrate interface, where a gradient of vapor pressure exists from the sample center to the edges. This explains why corrosion was more severe near the sample edges than at the sample center, as shown in Fig. 15(a). Furthermore, the depletion of Al due to the fast-growing $Al_2O_3$ could result in a phase transformation to $\gamma'$-$Ni_3Al$ and the formation of more volatile and non-protective oxides such as NiO and $NiAl_2O_4$ (spinel). Figure 15(b) and (c) shows the thermodynamic phase diagrams of the NiAl-$O_2$-$Cl_2$ and $Ni_3Al$-$O_2$-$Cl_2$ systems at 700 °C as calculated by Thermo-Calc®. For $\gamma'$-$Ni_3Al$, more volatile oxides and chlorides could form in the presence of $Cl_2$ and $O_2$, such as $NiCl_2$, NiO, and $NiAl_2O_4$. All of them are fast-growing products, but none is as protective as $Al_2O_3$ and therefore should be avoided. Once a coherent $Al_2O_3$ scale forms on an alloy surface, it inhibits the formation of other volatile oxides and thus protects the alloy.

Reddy et al. (Ref 86) studied an amorphous Fe-Cr-B coating deposited by HVOF and laser cladding; see Fig. 16(a) and (b). Corrosion tests were carried out in an HCl-rich environment at 700 °C for 250 h with and without KCl. In the absence of KCl, the amorphous HVOF-sprayed coating with a thin oxide scale performed very well, while the crystalline laser cladding suffered from ~ 350 μm of metal loss; see Fig. 16(c), (d), (e), and (f). When KCl was introduced, the HVOF-sprayed coating delaminated from the substrate and $MnCl_2$ was mainly found in the scale. The weight gain of the laser-clad specimen was three times that of the HVOF-sprayed coating. It seems that a high amorphous fraction in the coating increased the corrosion resistance. The coating chemistry is promising for heat exchanger components, as a protective $Cr_2O_3$ scale is formed. While the HVOF-sprayed coating showed improved corrosion performance, its spallation could be a major concern in actual boiler environments.

Sadeghimeresht et al. (Ref 87, 88) investigated the Cl-induced corrosion of HVAF-sprayed Ni21Cr, Ni5Al, Ni21Cr7AlY, and Ni21Cr9Mo-$SiO_2$ coatings in 5 vol.%

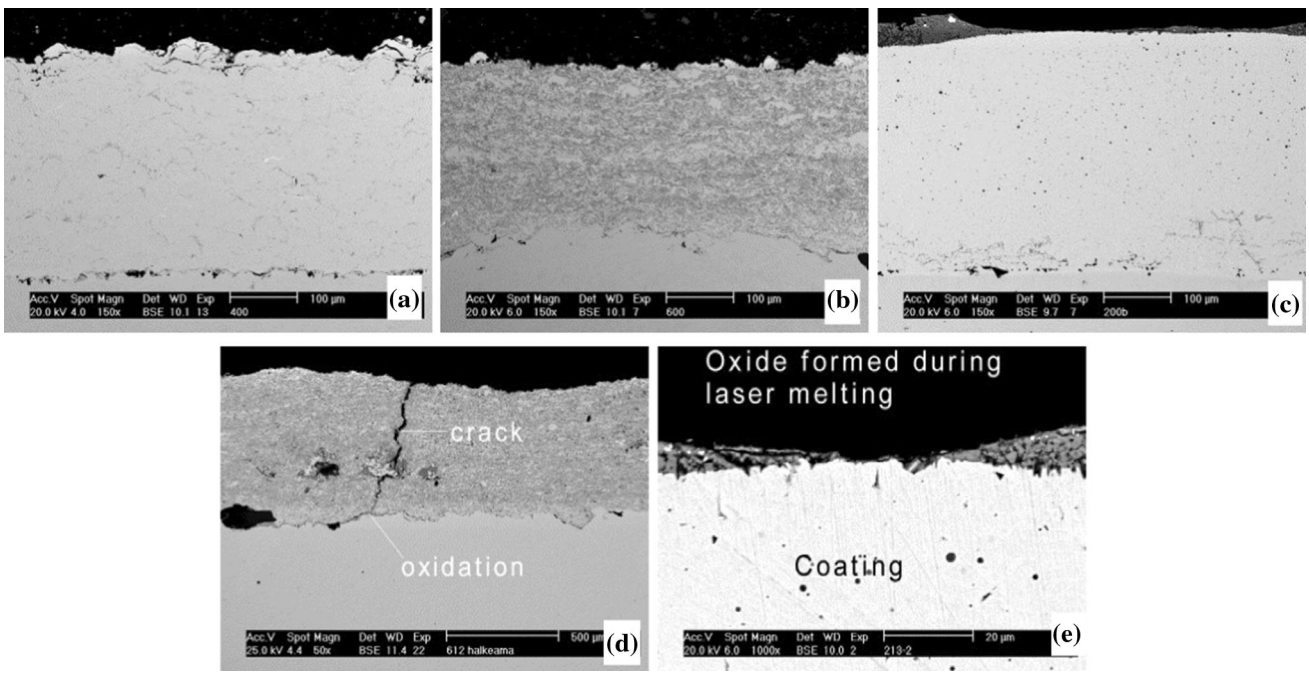


**Fig. 13** Microstructures of (a) Ni57CrMoSiB (DJ hybrid), (b) Ni50Cr (Excalibur), (c) laser-melted Ni57Cr coatings (Ref 84), (d) Ni50Cr (Excalibur) coating after 400 h of exposure (Ref 84), and (e) laser-melted Ni57Cr coating after 1000 h of exposure (Ref 84). Reprinted with permission from Elsevier

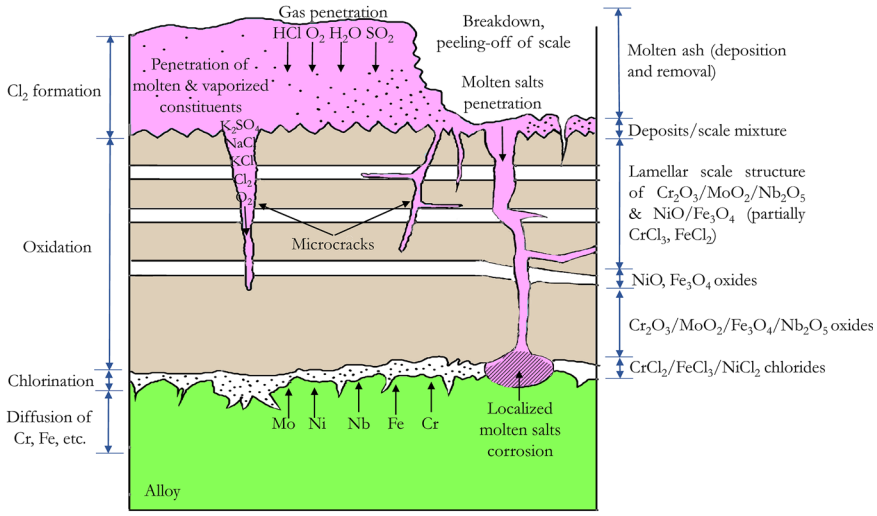


**Fig. 14** High-temperature corrosion mechanisms in the cases where an oxide layer is first formed

$O_2$ + 500 vppm HCl + $N_2$ with and without KCl at 600 °C for exposure up to 168 h. As shown in Fig. 17, all the coatings performed well in the absence of KCl in terms of controlling the corrosion of the substrates by acting as barriers against the corrosive Cl-containing environment. The oxidation behavior was strongly dependent on the protective scale-forming elements such as Cr or/and Al present in the coatings, which formed a protective $Al_2O_3$ or/and $Cr_2O_3$ scale at the test temperature; see Table 4.

Under KCl, the chromia-forming coatings degraded through a two-stage mechanism; see Fig. 18. In the first stage, the corrosion was initiated by the formation of $K_2CrO_4$ and $Cl^-$ through a reaction between KCl and the protective $Cr_2O_3$ formed according to Eq 1. Cl could form as per Eq 2 and 3. $K_2CrO_4$ depleted the Cr oxide scale, leading to a loss of the protective properties of chromia. Metallic chlorides and $Cl_2$ formed during this stage. In the second stage, the formed $Cl_2$ diffused inward through the defects (cracks and pores) present in the non-protective oxide scales formed during the previous stage. $Cl^-$ and $Cl_2$ diffused through the oxide grain boundaries and the oxide defects, respectively, to reach the coating/oxide interface.

Degradation of the protective oxide layer, which is attributed to the formation of $K_2CrO_4$ at the beginning of exposure, was observed by Israelsson et al. and Shu et al. (Ref 89, 90). It was reported that instead of $Cl_2$ (proposed in the "Cl-induced active corrosion" mechanism), $Cl^-$ (formed as per Eq 12) could penetrate the oxide scale through the grain boundaries, leading to the failure (with time) of the protective oxide layer. As already mentioned, $Cl_2$ penetration of the scale is not explained by the "Cl-induced active corrosion" mechanism. Moreover, the reaction proposed as part of the "Cl-induced active corrosion" mechanism for the production of $Cl_2$ (see ΔG of Eq 1) is not thermodynamically favored. It could, therefore, be proposed that $Cl^-$ diffuses into the oxide scale and coating through the grain boundaries and the splat boundaries, respectively, where the oxide is available. As $Cl^-$ is smaller than $Cl_2$, it has higher mobility in the grain boundary region of an oxide. Once $Cl^-$ reaches the scale/coating interface, it reacts with the transition metal ions formed by the oxidation of the coating (Ref 13). It should be noted that the scale/coating interface could be either on top of the coating or inside the coating, in the splat boundaries, where the oxide can form.

The formed solid chlorides have considerable equilibrium vapor pressures, evaporate readily, and diffuse upward toward the gas–oxide scale interface. When sufficient $pO_2$ is available, the gaseous chlorides react with the available $O_2$ to form solid oxides, releasing gaseous chlorine; see Eq 9 and 10 (Ref 19).

The oxide scales formed through these reactions are rather porous, non-protective, and non-adherent to the coating (Ref 91). Independent of Eq 11-15, regarding the formation of $Cl^-$ via an electrochemical mechanism and the subsequent $Cl^-$ diffusion through the oxide grain boundaries, the $Cl_2$ formed according to Eq 9 and 10 could also diffuse through the defects (mainly pores and cracks) present in the newly formed oxide scale toward the scale–coating interface and even further toward the coating–substrate interface (where $pO_2$ was still low). Depending on the alloying elements available in the coating, which were Ni and Cr in the present study, solid metal chlorides, which are thermodynamically stable, could form after the reactions with $Cl_2$ (in regions where $pO_2$ was high); see Eq 4-6. These reactions occur along with the reactions proposed in Eq 11-15. Cr seems to be more preferably attacked than Ni, as the formation of $CrCl_2$ or $CrCl_3$ has a more negative Gibbs free energy than the formation of $NiCl_2$ (Ref 92); see Eq 4-6.

It can be hypothesized that while the Ni21Cr coating was initially degraded via the electrochemical mechanism

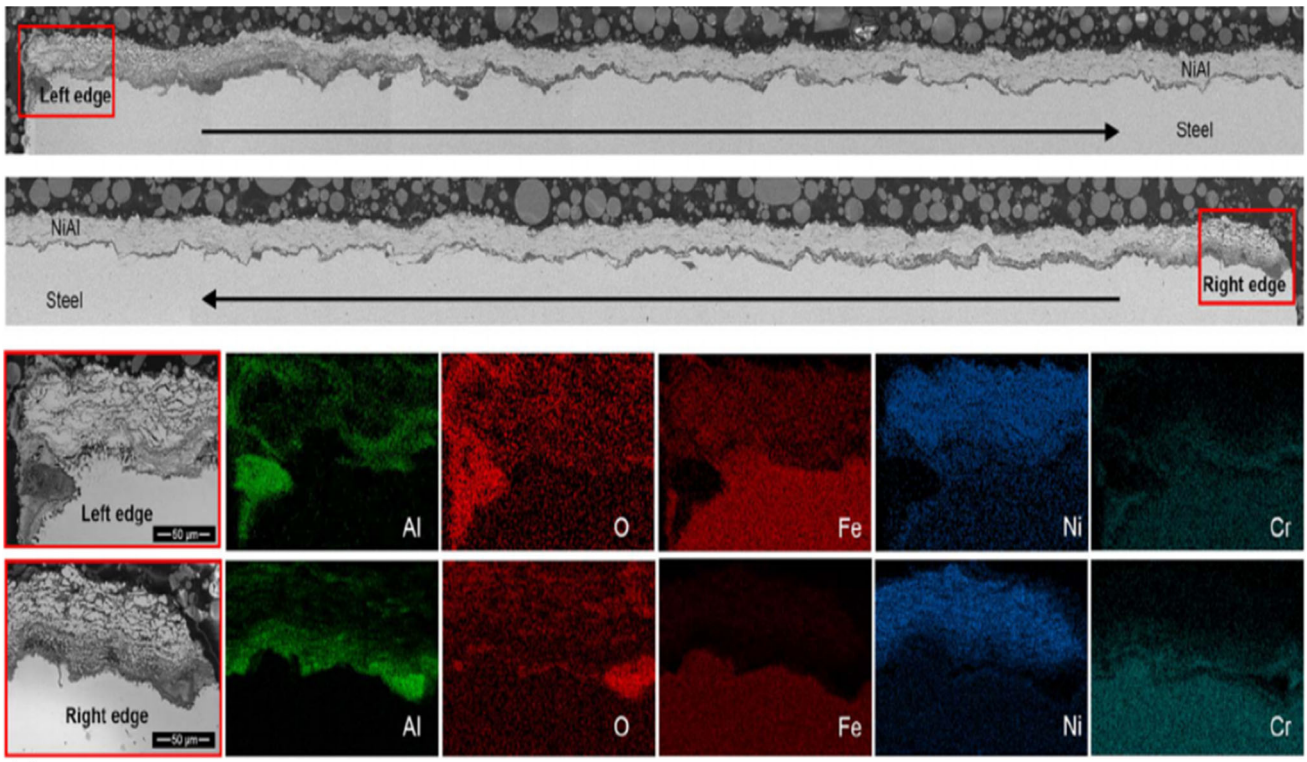


(a)

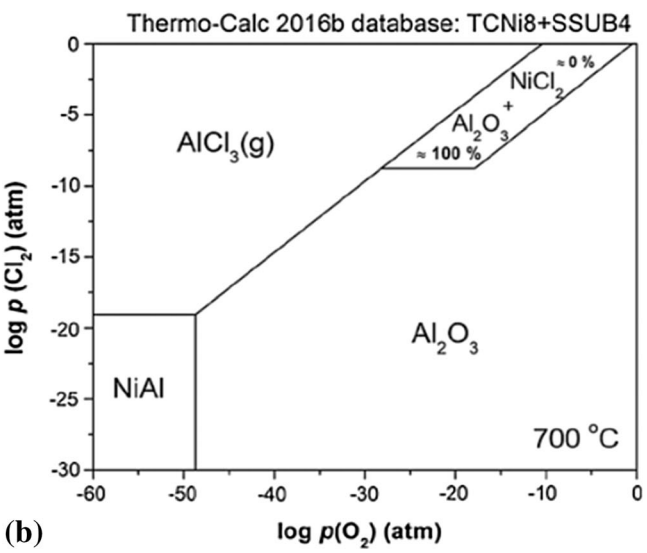


(b)

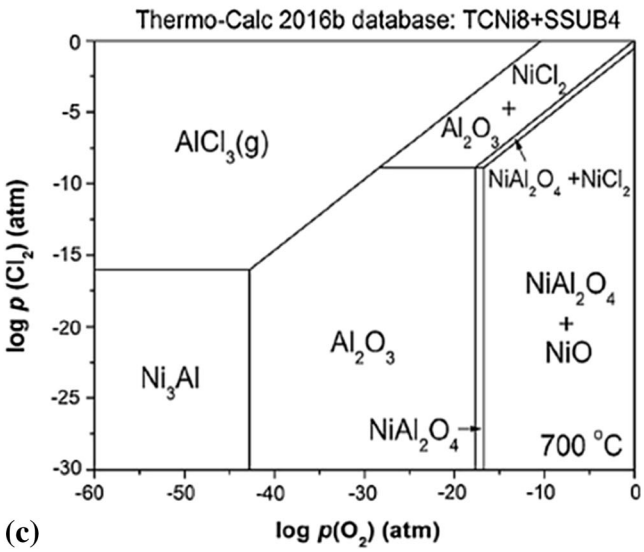


(c)

**Fig. 15** (a) Cross-sectional BSE images of NiAl coatings obtained at the two edges after corrosion at 700 °C for 250 h in synthetic gas with 500 ppm HCl and 10% KCl ash deposit, and the EDX mappings (Ref 8), Thermo-Calc® calculation of the formation of oxides on (a) NiAl and (b) $Ni_3Al$ alloys at 700 °C as functions of $O_2$ and $Cl_2$ partial pressures (Ref 8). Reprinted with permission from Elsevier

during the first stage, the "Cl-induced active corrosion" mechanism, along with the electrochemical mechanism, contributed to the failure of the coating in the second stage.

The alumina scale formed on the Ni5Al coating was rather protective in the presence of KCl; see Fig. 19. The protective alumina impeded the diffusion of $Cl^-$ during the first stage. The corrosion problems might arise only if the oxide scale spalls-off or cracks, forming wide openings for the diffusion of $Cl^-$ present at the coating surface or the oxide/coating interface and the subsequent $Cl^-/Cl_2$ diffusion. Israelsson et al. (Ref 93) showed that the presence of big defects such as cracks in the alumina layer is necessary for corrosion initiation and propagation. Otherwise, there is no chance of $Cl^-$ diffusing. Such large defects are common in alumina scales under thermal cycling conditions.

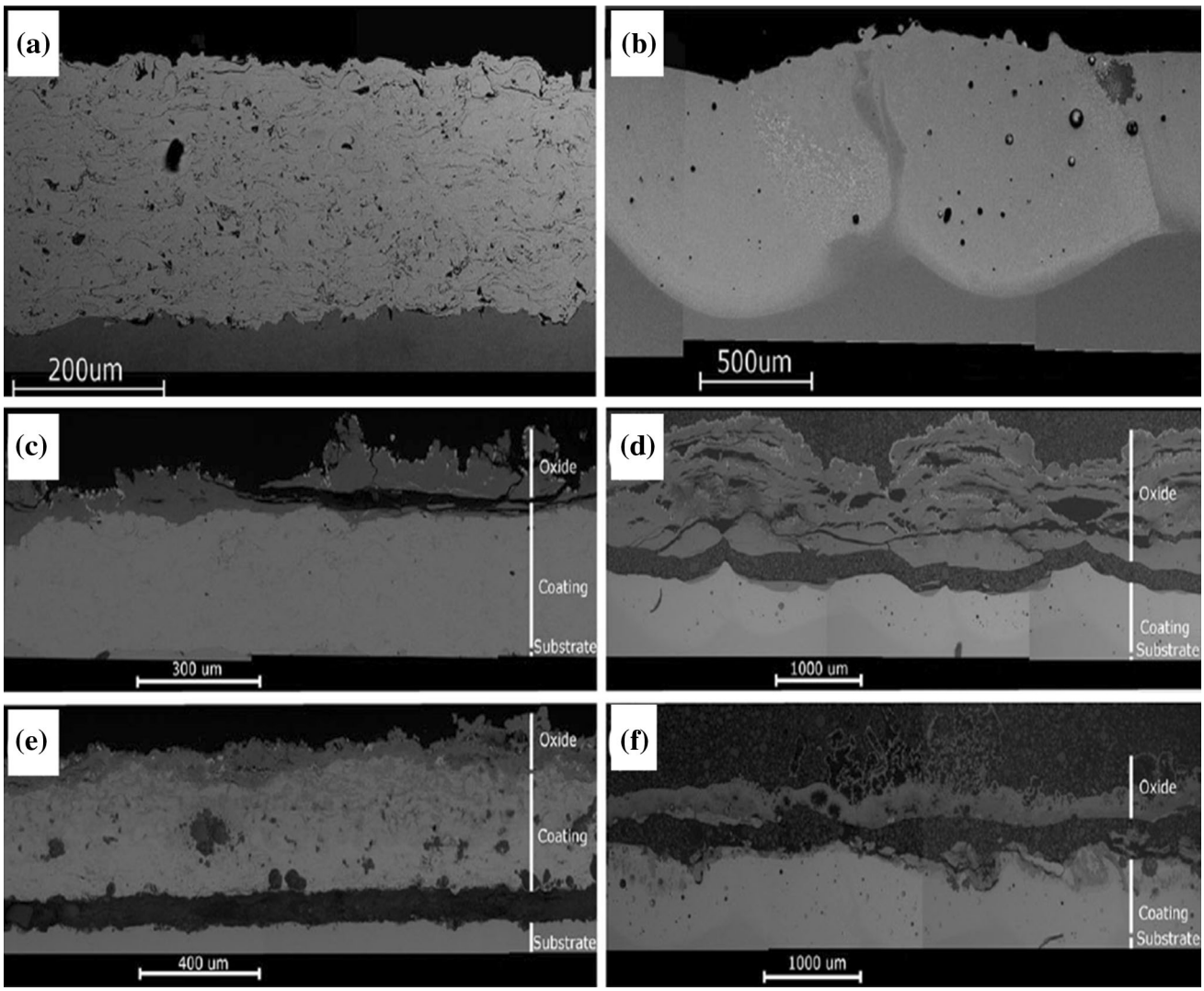


**Fig. 16** SEM images showing the cross sections of (a) as-deposited HVOF coating, (b) as-deposited laser cladding, (c) exposed HVOF-sprayed coating with no deposit, (d) exposed HVOF-sprayed coating with KCl, (e) exposed laser cladding with no deposit, and (f) exposed laser cladding with KCl (Ref 86). Reprinted with permission from Elsevier

In the presence of KCl, $Cl^-/Cl_2$ diffused through a non-protective and porous $NiCr_2O_4$ scale formed on NiCrAlY, leading to the formation of volatile $CrCl_3$. On the other hand, the Mo in NiCrMo-$SiO_2$ stimulated the formation of a more protective Cr-rich oxide scale, which increased the corrosion resistance by reducing the $Cl^-/Cl_2$ diffusion.

The interconnected pores and the intersplat boundaries could act as paths for the $Cl^-/Cl_2$ diffusion as long as the oxide was present. $Cl^-$ could diffuse through the intersplat boundaries of the coatings, forming metal chlorides and accelerating corrosion, which indicated that such regions were microstructural weak points concerning controlling Cl-induced corrosion (Ref 94).

## Reducing Environments

The comparison of investigations into the effect of Cr content in the alloy to reduce corrosion in oxidizing–chloridizing environments reveals contradicting results (Ref 95). A detrimental effect of Cr due to the formation of chromium chloride was reported at 800 °C in 50% HCl-10%$H_2O$-$H_2$ reducing atmosphere (Ref 96). An improvement in corrosion resistance with increasing Cr content was reported in mixed O-Cl environments at 1000 °C (Ref 95).

Sadeghimeresht et al. (Ref 97) studied the oxidation behavior of an HVAF-sprayed NiCoCrAlY coating deposited on AISI 304L in Ar-10%$H_2$-20%$H_2O$ ($pO_2 \approx 10^{-24}$ bar) environment at 600 °C. The NiCoCrAlY coating was found to exhibit improved oxidation behavior owing to the formation of a slow-growing and protective

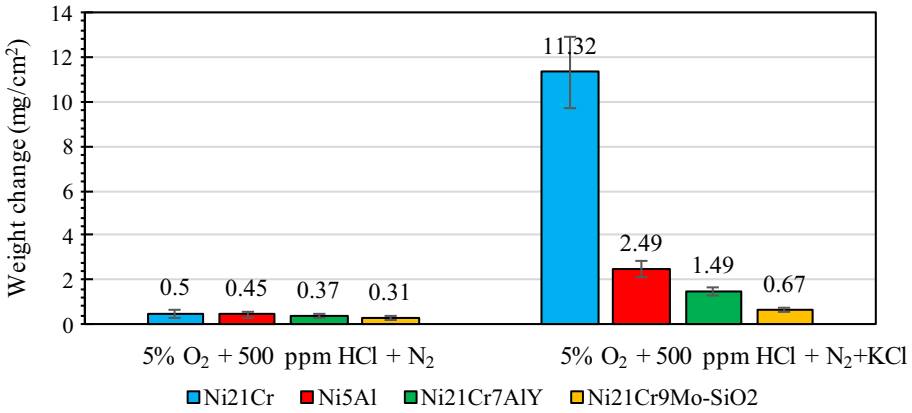


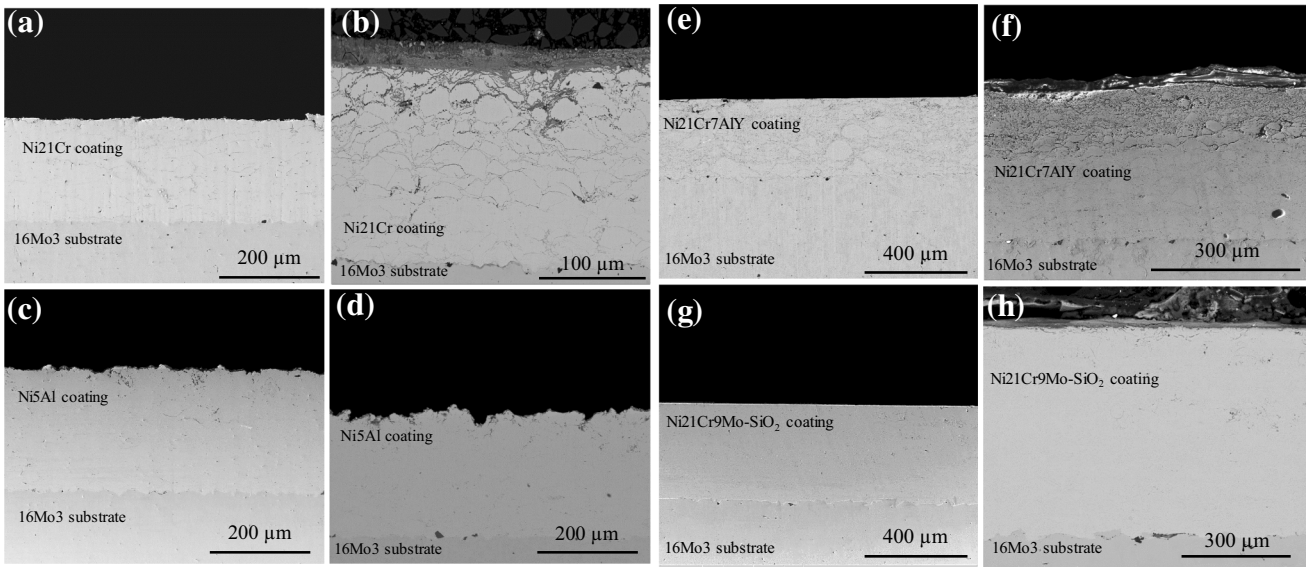


**Fig. 17** Weight changes in HVAF-sprayed Ni21Cr, Ni5Al, Ni21Cr7AlY, and Ni21Cr9Mo-$SiO_2$ coatings in an HCl-laden environment after 168-h exposure with and without KCl, and back-scattered cross-sectional SEM images of the four HVAF-sprayed coatings oxidized in 5% $O_2$ + 500 vppm HCl + $N_2$ at 600 °C for 168 h. (a), (c), (e), and (g) represent the coatings in the absence of KCl, while (b), (d), (f), and (h) show the coatings that were exposed to KCl (Ref 87, 88). Reprinted with permission from Elsevier

**Table 4** Corrosion products formed on the surfaces of coatings exposed to a HCl-laden environment for 168 h at 600 °C (Ref 87, 88)

| Coatings | Corrosion products | |
|---|---|---|
| | Without KCl | With KCl |
| Ni21Cr | NiO, $Cr_2O_3$, $NiCr_2O_4$ | $Cr_2O_3$, $NiCr_2O_4$, $K_2CrO_4$ |
| Ni21Cr7AlY | $Cr_2O_3$ | $CrCl_3$, $K_2CrO_4$, $NiCr_2O_4$ |
| Ni21Cr9Mo-$SiO_2$ | $MoO_3$, $NiCr_2O_4$ | $MoO_3$, $NiCr_2O_4$, $SiO_2$ |
| Ni5Al | $Al_2O_3$ | $Al_2O_3$, $NiAl_2O_4$ |

$Al_2O_3$ scale; see Fig. 20(a). Al depletion of the coating (Fig. 20b) occurred due to the formation of $Al_2O_3$ at the surface, which led to a reduction in Al content in the top part of the coating. However, the Al content (6 wt.%) was not below the critical level, at which the $Al_2O_3$ scale starts losing its protective properties due to an inadequate Al reservoir. The HVAF-sprayed NiCoCrAlY coating showed promising oxidation behavior compared to 304L stainless steel in the test condition considered in this study.

In another work of Sadeghimeresht et al. (Ref 98), the oxidation behaviors of HVAF-sprayed Ni and NiCr coatings (Fig. 21a and b) deposited on 304L stainless steel at 600 °C for 168 h in Ar-10%$H_2$-20%$H_2O$ were studied. The results showed that both Ni and NiCr coatings imparted oxidation protection to the 304L substrate. The chromia-forming 304L steel revealed a duplex but non-protective oxide scale comprising an outer $Fe_3O_4$ layer on an inner $(Fe, Cr)_3O_4$ spinel oxide. In contrast, the NiCr coating presented superior oxidation behavior owing to the formation of a continuous, thin, and slow-growing $Cr_2O_3$ scale. The Ni coating too protected the substrate owing to

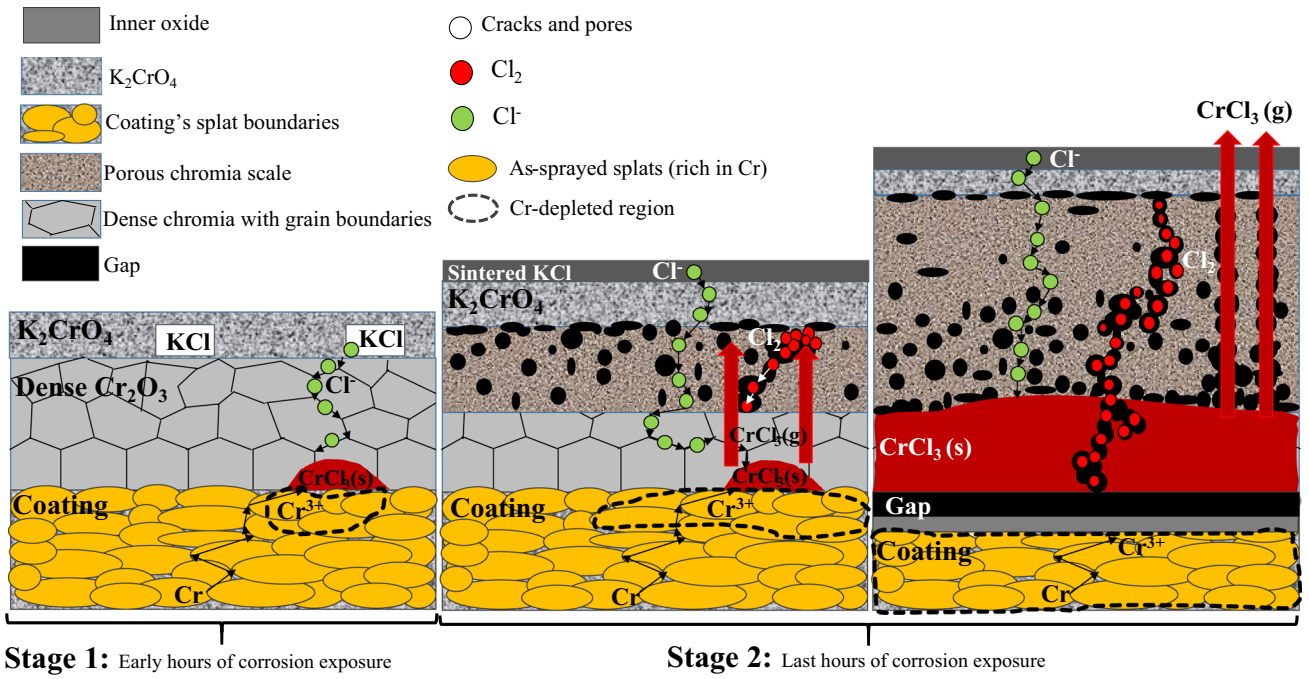


**Fig. 18** Schematic of the proposed corrosion mechanisms in coatings exposed to 5% $O_2$ + 500 ppm HCl + $N_2$ with KCl for 168 h at 600 °C (Ref 87). Reprinted with permission from Elsevier

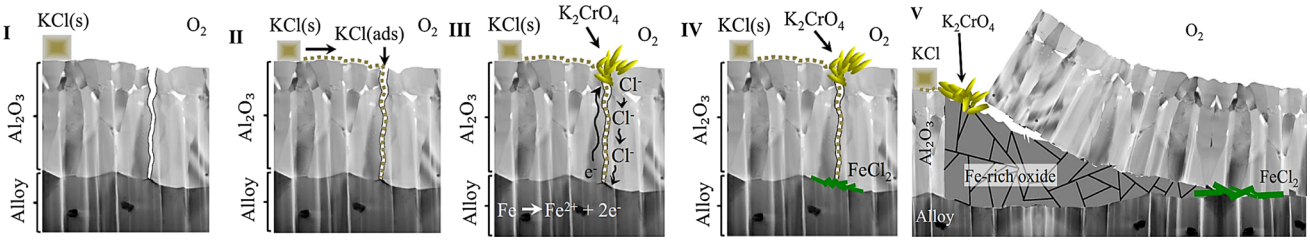


**Fig. 19** Schematic illustration of the initiation of corrosion attack. KCl enters the crack through surface diffusion. The KCl in the crack provides the medium for ion transport. Alumina is a semiconductor with good electron transport properties but does not facilitate ion transport (Ref 93). Reprinted with permission from Elsevier

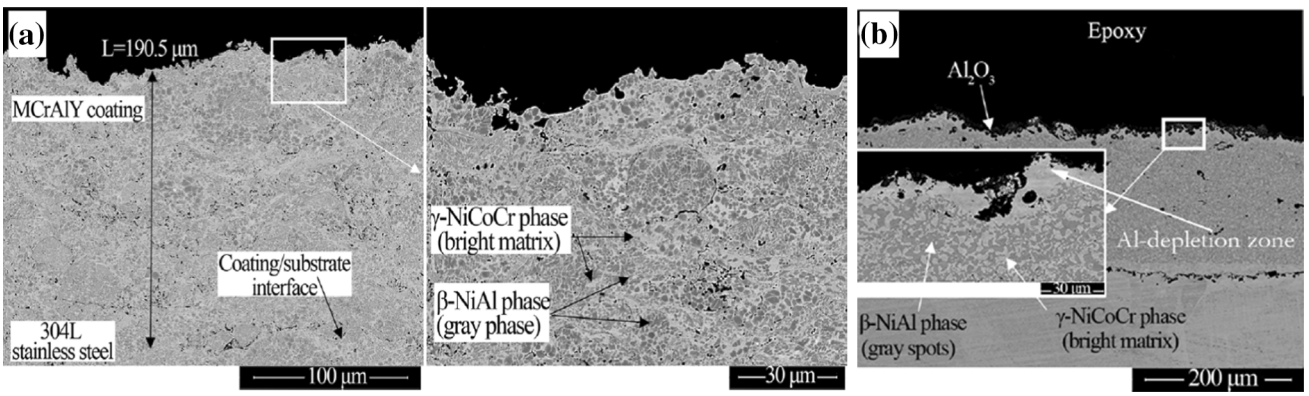


**Fig. 20** (a) Cross-sectional SEM image (BSE) of an as-sprayed NiCoCrAlY coating (Ref 97), and (b) cross-sectional SEM image (BSE) of a NiCoCrAlY-coated steel substrate oxidized at 600 °C in Ar-10%$H_2$-20%$H_2O$ for 168 h (Ref 97). Reprinted with permission from Elsevier

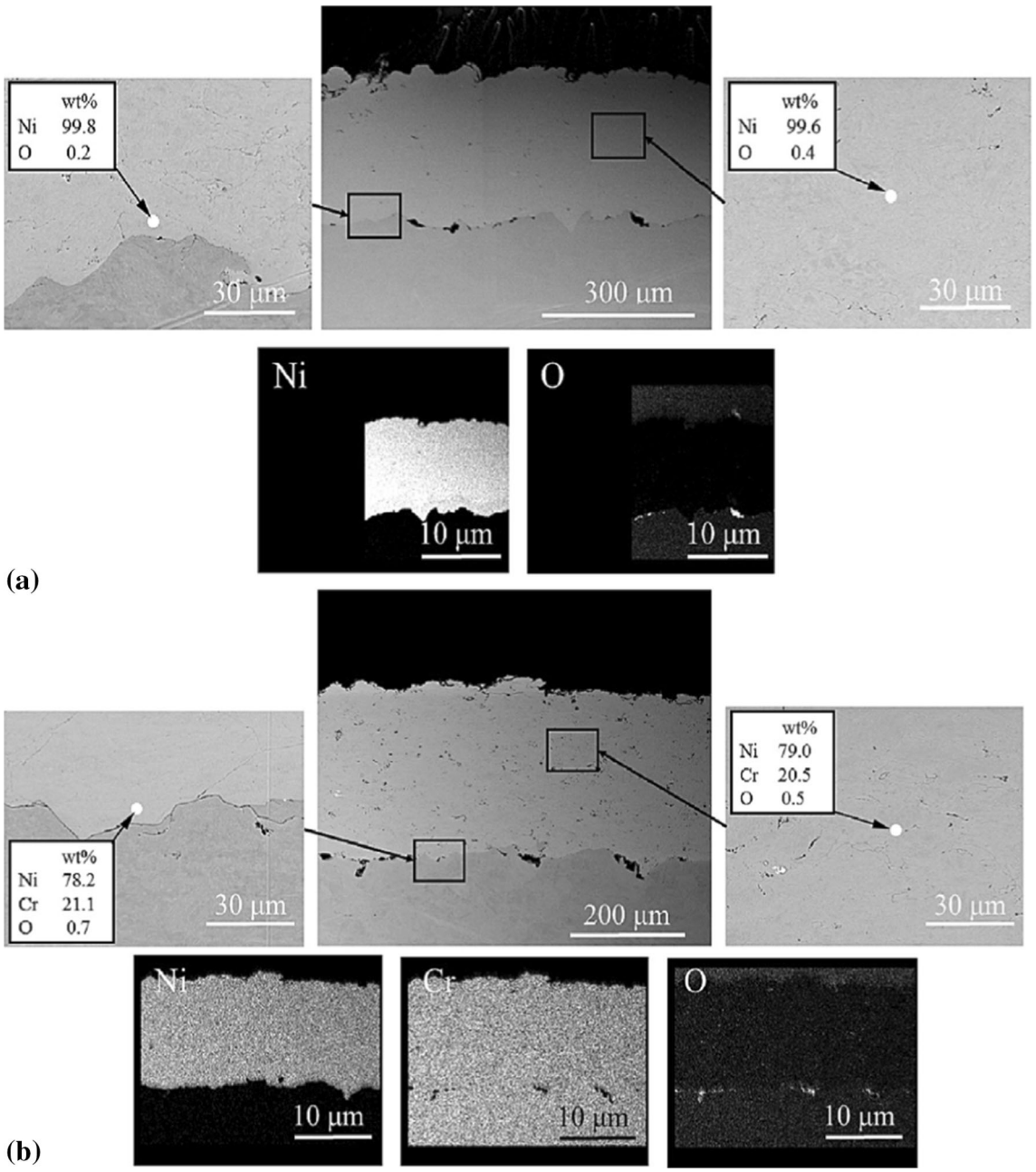


**Fig. 21** Cross-sectional SEM image (SE mode), EDX point and element mapping analysis of as-sprayed (a) Ni and (b) NiCr coatings deposited by HVAF (Ref 98). Reprinted with permission from Elsevier

the limited nucleation and growth of the deleterious NiO scale in the low-O-activity environment. No significant Cr depletion was observed in the exposed NiCr coating, which might be attributed to the presence of a high amount of Cr (21 wt.%) in the coating. The defects, e.g., lamellar boundaries and pores, in the NiCr coating served as preferential sites for the nucleation and growth of the oxide.

Uusitalo et al. (Ref 99) investigated the corrosion behavior of HVOF and laser-melted HVOF Ni-based coatings in a reducing Cl-containing atmosphere at 550 °C. The exposed HVOF coatings contained high amounts of Ni and Cr. Despite the high alloy content of the HVOF coatings, the substrates were attacked by Cl and S in many cases. The corrosive species penetrated the coating through an interconnected network of voids and oxides present at the splat boundaries. The corrosion resistance of the splat boundaries determined that of the HVOF coatings. The best HVOF coatings, however, were not penetrated by the corrosive species. The laser-melted HVOF coating did not suffer any corrosion damage during the tests. The

corresponding HVOF coating was penetrated by the corrosive species. The interconnected network of voids and oxides present at the splat boundaries of the HVOF coating was efficiently removed by laser melting, which proved to be an efficient method for improving the corrosion resistance of HVOF coatings.

### Role of Coating Architecture After the Addition of a Dispersed Oxide

Sadeghimeresht et al. (Ref 100) investigated Ni21Cr9Mo coatings with and without dispersed $SiO_2$ deposited by HVAF. As shown in Fig. 22, the $SiO_2$-containing coating revealed a lower weight change than the $SiO_2$-free coating, which was most probably due to the formation of a protective and adherent Cr-rich oxide scale. The oxide scale formed on the $SiO_2$-free coating was more porous and thicker; see Fig. 22(a), (b), (c), and (d). $SiO_2$ decelerated the short-circuit diffusion of $Cr^{3+}$ through the defects in the scale, e.g., vacancies, and promoted the selective oxidation of Cr to form the protective Cr-rich oxide scale. Furthermore, the presence of $SiO_2$ led to less subsurface depletion of Cr in the coating and accordingly less corrosion of the substrate. The corrosion product formed on the $SiO_2$-free coating was highly porous, non-adherent, and thick. The experimental results also showed that the effect of $SiO_2$ was even more significant once KCl was introduced. In the absence of the $SiO_2$ dispersoids, the formation of $NiCl_2$ was promoted; see Table 5. The adhesion of the scale to the coating was greatly improved, as no gap was observed at the interface. It was shown that a uniform supply of Cr to the formed oxide scale promoted the formation of a more continuous and denser Cr-rich scale that exhibited low growth kinetics and less spallation. Therefore, the formation of undesirable $K_2CrO_4$, which depletes Cr in $Cr_2O_3$, was interrupted, as KCl was locally consumed during the exposure. Moreover, the fast formation of an external Cr-rich scale as a result of the presence of homogenous $SiO_2$

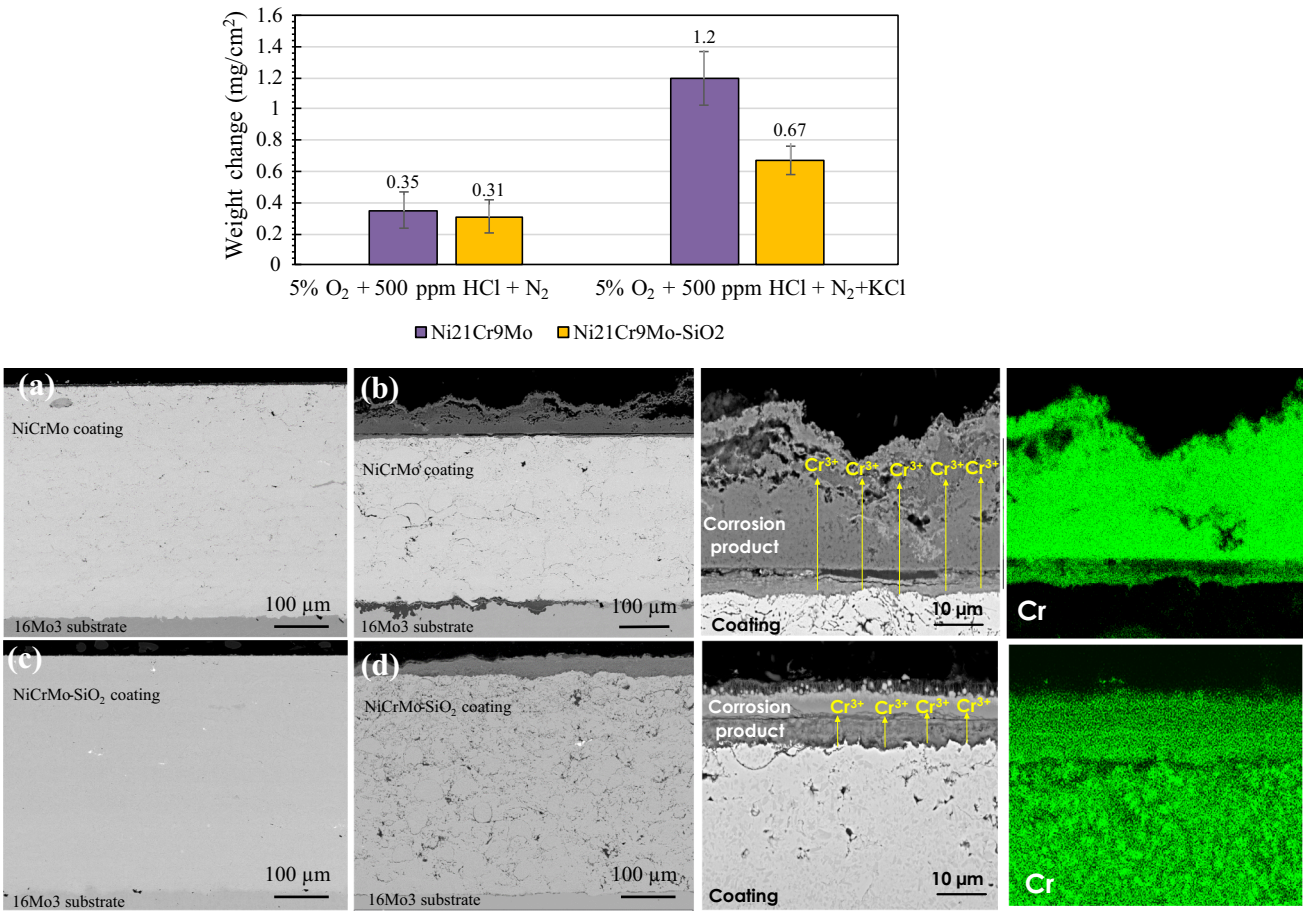


**Fig. 22** Weight changes in HVAF-sprayed Ni21Cr9Mo and Ni21Cr9Mo-$SiO_2$ coatings in an HCl-laden environment after 168 h of exposure with and without KCl, cross-sectional SEM images of four HVAF-sprayed coatings oxidized in 5 vol.% $O_2$ + 500 vppm HCl + $N_2$ at 600 °C for 168 h with and without KCl: (a) Ni21Cr9Mo without KCl, (b) Ni21Cr9Mo with KCl, (c) Ni21Cr9Mo-$SiO_2$ without KCl, and (d) Ni21Cr9Mo-$SiO_2$ with KCl, and back-scattered SEM images of the cross sections of exposed (a) NiCrMo and (b) NiCrMo-$SiO_2$ coatings in 5% $O_2$ + 500 ppm HCl + $N_2$ with KCl deposit for 168 h at 600 °C (Ref 100). Reprinted with permission from Elsevier

**Table 5** Corrosion products formed on the surfaces of $SiO_2$-containing and $SiO_2$-free coatings exposed to a HCl-laden environment for 168 h at 600 °C (Ref 100)

| Coatings | Corrosion products | |
|---|---|---|
| | Without KCl | With KCl |
| Ni21Cr9Mo | $MoO_3$, $NiCr_2O_4$ | $NiCl_2$, $NiCr_2O_4$ |
| Ni21Cr9Mo-$SiO_2$ | $MoO_3$, $NiCr_2O_4$ | $NiCr_2O_4$, $SiO_2$ |

resulted in notably enhanced corrosion resistance of the coating. The non-adherent scale on the $SiO_2$-free coating experienced fast grain growth.

By adding $SiO_2$ dispersoids to the NiCrMo coating, $Cr^{3+}$ was continuously and slowly supplied to the protective Cr-rich oxide scale formed in step 1 in Fig. 23. Therefore, the formation of $Cl^-$ and $K_2CrO_4$, which depletes the oxide scale of Cr, was slowed down. Consequently, less volatile metallic chlorides and voids were formed in the corrosion products developed on the coating. Several explanations have been proposed for the lower oxidation rate of the oxide-dispersed alloys (Ref 101-104). Stringer et al. (Ref 105) suggested that the dispersoids present on the surface act as oxide nucleation sites, and led to faster formation of a continuous $Cr_2O_3$ scale. Giggins and Pettit (Ref 106) showed by using a Pt marker that the position of the marker depends on the relative diffusion rates of the components involved, i.e., the outward diffusion of $Cr^{3+}$ and the inward diffusion of $O^{2-}$. They suggested that the slow outward diffusion of $Cr^{3+}$ might be caused by the blocking action of the dispersoids in the $Cr_2O_3$ scale. However, all these studies were performed in ambient air (without KCl) and did not focus on the formation of $Cl^-$ and $K_2CrO_4$ on the corrosion product developed. The dispersoids have a beneficial influence on scale adhesion, by the findings reported in the literature (Ref 107). This might be due to the thinner scale, which is more compliant with the coating.

## Role of Thickness

The coating thickness was reported to significantly influence the electrochemical corrosion behavior of a coated steel (Ref 108). A thin coating allows the electrolyte to easily migrate until it reaches the coating/substrate interface (Ref 109). Wang et al. (Ref 110) stated that the corrosion resistance of coatings increased following an increase in coating thickness from 120 to 400 μm. The reduced corrosion resistance observed in thinner coatings

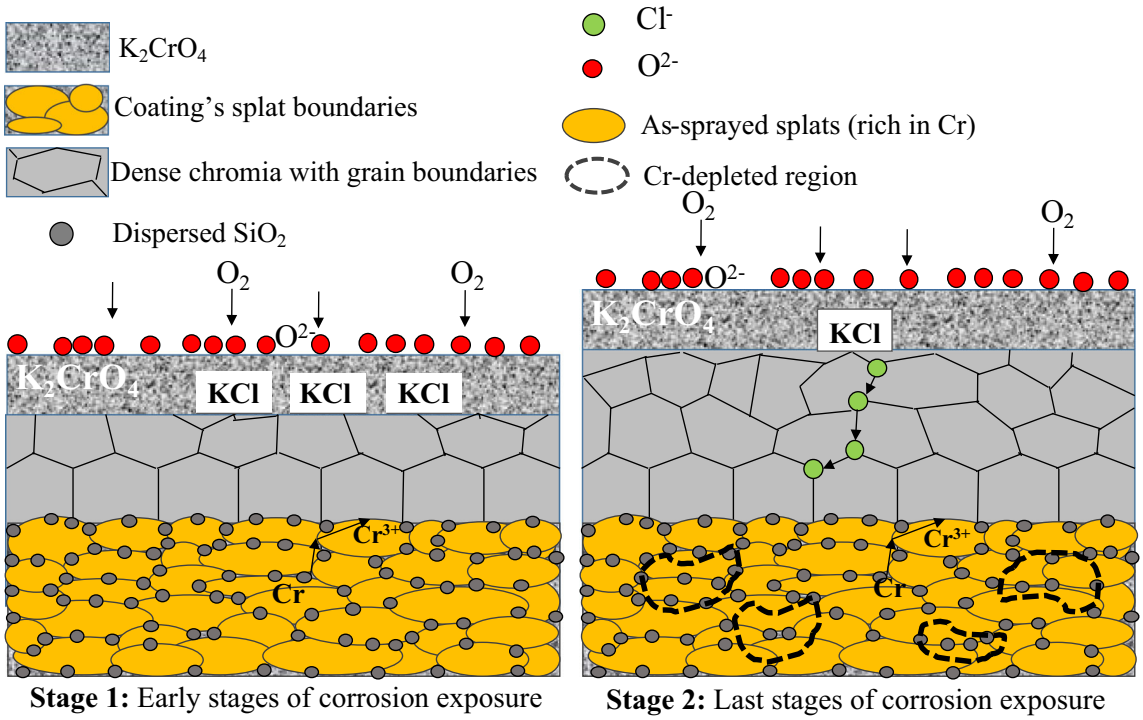


**Fig. 23** Schematic of the corrosion mechanism of a NiCrMo-$SiO_2$ coating exposed to 5% $O_2$ + 500 ppm HCl + $N_2$ with KCl deposit for 168 h at 600 °C. Dispersoids decelerated the formation of $Cl^-$ and $K_2CrO_4$ during the early stages. A random diffusion of $Cl^-$ within the oxide layer and a few Cr-depleted regions within the coating were observed; however, in general, the dispersoids succeeded in protecting the coating and, thereby, the substrate by promoting the formation of a dense and protective Cr-rich oxide scale (Ref 100). Reprinted with permission from Elsevier

was assumed to be associated with an easier formation of through-pores "channels" (by the connection of the individual pores) along with the thickness of the coating (Ref 111).

If a molten salt (electrolyte) reaches the coating/substrate interface, the corrosion reactions become more complex and generate more corrosion products due to the formation of galvanic pairs between the coating and the substrate. In this situation, a coating with a corrosion potential similar to that of the substrate is recommended. If the corrosion potential of the coating is lower, it will be corroded in the presence of the molten salt (Fig. 24a) but, if the coating has a higher corrosion potential, the substrate will be sacrificed (Fig. 24b). In the former case, the presence of defects in the coating is not of importance, as the coating will anyhow be corroded; however, in the latter case, the defects in the coating are highly important, and a defect-free coating is highly required. In general, spallation may be considered as the final step of service failure under the specified hot corrosion conditions for an insufficient thickness of the protective coating. By adding an intermediate layer to the coating (Fig. 24c), it was shown in many studies that the progress of corrosion can be controlled (Ref 112-116).

### Bi-Layer Coating Architecture

In a bi-layer coating, as shown in Fig. 24(d), after the electrolyte (like a molten salt) penetrates the top coat and reaches the top/bond coat interface, the corrosion occurring is variably associated with the properties of the bond coat (Ref 112-119). The top coat in the bi-layer coating, similar to that in a single-layer coating, usually displays insufficient interlamellar cohesion, which is favorable for the corrosive species to reach the top coat/bond coat interface. The splat boundaries in the top coat are slightly deteriorated; however, the bond coat prevents the corrosion of the substrate (Ref 120). Consistent with the previous explanation, the intersplat bonding is critical to the corrosion resistance of thermally sprayed samples owing to several factors: Initially, when defects such as porosity or weak intersplat cohesion are present in coatings, they act as

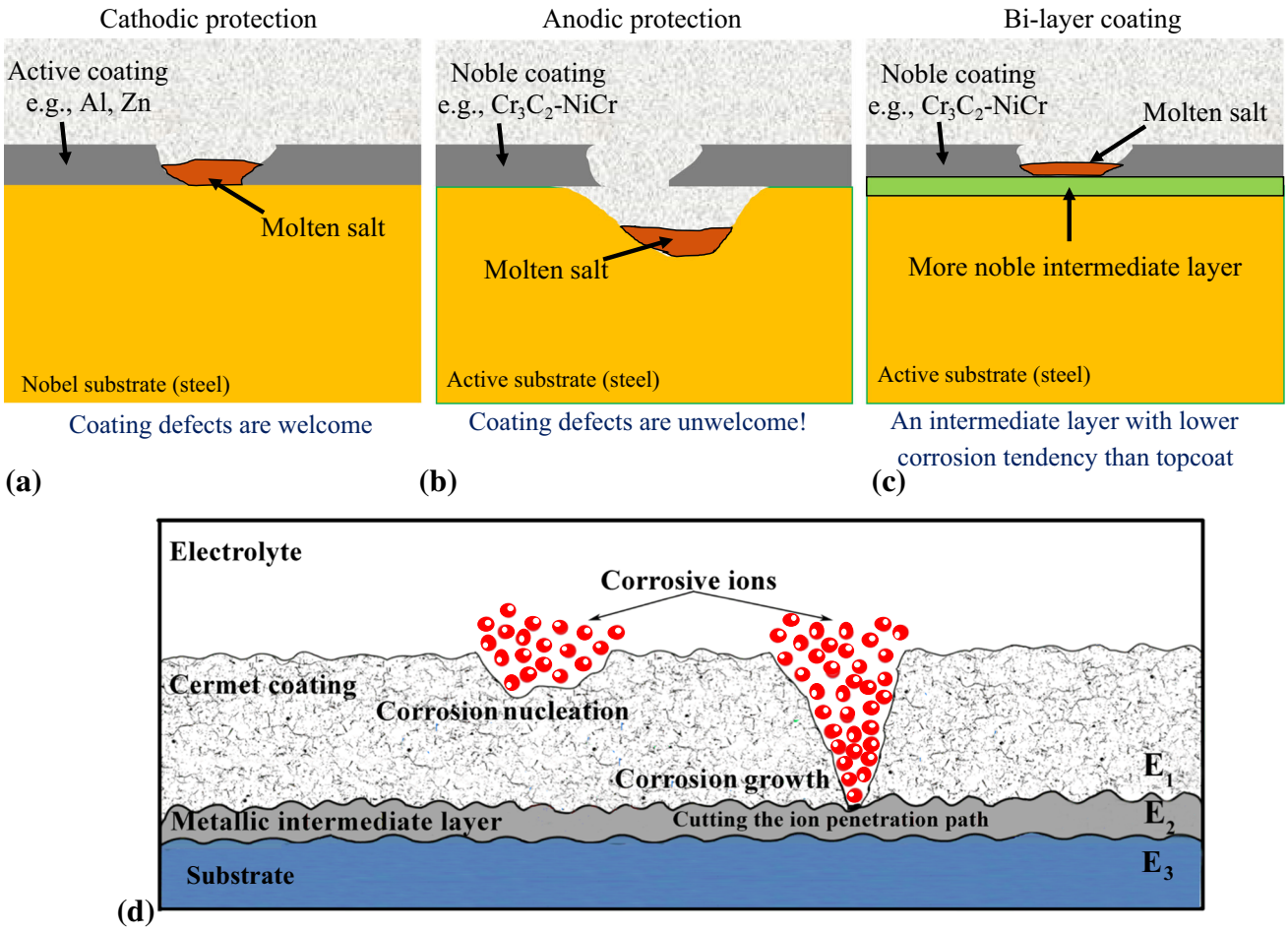


**Fig. 24** Types of coating and substrate failures according to their corrosion potential: (a) cathodic protection, (b) anodic protection, (c) bi-layer coating, and (d) effect of the corrosion potential in the top coat and bond coat layers (Ref 112)

preferential nucleation sites for corrosion. In a bi-layer coating, the bond coat, which is typically a metal, promotes intersplat cohesion, and results in higher density, lower oxide content, and lower porosity. The molten salt fails to easily penetrate the splat boundaries of the bond coat; therefore, the top coat/bond coat interface acts as an additional barrier in preventing the corrosion of the substrate. Moreover, it permits the formation of galvanic cells between the anodic substrate and the cathodic top coat, since the top coat is more cathodic than the steel substrate. Furthermore, the standard reduction potential of the bond coat is supposed to be between those of the substrate and the top coat. The corrosion tendency of each layer in a multilayer coating can be evaluated by electrochemical techniques such as polarization and electrochemical impedance spectroscopy (EIS), which have not been fully explored yet.

Wu et al. (Ref 121) deposited a single-layer Ni and a multilayer $Ni_2Al_3$/Ni coating, which were protective in a wood-fired plant where the outlet steam temperature was 520 °C. However, in a plant that fired straw at the outlet steam temperature of 540 °C and where severe thermal cycling took place, both the Ni and $Ni_2Al_3$ coatings failed. This highlights the differences between the two biomass plants and suggests that a coating solution has to be tailored to the operating conditions of a specific boiler.

### Role of Temperature

According to Lee et al. (Ref 122), the operating temperature of the combustion chamber, the metal surface temperature, and its local fluctuations disrupt the protective oxide layer and affect the corrosion rate of boilers. First, the high temperature of the metal surface, due to high radiation fluxes and/or inadequate heat transfer to the steam flowing inside the tube, results in melting of deposits and acceleration of corrosion rate. In general, the metal temperatures of the water wall and superheater tubes in WtE boilers are maintained below 300 and 450 °C, respectively (Ref 123). However, operation at higher superheater temperatures increases the thermal efficiency of the steam turbine. Secondly, the temperature of the combustion gases can affect the deposition rates and also the composition of the deposit, and thus accelerate corrosion. The gradient between the gas temperature and the metal surface temperature is a driving force for the condensation of vaporized species, such as metal chlorides, on the cooled surface (Ref 124). When the temperature gradient is large, the chloride concentration in the deposit is high and the melting point of the salt decreases. In addition, the thermal stresses induced by the temperature gradient across the deposit and the metal wall can affect the adhesion of the oxide scales on the metal surface, thereby resulting in the fracture of the protective oxide layer, followed by spalling and an increase in point defect diffusion within the oxide scales (Ref 125, 126). Thirdly, the non-homogeneous physical and chemical compositions of the MSW fuel and the corresponding fluctuations in the heating value with time result in pronounced fluctuations of the gas temperature within the combustion chamber. Experimental studies have confirmed that the corrosion rate increases several times because of the wide temperature fluctuations (Ref 127).

Oksa et al. (Ref 76) tested HVOF-sprayed NiCr, Alloy 625, Ni21Cr10W9Mo4Cu, and Fe25Cr15W12Nb6Mo coatings in NaCl-KCl-$Na_2SO_4$ salt under controlled $H_2O$ atmosphere at two different temperatures 575 and 625 °C. It was shown that the effect of test temperature was contradictory. The NiCr coatings showed similar deposits for the two different temperatures. In Alloy 625, the oxide layer was thicker at 575 °C and mainly rich in Fe. A thin Cr-rich oxide layer was observed at 625 °C. In Ni21Cr10W9Mo4Cu, a thin oxide containing Ni, Cr, Mo, and W was formed at 575 °C. A detached Cu-rich oxide particle was detected on the surface. At 625 °C, a slightly thicker oxide layer rich in Ni, Cr, Cu, and Nb was formed. The outer surface of the coating was depleted of Ni and enriched with Mo and W. In Fe25Cr15W12Nb6Mo, a small amount of Cl was present in the oxide and at the outer surface of the coating exposed at 575 °C. The iron oxide layer on this coating consisted of small amounts of Cr, Si, Mn, Mo, and Nb. The coating showed a very good corrosion resistance at both the test temperatures. It was shown in some cases that the lower temperature (575 °C) was highly detrimental. Similar results have been reported in the temperature range 500-650 °C under alkali salt deposits (Ref 85, 128, 129) but no clear explanation of the phenomenon has been given. Paul et al. (Ref 85) suggested that the reason for the better corrosion resistance at higher temperatures was the change in the predominant corrosion mechanism from molten-salt corrosion to gaseous corrosion. Most probably, the reason is derived from the sulfate–chloride chemistry and the ability of the metal or the alloying elements to form a protective oxide in the prevailing conditions (Ref 130, 131). It is assumed that the 50 °C increase in temperature may have enhanced the vaporization of Cl, and the gas flow during the test could have decreased the amount of Cl available for the corrosion process. Based on thermodynamic calculations performed by using FactSage 6.2, the melting point of the salt mixture is 517 °C. The amount of vaporized Cl (and K) increases, even though the amount is very small. The kinetics of the process are difficult to estimate, because mass transfer constraints the vaporization process. Another explanation may be the higher diffusion rate of Cr or other protective component to form a more protective scale on the alloy,

which could have retarded the corrosion process. This is supported by the higher amounts of Cr present in the oxide layers at 625 °C, compared to those observed at the lower temperature.

### Role of Substrate

The effect of substrate on the high-temperature corrosion behavior of the coatings in boilers has not been investigated. However, it has been extensively studied for gas turbine applications. The lack of studies about boiler applications might be mainly attributable to the lower operating temperatures of boilers (< 700 °C), in which the microstructure and composition of the substrate are not significantly affected. During high-temperature exposure under molten salts, if the corrosion ions diffuse and reach the substrate, galvanic cells between the coating and the substrate might form, which can further accelerate the corrosion of the coating or the substrate, depending on which one has the lower corrosion potential. It has been recommended by Porcayo-Calderón et al. (Ref 132) that to avoid the occurrence of galvanic corrosion through the diffusion of molten salts ($ZnCl_2$-KCl) toward the substrate through an HVOF-sprayed Ni21Cr coating, a high coating thickness (500 μm) is required. In addition, the CTE of the coating should be close to that of the underlying substrate to withstand the thermal fluctuations encountered during start-ups, shutdowns, and the boiler operation itself without cracking, which can be caused by a CTE mismatch. The CTE (from 20 to 600 °C) for NiCr is $\sim 14 \times 10^{-6}$/ °C, for NiCrAlY is $\sim 12 \times 10^{-6}$/ °C, for Alloy 625 is $\sim$ 13-16 $\times 10^{-6}$/°C, and for Fe19Cr is $\sim 10 \times 10^{-6}$/ °C (Ref 133), compared to 10-14 $\times 10^{-6}$/°C for ferritic steels, which are the typical boiler materials.

### Role of Post-Treatment

Post-treatment consists of processes in which the microstructure or/and composition of a component is altered. It can include heat treatment, polishing, grit blasting, shot peening, or laser remelting. Applying appropriate surface treatment processes on thermal spray coatings to increase the coating durability has been a target for many researchers over the last few decades (Ref 134). Such post-treatments modify the surface conditions and are thus expected to affect the oxidation behavior of coatings. It has been reported that shot peening can strongly influence oxidation behavior by promoting the fast formation of protective α-$Al_2O_3$ scale layers on the surfaces of MCrAlY (M = Ni, Co, or/and Fe) and NiAl coatings and by reducing oxide scale spallation (Ref 135-137). Similarly, it has been reported that grit blasting of the coated specimen favored α-$Al_2O_3$ formation due to formation of uniform surface roughness on the coating surface (Ref 136, 138-140). However, a negative effect can be observed in the form of introduction of contaminants on the treated surface during the grit blasting process, which accelerates oxide growth (Ref 141). On the contrary, the use of glass balls showed no such negative effect (Ref 142). In a previous study on the oxidation of HVAF-sprayed NiCoCrAlY coatings for up to 1000 h at 1000 °C (Ref 143), it has been shown that shot-peening treatment can improve coating performance by reducing α-$Al_2O_3$ growth rate and suppressing the formation of detrimental spinels. Such positive effects can be attributed to the fact that the impingement of particles on the coating modifies the microstructure near the surface by introducing more dislocations and grain boundaries. Such structural features offer "short-circuit" paths for the diffusion of Al to the oxidation front and thus aid the rapid formation of the protective alumina scale on the surface during the initial oxidation stage. Hence, in addition to the scientific interest, studying the effect of surface treatments on the initial oxidation stage is also important from an application standpoint for developing post-deposition treatments for enhancing the long-term oxidation behavior of MCrAlY (M = Ni, Co, or/and Fe) coatings. Deng et al. (Ref 144) investigated the surface microstructure and high-temperature oxidation resistance of an APS-deposited NiCoCrAlY coating modified by cathode plasma electrolysis (CPE). It was shown that a remelted layer without any oxide stringers or pores was formed on the modified sample. The grain size of the remelted layer was approximately 80-120 nm. Selective oxidation of Al avoided the formation of other oxides. An oxide scale mainly composed of $Al_2O_3$ was formed on the modified sample. Such beneficial results can be attributed to following effects: During the CPE process, plasma discharge at a high temperature is observed on the bond coat surface. As a result of the plasma discharge, the surface is melted and quickly resolidified, as a result of which the grain size decreases and the pores and oxide stringers disappear. During cyclic oxidation, owing to the above-mentioned modification of the surface properties, the critical content of Al required for selective oxidation is significantly decreased. Therefore, a continuous $Al_2O_3$ scale is formed. Fernandez et al. (Ref 145) investigated laser-treated APS-deposited Cr-Ni coatings under the oxidative atmosphere containing 3.0-3.5 vol.% of $O_2$ at 500 and 800 °C, to which steam boilers are typically exposed. By using laser processing, low porosity and homogeneous coating were obtained. Using laser cladding or laser surface treatment, the oxides were separated from the bare alloy, making the nodules rise to the surface. The superior oxidation resistance of the laser-treated coating compared to those of the uncoated substrate and the plasma-sprayed coating was ascribed to the formation of a coating without

pores and to the formation of a thin oxidized protective film.

After the completion of the coating step, additional heat treatments are sometimes performed to obtain the desired microstructure and phase distribution in the coating. Moreover, optimization of the coating/substrate bonding as well as the coating and substrate properties may require additional heat treatments. The residual stresses are also relaxed, and interparticle cohesion is increased. Figure 25 shows the retention of some unmelted and/or resolidified particles in as-sprayed Fe- and Co-based coatings, which led to lower deposit cohesive strengths. As a result of heat treatment, the Fe-based coating is affected more, particularly after 3 h at 900 °C in vacuum. An inappropriate selection of the parameters during heat treatment (time, temperature, and environment) may lead to an even worse microstructure with a high level of pores and oxides as well as delamination at the coating/substrate interface (Ref 146).

## Laboratory Corrosion Test Procedures

Simplified laboratory test setups are effective for comparing and evaluating the corrosion tendencies of materials over a short period, because only a few of the corrosion factors are involved. However, the results obtained are difficult to apply in the evaluation of the long-term corrosion lifetime of materials, because such simplified tests only account for relatively moderate corrosion environments, which make it difficult to exactly anticipate the corrosion rates experienced in actual conditions. The factors that are difficult to reproduce in laboratories include (i) the various fluctuations in the temperature and chemical composition of the combustion gas, and (ii) the heat transfer rates and temperature gradients ($\Delta T$) observed in boilers and heat exchangers. It is well known that these dynamic factors are closely related to the breakdown of the protective oxide scales that form on material surfaces, which increases the corrosion rates. Therefore, the effect of these factors has been investigated in detail, particularly, in the fields of high-temperature oxidation and gaseous corrosion. On the other hand, in the field of high-temperature corrosion, investigations have been carried out only by using large-scale equipment, such as burner-rig tests. In addition, it has been noted that the factors indicated in (ii) strongly influence the deposition behaviors and deposition rates of the corrosive ash components contained in the combustion gas of fossil fuels or waste. Accordingly, these factors are considered to be very important, because they relate closely to the corrosion rates.

Two approaches are commonly used to study the corrosion kinetics of materials in laboratory: measuring the change in the weight of the exposed samples or calculating the thickness of the oxide scale (corrosion product). Two techniques are used for measuring the weight changes in the coatings before and after corrosion exposures. First, freestanding coatings can be produced by removing the substrate to prevent the effect of the substrate on the high-temperature corrosion kinetics of the coatings; see Fig. 26(a). To fabricate a freestanding coating, the

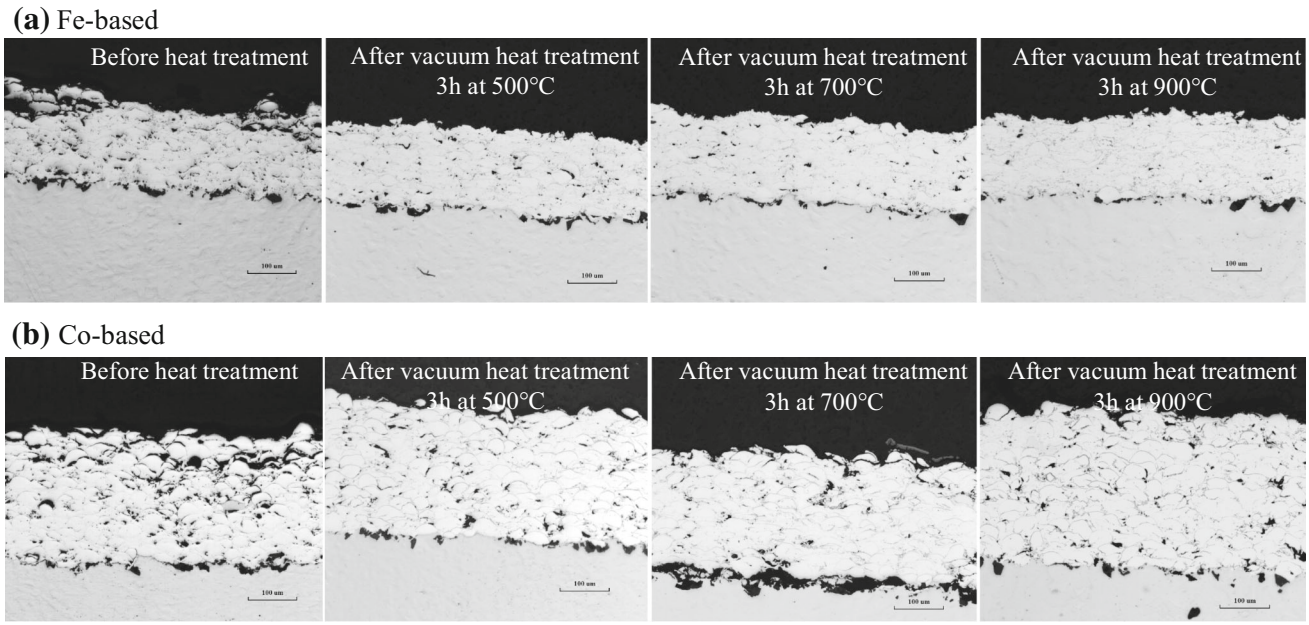


**Fig. 25** Effect of heat treatment in different conditions on (a) HVAF-sprayed Fe-based coating and (b) HVAF-sprayed Co-based coating. The SEM images in the as-sprayed conditions which are reprinted with permission from Elsevier are sourced from (Ref 146)

substrate can be first mechanically cut at a low speed at a location close to the coating/substrate interface. The remnant substrate can then be manually ground and polished until only the coating remains. The second method is to apply the coating on all the surfaces of the specimen to prevent the contact of the corrosive atmosphere with the substrate. Thus, the total weight change in the coating/substrate system will be equal to the weight change in the coating. To coat all the specimen's surfaces, usually a rod of the substrate material is fixed in a horizontal rotating mandrel to first coat the cylindrical surface; see Fig. 26(b). The rod can then be sliced into buttons (step A in Fig. 26b), and both the flat surfaces of the buttons can be grit-blasted first (step B in Fig. 26b) and thermally sprayed (step C in Fig. 26b) subsequently to ensure that the substrates have been coated on all the sides. Before the corrosion test, all the surfaces of the investigated samples can be polished to obtain uniform surface roughness.

To evaluate corrosion in a laboratory, simplified high-temperature corrosion tests such as the salt-embedded or salt-spraying method have been used, depending on the purpose. Jafari and Sadeghimeresht et al. (Ref 57) first dissolved KCl in an ethanol/water mixture to form a saturated solution, and then they sprayed the mixture onto the polished samples to form 0.1 mg/cm$^2$ deposits. Sadeghimeresht et al. (Ref 87, 88, 100) initially prepared a KCl suspension by dissolving in ethanol (not saturated). The deposit ($\sim$ 0.1 mg/cm$^2$) was then applied onto the surfaces of the polished samples by using a paintbrush. Fantozzi et al. (Ref 62) carried out the test according to the ISO standard 17224:2015 (E) (Ref 147). First, freestanding coatings (i.e., coatings without the substrates) were prepared. These coatings were placed in separate alumina crucibles containing KCl salt. The coatings were partially immersed in the KCl deposit, so that a small part of the coating was not in contact with the salt, as schematically shown in Fig. 26(c). This configuration enables the direct observation of the degradation of the coatings exposed to the salt, which can be compared with that of the unexposed parts. Knowledge of the corrosion test procedure followed in each study enables the other researchers to understand the reasons for the dissimilarities in the results.

Considering the above-mentioned conditions, with the aim of improving the accuracy of laboratory high-temperature corrosion tests and evaluating the corrosion lifetimes of various materials more easily and quickly, a new temperature gradient test (TGT) with a thermal cycle component has been developed (Ref 148). The application of the TGT is mainly for waste combustion environments, in which thermal cycles and $\Delta$Ts strongly influence corrosion.

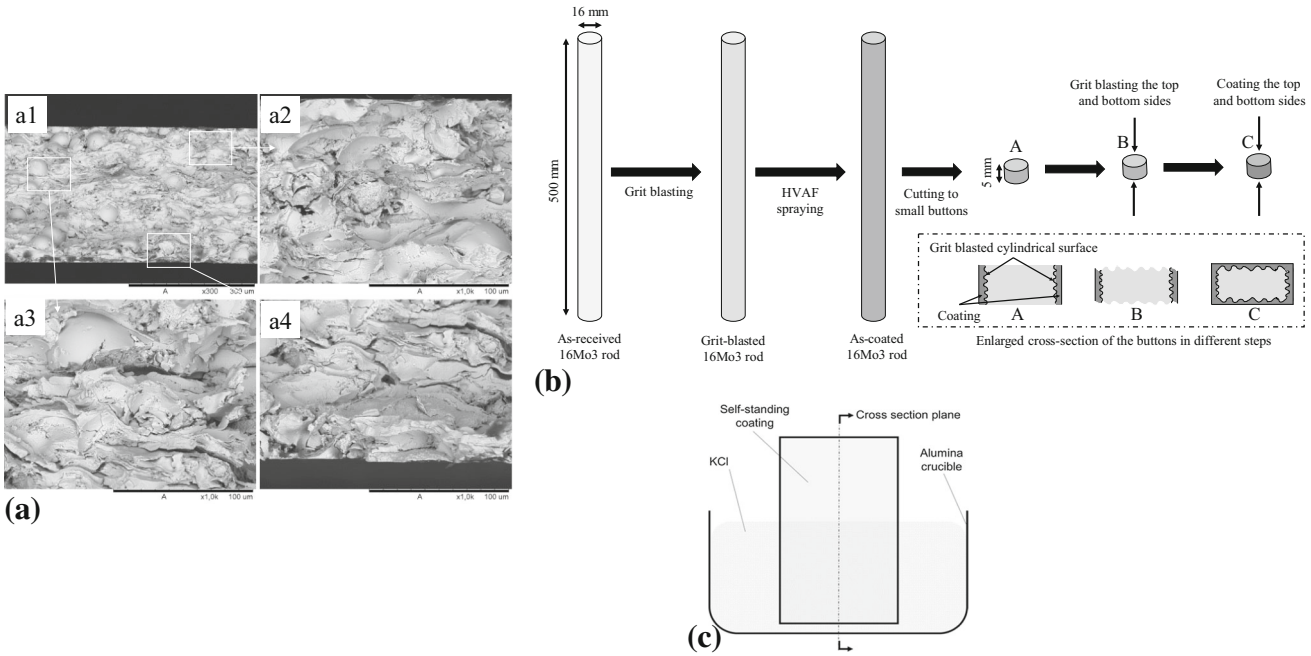


**Fig. 26** (a) Fractured surfaces of HVAF- and HVOF-sprayed amorphous Fe-based coatings: (a1) HVAF coating at a low magnification, (a2) HVAF coating at a high magnification, (a3) HVOF coating at a low magnification, (a4) HVOF coating at a high magnification; (b) schematic view of the procedure followed to produce fully coated specimens. A 16Mo3 rod with the length of 500 mm and diameter of 16 mm was first grit-blasted and then coated by using the HVAF process. The coated rod was then sliced to small buttons with a thickness of 5 mm (step A). The two flat surfaces (top and bottom) of the buttons were grit-blasted (step B) and then coated (step C). Special attention was paid to the corners of the buttons to avoid any damage during the cutting, grit blasting, and spraying (Ref 87); and (c) preparation of a KCl suspension in ethanol, with the deposit ($\sim$ 0.1 mg/cm$^2$) applied on the surface of the sample by using a paintbrush (Ref 62). Reprinted with permission from Elsevier

To clarify the fundamental corrosion behavior, especially with regard to the protective oxide layers of materials, through TGTs with a thermal cycle component, a basic investigation is being carried out to study the influences of the applied thermal parameters. Furthermore, the long-term corrosion lifetimes are evaluated by using the TGT results, and the values obtained from the laboratory tests and practical WtE boilers are compared. In addition, the applicability of TGTs and the corrosion mechanisms of WtE boiler materials are being studied by integrating the above results.

In a more complex condition, the laboratory tests were performed by using two different synthetic deposit materials that were applied on an air-cooled probe on adjacent alloy samples that were separated by a heat-resistant barrier; see Fig. 27(a). The first deposit was always $PbCl_2$, whereas the other one was either a NaCl, $Na_2SO_4$, KCl, $K_2SO_4$, KCl-NaCl mixture or inert $SiO_2$. Although, in a boiler environment, other ash-forming elements are also likely to affect the behavior of $PbCl_2$, this setup concentrates on a simplified system to gain a better understanding of the phenomena. The focus was on studying the vaporization, condensation, and reactivity of the $PbCl_2$ present in the other deposit (Ref 36). Two different material temperatures (200 and 400 °C) were selected to examine the effect of temperature and temperature gradient on the gas-phase migration of chlorides and their reaction with the other component, leading to the possible formation of a melt. The higher steel temperature (400 °C) was chosen to represent the typical superheater temperature in waste-fired boiler units, while the lower temperature (200 °C) was chosen for performing a comparison. The deposit reactions and corrosion results are summarized in Fig. 27(b). The results showed no increase in corrosion when the material temperature was 200 °C, whereas all the deposit materials were found to be extremely corrosive at 400 °C, when using C steel. The most corrosive agent was pure $PbCl_2$ salt. Thus, the highest corrosion rates were detected in the case of the deposits that did not react with $PbCl_2$ (i.e., $SiO_2$ and NaCl). The gradient furnace testing method proved to be a practical tool for further corrosion studies related to the laboratory-scale testing of superheater materials and deposit chemistry.

### Actual Boiler Exposures

VTT Technical Research Centre of Finland has extensively studied thermal spray coatings exposed to actual boilers fed with biomass fuels. Oksa et al. (Ref 133) investigated three HVOF-sprayed Ni-based (Ni24Cr16.5Mo, Ni22Cr-b5Fe9Mo4Nb and Ni22Cr10Al1Y) coatings in a 40 MW circulating fluidized bed (CFB) boiler, which mainly used wood as the fuel, over 2 years. The coated tubes were installed in the cold and hot economizer zones; see Fig. 28. Tube failure mainly occurred through Cl-induced corrosion. The corrosion was probably enhanced by the presence of KCl-$ZnCl_2$ and a high content of water vapor in the fuel. The C steel tube strongly corroded during the two-year exposure in the boiler that mainly burned wood with high moisture content. Zn and Pb were identified in the deposits. It is suggested that the extremely severe corrosion of the C steel is Cl-induced, apart from being the effect of the presence of K, Cu, Zn, and Pb in the deposits. HVOF-sprayed NiCr16Mo, NiCr9Mo, and NiCr10Al coatings revealed high corrosion resistance in the boiler during the exposure period; see Fig. 28. Corrosion attack in the coatings mainly occurred through the splat boundaries and pores. Therefore, to minimize the porosity and ensure sufficient melting of the particles, as well as achieve excellent cohesion and minimize the oxidation of the splats with a satisfactory velocity of the powder particles, optimization of the coating microstructure is suggested as being highly important.

In another work, Oksa et al. (Ref 55) studied two HVOF-sprayed Fe-based coatings (Fe27Cr and Fe19Cr) exposed to similar boiler conditions; see Fig. 29. The coatings were deposited on small tube sections, which were welded to the main boiler tubes. The coatings were then mounted onto the hot economizer. Even though the temperatures of the material on the boiler were low, the prevailing corrosion conditions caused severe damage to the C steel tubes. During the exposure period, the actual boiler tubes even lost several millimeters of their thicknesses. Thick corrosion products were mainly formed on the leeward side, and severe pitting was observed on the windward side. The coatings withstood the boiler environment very well, and the Fe-27Cr coating displayed excellent protection of the substrate material; see Fig. 29. The Fe-19Cr coating revealed sufficient corrosion resistance in the boiler conditions investigated. However, the Fe-19Cr coating exhibited a few perpendicular cracks suggesting that the underlying material had corroded slightly.

Oksa et al. (Ref 149) investigated four HVOF and one arc-sprayed coatings exposed to actual biomass co-fired boiler with a probe measurement installation in the superheated zone (see Fig. 30a) for 5900 h at 550 and 750 °C. The coating materials were Ni-Cr, Alloy 625, Fe-Cr-W-Nb-Mo, and Ni-Cr-Ti; see Fig. 30(b). Two different HVOF spray guns CJS and DJ hybrid were used to compare the corrosion resistance of the Ni-Cr coating microstructures. The ferritic steel T92 and the nickel super alloy A263 were used as the reference materials. The CFB boiler burnt a mixture of wood, peat, and coal. The coatings showed excellent corrosion resistance at 550 °C compared to that of the ferritic steel. At 750 °C, the CJS-sprayed coating showed better corrosion resistance than the DJ-sprayed

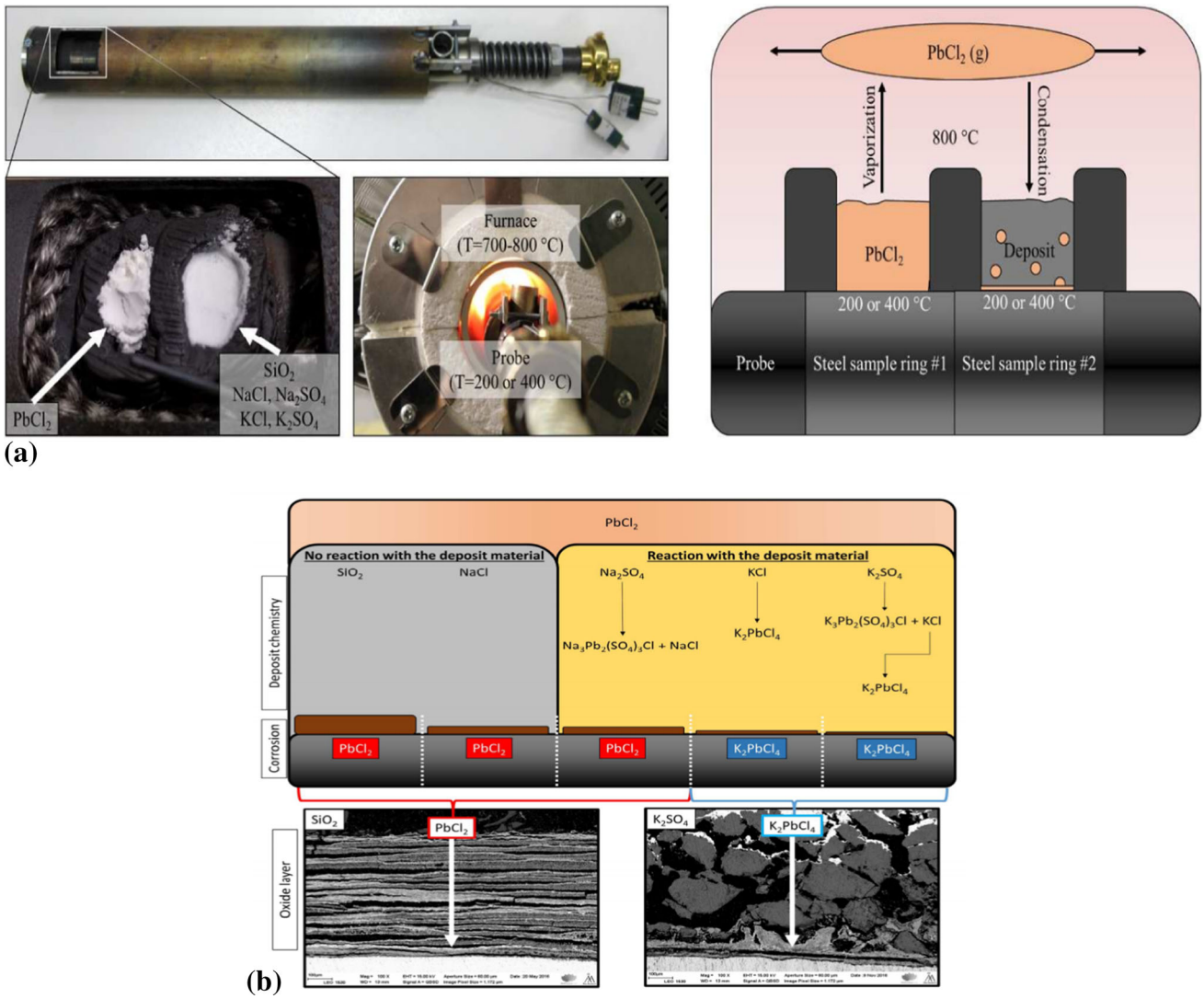


**Fig. 27** (a) The experimental setup is shown on the left, revealing a probe with deposit-covered sample rings and the probe in a tube furnace. On the right is a schematic representation of the experimental configuration; and (b) a summary of the deposit chemistry and the corrosion results (Ref 36). Reprinted with permission from Elsevier

coating; see Fig. 30(c) and (d). Alloy 625 was completely corroded during the exposure at 750 °C.

Oksa et al. (Ref 150) studied five different thermal spray coatings (Fig. 31a) in an actual biomass co-fired boiler for 1300 h by using a measurement probe. The coated probe before and after the corrosion exposures is shown in Fig. 31(b). At 550 °C, the coatings showed excellent corrosion performances compared to the reference ferritic steel T92 (Fig. 31c and d). At 750 °C, the tube material A263, together with NiCr and NiCrTi, exhibited the highest corrosion resistance (Fig. 31e). It was concluded that thermal spray coatings can offer substantial corrosion protection in biomass and recycled fuel burning power plants.

Bala et al. (Ref 151) investigated HVOF- and cold-sprayed Ni20Cr coatings (see Fig. 32) that were subjected to cyclic exposures in the superheated zone of a coal-fired boiler for 15 cycles. Both the HVOF- and cold-sprayed coatings were successful in reducing the high-temperature corrosion rate of T22 steel. The coatings were found to retain their surface contacts with the substrates, without any signs of scale spallation. The HVOF-sprayed Ni20Cr coating performed better than its cold-sprayed counterpart in an actual boiler environment, which might be attributed to the presence of a continuous protective $Cr_2O_3$ layer in the case of the former.

Bala et al. (Ref 152) also investigated cold-sprayed NiCr, NiCrTiC, and NiCrTiCRe coatings. The performances of the coatings were evaluated in actual boiler conditions, to which uncoated and coated steels were exposed in the superheated zone of a coal-fired boiler for 15 cycles. It was observed that the coated specimen

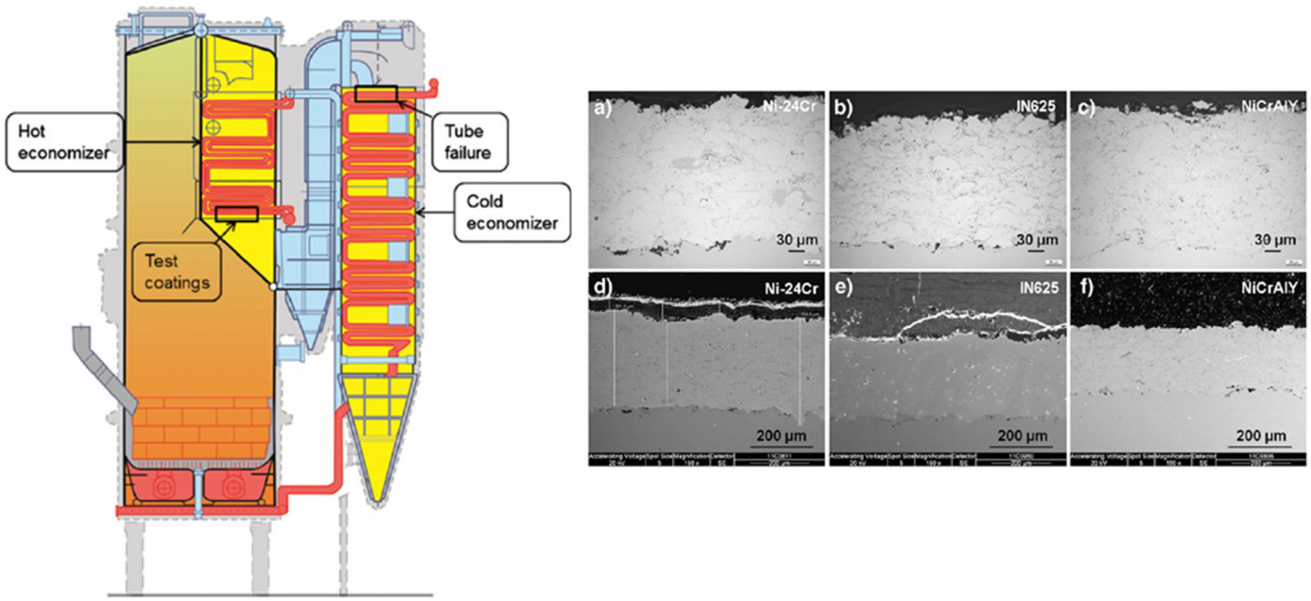


**Fig. 28** Schematic view of CFB boiler design. The locations of the test coatings in the economizers and the tube failure are shown in the figure. SEM images of the cross sections of the coatings after two-year exposure: HVOF-sprayed (a) NiCr16Mo, (b) NiCr16Mo, and (c) NiCr16Mo: (d) NiCr16Mo, (e) NiCr16Mo, and (f) NiCr16Mo (Ref 133). Reprinted with permission from Elsevier

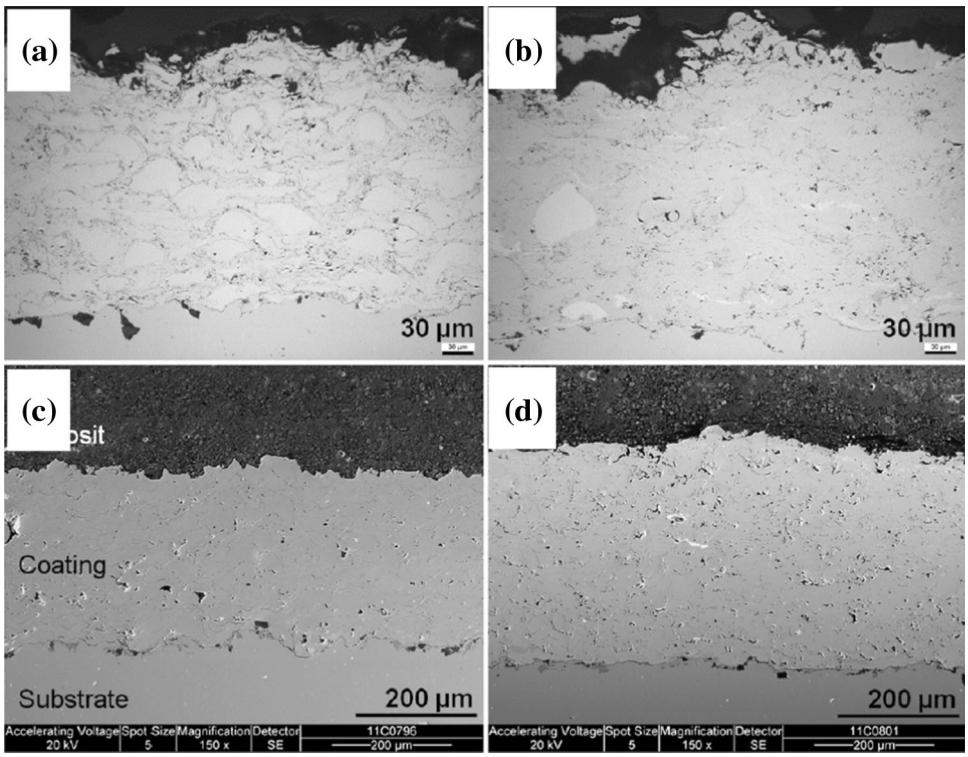


**Fig. 29** SEM images of the cross sections of HVOF-sprayed coatings: (a) as-sprayed Fe-27Cr, (b) as-sprayed Fe-19Cr, (c) exposed Fe-27Cr, and (d) exposed Fe-19Cr (Ref 55). Reprinted with permission from Elsevier

exhibited a better corrosion performance than the bare steel. The formation of oxides and spinels of Ni and Cr might have resulted in the better corrosion performance of the coatings. The NiCrTiCRe coating showed the best corrosion resistance among all the investigated specimens.

A summary of high-temperature corrosion studies on a few thermal spray coatings in environments simulating biomass-fired boiler conditions is given in Table 6.

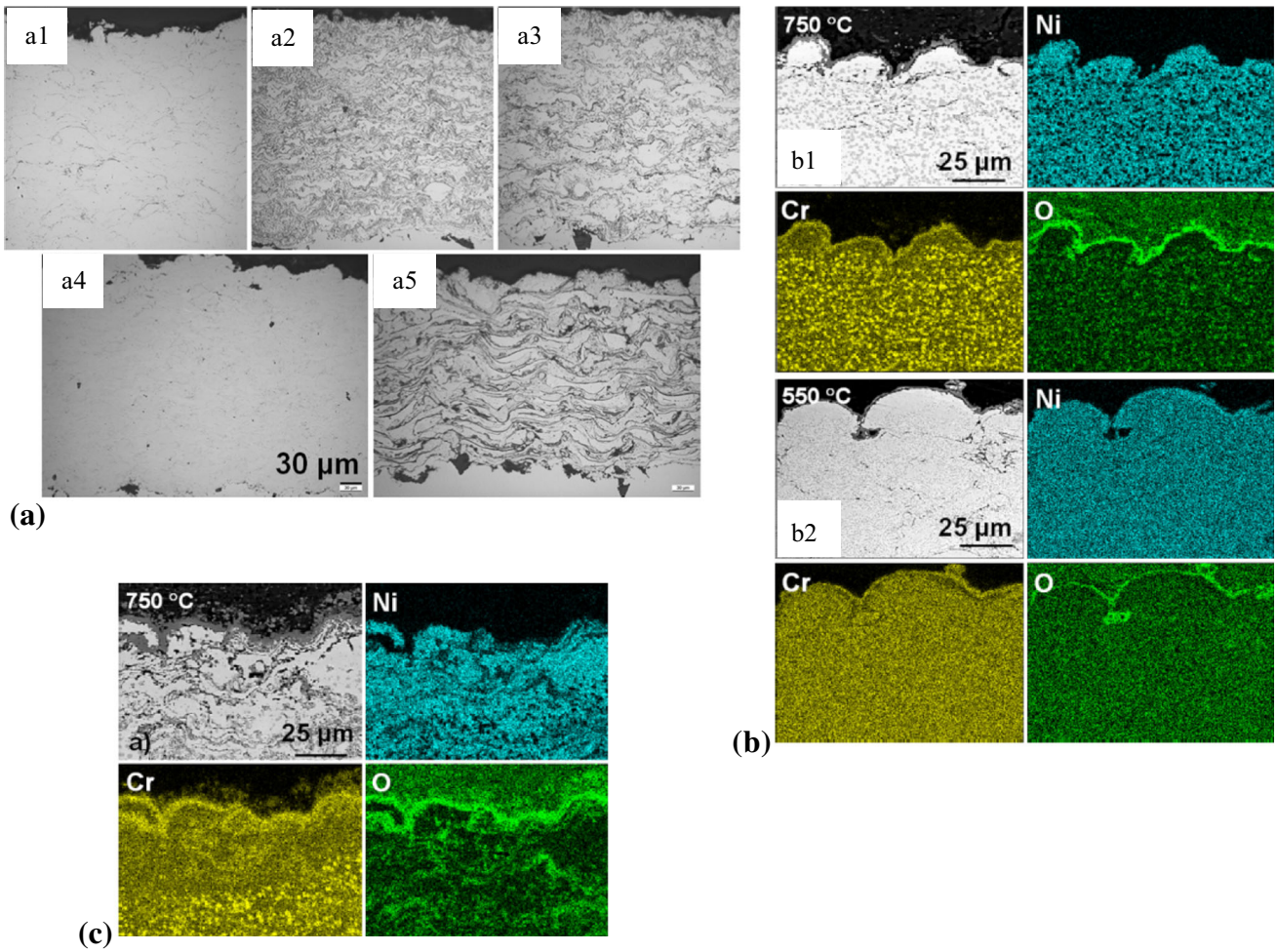


**Fig. 30** A 550 MWth CFB boiler test facility along with the location of the probe measurement system is shown, (a) SEM images of as-sprayed coatings: (a1) NiCr-F CJS, (a2) NiCr-C DJ, (a3) Alloy 625 DJ, (a4) FeCr CJS, and (a5) NiCrTi. The scale bar is the same, 30 µm, for all the images; (b) EDX maps of the coating NiCr-F CJS after exposures at (b1) 750 °C and (b2) 550 °C. For the outer surface of the coating, the elemental maps of Ni, Cr, and O are shown; (c) EDX map of the coating NiCr-C DJ after the exposure at 750 °C. For the outer surface of the coating, the elemental maps of Ni, Cr, and O are presented (Ref 149). Reprinted with permission from Elsevier

## Characterization of Exposed Coatings

Researchers have resorted to various methods to ascertain the performance of different coatings intended to impart protection against corrosion in varied environments. These have included weight change monitoring as well as the thickness of the corrosion scale, nature of the oxide scale, depletion of elements that are responsible for protective scale formation, etc. In addition, the formation of different complex corrosion products that occur during prolonged exposure of coatings to aggressive environments has also been of interest. Characterization tools help to better understand the nature of the corrosion products as part of the corrosion processes and the interaction between the corrosive agents and various alloying elements and their effect on scale growth. The techniques can be useful in assessing the effect of coating microstructure and composition in a given corrosive environment to study the corrosion mechanisms. Advanced methods can be used that are complementary to the simpler method of corrosion investigation involving weight change measurements.

### Weight Change Monitoring

The total weight gained after an oxidation test is simply a net result of the oxygen uptake due to scaling. When an external oxide layer is formed on the surface, the measured total weight gain essentially corresponds to the growth of the oxide layer (due to oxygen uptake). If the weight change results over time follow a trend (linear, parabolic, or logarithmic), they can be used to predict the corrosion rate over a longer period. However, the interpretation of the weight change results is not always simple and straightforward, especially for samples exposed to complex

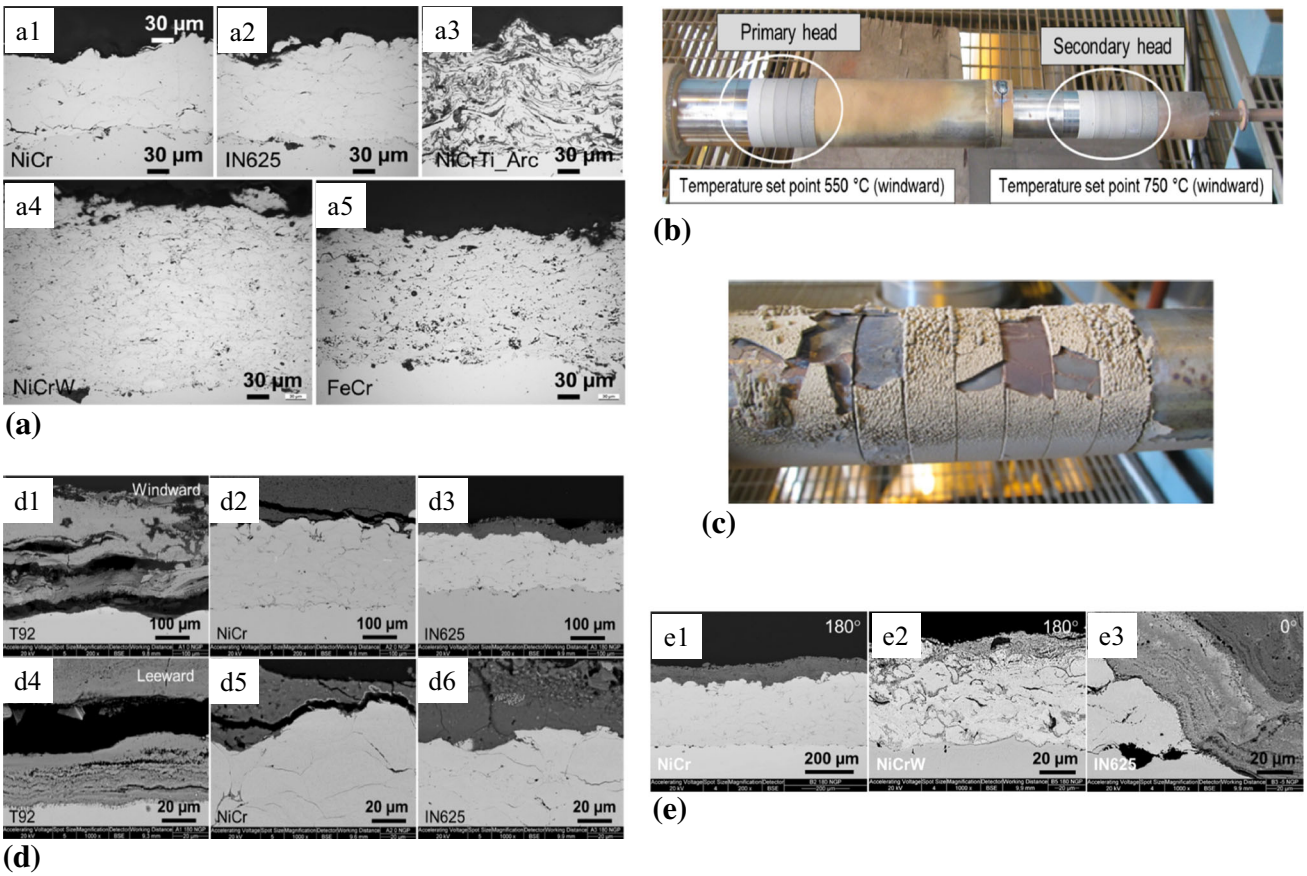


**Fig. 31** (a) Optical micrographs of thermal spray coatings before testing: (a1) HVOF-sprayed NiCr and (a2) Alloy 625, (a3) arc-sprayed NiCrTi, (a4) HVOF-sprayed NiCrW and (a5) FeCr; (b) the high-temperature probe used for the corrosion testing at two different temperature regions; (c) the probe after 1300 h of exposure, and the material samples at the metal temperature of approximately 550 °C; (d) SEM (BSE) images of the cross sections of the specimens after the 1300-h exposure at 550 °C: (d1-d3) windward sides of T92, NiCr, and Alloy 625 coatings, (d4-d6) the leeward sides of these coatings; and (f) SEM (BSE) images of the HVOF Ni-based coatings after exposure at 750 °C for 1300 h. The Cr content of the coatings varied between (e1) NiCr, with 46 wt.% Cr in a layer deposited on top of the coating, and (e2, e3) NiCrW and Alloy 625, with 21 wt.% Cr (Ref 150). Reprinted with permission from Elsevier

environments such as oxidizing–chloridizing environments. It is pertinent to mention here that the weight changes observed in the coated samples can be attributed to different factors:

(a) Formation of oxides, such as $Cr_2O_3$ or $NiCr_2O_4$ (Ref 87);
(b) Formation of metallic chlorides, mainly $NiCl_2$, $MoCl_3$, $CrCl_3$, or $CrCl_2$, within the coating (Ref 19);
(c) Evaporation of metallic chlorides, e.g., $NiCl_2$, $MoCl_3$, or/and $CrCl_2$, which can possibly form in Cl-containing environments (Ref 173);
(d) Spallation of the coatings and corrosion products (Ref 76);
(e) Deterioration of the substrate (16Mo3) by Cl and the formation of new phases (either oxides or chlorides) at the coating/substrate interface (Ref 88); and
(f) Sintering of KCl on the surface during exposure (Ref 90).

The problem of spallation is addressed by using an inert refractory crucible to collect the corrosion products formed. However, this experiment presents practical difficulties. Because spallation can cause violent ejection of oxide particles, the crucibles should be fitted with lids. Such an arrangement impedes the mass transfer between the specimen and the gas flowing past the crucible and is, therefore, not suited when using mixed gases. An alternative method for observing spallation directly is to use continuous thermogravimetric analysis (CTGA). In a CTGA experiment, a microbalance is used to record the weight changes occurring during the entire process, cycle after cycle. Thus, the oxidation kinetics are observed directly during the high-temperature periods, and the abrupt weight losses corresponding to scale spallation are, at least in principle, observable. TGA

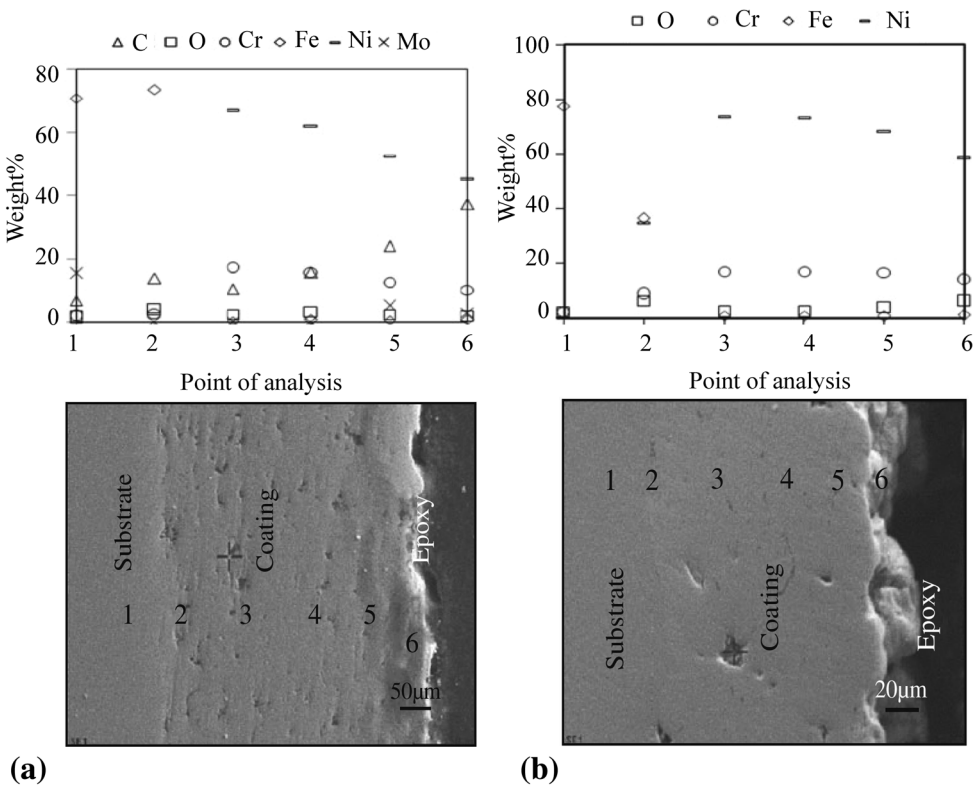


**Fig. 32** Variation in elemental composition across the cross sections of Ni-20Cr coatings on T22 steel: (a) HVOF coating and (b) cold-sprayed coating (Ref 151). Reprinted with permission from Elsevier

has been extensively used to study the high-temperature corrosion performances of thermal spray coatings in boiler applications (Ref 61, 62, 174-177).

Once a weight gain is recorded, it most probably implies that the factors leading to the gain (such as the formation of an oxide) outweigh the factors leading to a weight loss (such as vaporization), and vice versa. Moreover, weight change studies do not provide information regarding the internal corrosion, depletion of alloying elements, and formation of vacancies/voids within the scale. While still challenging, measurement of the oxide scale thickness is recommended to obtain separate information on the thickness of the deposit and the oxide layer, and the internal corrosion. Jafari and Sadeghimeresht et al. (Ref 57) measured the weight gain and thickness of the corrosion products for four HVAF-sprayed coatings Ni21Cr, Ni5Al, Ni21Cr7Al1Y, and Ni21Cr9Mo that were exposed to a KCl deposit in ambient air at 600 °C for up to 168 h. It was shown that, in most cases, the corrosion layer thickness was in good accordance with the observed mass gain. It was reported that internal corrosion and spallation were not considered in the calculations.

In general, the weight change measurement technique is economical and has become popular as a way of generating comparative alloy performance data under more realistic exposure conditions. However, it is necessary to use a combination of this measurement with more advanced analytical tools to overcome the difficulties.

## Microstructure and Compositional Analysis of Exposed Coatings

Figure 33 compares the capabilities and features of several analytical tools that can provide information about the high-temperature corrosion of coatings, e.g., identifying the microstructure and chemistry of the corroding surface. While some are site-specific (e.g., SEM/EDX, transmission electron microscopy (TEM), Auger electron spectroscopy (AES), and focused ion beam (FIB)), others can provide more general information pertaining to the surfaces (e.g., Fourier-transform infrared (FTIR), x-ray photoelectron spectroscopy (XPS), and BIB). While some offer useful information on the outermost layer, i.e., the surface film of a material (e.g., AES, time-of-flight secondary ion mass spectrometry (ToF–SIMS), and FIB/TEM), others reveal details from areas that are deep inside the specimen (e.g., SEM, Bragg–Brentano (BB)-x-ray diffraction (XRD), and computed x-ray tomography (CT)). Finally, while some techniques are beneficial for characterizing the distributions of major elements such as Ni, Cr, and Al (e.g., SEM/EDX, and XRD), others provide information regarding trace elements (e.g., ToF–SIMS and FIB/TEM/EDX).

It may be noted that some of the characterization techniques listed above can be employed both ex situ and in situ (e.g., XRD, FTIR spectroscopy, and environmental SEM (ESEM)). In situ analysis implies investigation of corrosion in real time and at the exact location where it

**Table 6** A summary of high-temperature corrosion studies on a few thermal spray coatings in environments simulating biomass-fired boiler conditions

| Year | Substrate material | Coating composition | Coating technique | Corrosive environment | Brief detail | Reference |
|---|---|---|---|---|---|---|
| 1997 | T2 | Ni45Cr (in wt.%) | HVOF wire arc | 400 ppm $H_2S$-100 ppm HCl-900 ppm $SO_2$ at 425 °C for 1000 h with and without a chloride-bearing ash deposit | The corrosion resistance of the coatings was limited by their inherited coating features like pores, which allowed local penetration of sulfur to the substrate surfaces. The HVOF process produced a denser coating than the arc spray and thus provided better corrosion resistance | 153 |
| 2002 | Ferritic steel (in wt.%; 2.25 Cr-1 Mo) | Ni-49Cr2Si<br>Ni-57CrMoSiB<br>Ni-21Cr9MoFe<br>Fe-15Al-2Cr<br>Ni-50Cr | HVOF, Excalibur HVOF, laser-treated coatings | 500 ppm HCl-600 ppm $H_2S$-5%CO-20% $H_2O$ (vol.%)-Ar, at 550 °C for 100, 400 and 1000 h | Despite the high alloy content in the coatings, the substrates were attacked by Cl and S. The corrosive species penetrated the coating through interconnected network of voids and oxides at splat boundaries. Laser melting improved the corrosion resistance of the coatings | 154 |
| 2003 | Ferritic steel (in wt.%; 2.25 Cr-1 Mo) | Ni-49Cr2Si<br>Ni-57CrMoSiB<br>Ni-21Cr9MoFe<br>Fe-15Al-2Cr<br>Ni-50Cr | HVOF, Excalibur HVOF, laser-treated coatings | 500 vppm HCl-3% $O_2$-14% $CO_2$-20% $H_2O$ (vol.%)-Ar at 550 °C for 100, 400 and 1000 h | Cr was the most beneficial alloying element of coatings | 84 |
| 2004 | Fe37 | Ni45Cr and 20NiCr-80$Cr_3C_2$ | HVOF with and without sealant, with and without laser treatment | Ambient air with and without a molten alkali chloride–alkali sulfate salt mixture of eutectic composition at 520-530 °C | Both the sealant and laser treatment reduced the corrosion rate of the coatings. The laser treatment parameters need modifications to attain a distinct melted and resolidified layer to improve corrosion resistance | 156 |
| 2005 | A mild steel | SHS7170 (20-25 Cr, Mo < 10, W < 10, B < 10, C < 5, Si < 5, Mn < 5, and balance Fe) | Wire arc | Ambient air environment 10 cycles (each cycle; 10 min at 600 °C) then exposed to erosive environment at 300, 450, and 600 °C using a bed ash from a boiler | The coatings provided protection as long as they remained bonded to the substrate | 157 |

**Table 6** continued

| Year | Substrate material | Coating composition | Coating technique | Corrosive environment | Brief detail | Reference |
|---|---|---|---|---|---|---|
| 2005 | AISI 304 austenitic stainless steel | Ni9Cr7Al6Mo, Ni48Cr | APS with and without laser treatment | A 210 kW laboratory combustion unit, using methane as fuel (10.5-11.6 vol.% $CO_2$, 50-200 ppm CO, and 3-3.5 vol.% $O_2$-balanced $N_2$) at 500 and 800 °C for 24 h | The laser treatment improved the coating–substrate bonding. The corrosion rate was significantly reduced by the surface treatment. At 500 °C, the oxidation was not obvious | 145 |
| 2005 | 9Cr-1Mo ferritic steel | Ni50Cr undercoat with an Al topcoat | APS | Steam oxidation at 600, 650, 700 and 750 °C for 100, 1000, 3000 h | The bi-layer coating architecture changed to a three-layered structure after the exposure<br>The undercoat was intact except the increased oxide formation at the inner splat boundaries | 75 |
| 2007 | SA213 T11<br>SA213 T22<br>SA213TP 347H | Fe17Cr5Al0.1Y<br>Ni50Cr<br>Ni43Cr1Ti0.1Fe<br>Cr16Ni9C1Fe<br>$80Cr_3C_2$-20NiCr | Arc spray<br>Flame spray<br>APS<br>Plasma spraying (vacuum)<br>HVOF | Ambient air<br>With and without<br>70%$V_2O5$-20%$Na_2SO_4$-10% NaCl<br>at 550 and 650 °C for 192 h (6 cycles) | The coatings were attacked through splat boundaries. Fe17Cr5Al0.1Y and Ni50Cr were prone to spalling. $80Cr_3C_2$-20NiCr coating remained mostly intact | 158 |
| 2008 | AISI 316L stainless steel | Ni15Cr3B5Si5Fe (in two particle sizes) | HVOF, LS-HVOF | Oxidation (ambient air at 800 °C for up to 500 h)<br>Hot corrosion (ambient air at 800 °C with $Na_2SO_4$ + 20 wt.%NaCl) | LS-HVOF NiCrBSi coating had superior corrosion performance in comparison with its HVOF counterpart, since a nanograined microstructure was produced in the former coating with high percentage of melted splats, low defects, and good uniformity | 159 |
| 2009 | Mild steel | $80Cr_3C_2$-20NiCr (coarse and fine particle sizes) | HVAF | At 650 °C for up to 200 h in ambient air | No carbide decarburization occurred during the HVAF spraying. The coating sprayed with the fine particle size (nanostructured) showed much better corrosion performance as the coating possessed a very compact and uniform microstructure | 160 |
| 2010 | Mild steel | Ni22Cr9Mo<br>Ni23Cr12Mo4Fe3W<br>Fe10Ni16Cr2Mo | HVOF | Electrochemical tests with a eutectic mixture of salts (in wt.%: 52%KCl-48%$ZnCl_2$), at 400 °C for 120, 240 and 360 h | The coatings showed high corrosion resistance (Ni22Cr9Mo was the best). Interconnected pores and spray oxidation were the main limitation in order to achieve a high corrosion performance | 161 |
| 2011 | | | | | | 162 |

**Table 6** continued

| Year | Substrate material | Coating composition | Coating technique | Corrosive environment | Brief detail | Reference |
|---|---|---|---|---|---|---|
| | SAE 213-T22 | Ni20Cr | HVOF | Boiler exposure (236 mg/m$^3$ $SO_x$-1004 mg/m$^3$ $NO_x$-15% $CO_2$-4%$O_2$) at 700 °C for 15 cycles (each cycle: 100-h exposure followed by 1-h cooling in ambient air) | The coating showed no spallation of its oxide scale. The coating retained its surface contact with the substrate without any signs of spallation | |
| 2012 | | | | | | 151 |
| | SAE 213-T22 | Ni20Cr | HVOF, cold spray | Boiler exposure (236 mg/m$^3$ $SO_x$-1004 mg/m$^3$ $NO_x$-12% $CO_2$-7%$O_2$) at 700 °C for 15 cycles (each cycle: 100-h exposure followed by 1-h cooling in ambient air) | The HVOF-sprayed Ni-20Cr coating performed better than its cold-sprayed counterpart, attributed to the continuous presence of protective $Cr_2O_3$ layer in the former case | |
| 2013 | | | | | | 85 |
| | P91 steel | NiCrBSiFe, alloy 718 (21% Cr), alloy 625 (19% Cr), C-276 (16% Cr) | HVOF | A gas mixture containing $O_2$, $N_2$, $H_2O$, HCl with and without KCl-45%$K_2SO_4$ for 168 h at 525, 625, and 725 °C | The effect of coating composition was highlighted. At 725 °C, the high Cr-containing coatings (Alloy 718 and Alloy 625) outperform the C-276 coating with lower Cr content. At 525 °C (below the salts eutectic point), C-276 coating was the best coating as the corrosion mechanism changed from that of molten-salt corrosion to that of gaseous corrosion | |
| 2013 | | | | | | 59 |
| | ASTM A213 TP347H | Ni20Cr<br>Ni50Cr | HVOF | Ambient air containing $Na_2SO_4$-60%$V_2O_5$ for 50 cycles (each cycle: 1-h heating at 700 °C followed by 1-h cooling in ambient air) | While the surface roughness and the content of porosity were lower in the Ni20Cr coating, the Ni50Cr showed a better corrosion performance implying the importance of the coating composition | |
| 2013 | | | | | | 76 |
| | X20 (Fe12Cr5Ni1Mo) | Ni46Cr<br>Ni22Cr9Mo4Nb3Fe<br>Ni21Cr10W9Mo<br>Fe25Cr15W12Nb6Mo4C | HVOF (carbide jet spray-CJS and hybrid diamond jet-DJ hybrid) | Synthetic air + 10% $H_2O$ with and without salt (6.5%NaCl + 59%$Na_2SO_4$ + 34.5%KCl) at 575 and 625 °C for 168 h | Chromia has high solubility in NaCl-KCl melt, but still a sufficient amount of Cr (> 18 wt.%) to form a protective $Cr_2O_3$ was needed for better corrosion resistance. The optimization of the coating structure besides selection of suitable chemical composition is critical | |

**Table 6** continued

| Year | Substrate material | Coating composition | Coating technique | Corrosive environment | Brief detail | Reference |
|---|---|---|---|---|---|---|
| 2014 | St35.8<br>Carbon steel (Fe0.1C) | Ni24Cr16Mo<br>Ni22Cr9Mo4Nb3Fe<br>Ni21Cr10Al1Y | HVOF | Field boiler exposure 40 MW, varied temperatures from 200 to 800 °C for 2 years | The coatings showed excellent corrosion resistance in the biomass boiler conditions during the two-year exposure. Corrosion attacks mainly occurred through oxidized lamellar boundaries and pores in the coatings | 133 |
| 2014 | St35.8<br>Carbon steel (Fe0.1C) | Fe27Cr11Ni4Mo<br>Fe19Cr9W7Nb4Mo | HVOF | Field boiler exposure 40 MW, varied temperatures from 200 to 800 °C for 2 years | Fe27Cr11Ni4Mo had an excellent corrosion resistance. Fe19Cr9W7Nb4Mo showed sufficient corrosion resistance in the boiler conditions, but due to perpendicular cracks the coating did not protect the substrate material | 55 |
| 2015 | X10Cr13 steel | Ni46Cr<br>Ni21Cr9Mo4Nb3Fe<br>Fe19Cr9W7Nb4Mo<br>Ni46Cr1Ti | HVOF | Actual boiler exposure (550 MW) in the superheater area after the cyclones for 5900 h, with varied temperatures from 550 to 750 °C | Altering the process parameters led to a significant improvement in corrosion resistance. Formation of a thin protective $Cr_2O_3$ layer resulted in a higher corrosion resistance | 166 |
| 2015 | Steel | Ni46Cr1Fe<br>Ni21Cr9W9Mo4Cu<br>Ni43Cr<br>Fe19Cr9W7Nb4Mo2C<br>Fe30Cr<br>Fe13Cr | HVOF wire arc | Ambient air +10% $H_2O$ with and without salt ($50\%Na_2SO_4 + 50\%KCl$) at 500 and 600 °C for 168 h | Both the coating composition and thermal spray process are important to achieve high corrosion resistance. The chromia-forming coatings were successful to control corrosion. At 600 °C, the coatings suffered from heavy depletion of Cr | 68 |
| 2016 | AISI 304L stainless steel | NiCoCrAlY (Ni23Co20Cr9Al1Y) | HVAF | Ar-10%$H_2$-20%$H_2O$ at 600 °C for 168 h | While the chromia-forming 304L was unable to tolerate the exposure condition, the alumina-forming NiCoCrAlY was able to form a protective $Al_2O_3$ layer that acted as a diffusion barrier which blocked the diffusion of the corrosive species | 97 |
| 2017 | AISI 304L stainless steel | Ni, Ni21Cr | HVAF | Ar-10%$H_2$-20%$H_2O$ at 600 °C for 168 h | Ni and NiCr coatings performed well due to being intact in the former coating and the formation of a continuous oxide scale of chromia in the later, which provided a barrier for further diffusion of corrosive gaseous species | 98 |

**Table 6** continued

| Year | Substrate material | Coating composition | Coating technique | Corrosive environment | Brief detail | Reference |
|---|---|---|---|---|---|---|
| 2018 | P92, T22 (Vallourec) and Sanicro 28 | Ni5Al, Fe50Cr, Ni20Cr | HVOF | 8%$O_2$-60%$CO_2$-30%$H_2O$-2% $N_2$-2 vppm $SO_2$-400 vppm HCl with and without a mixed salt of 45 wt.% KCl + 55 wt.% $K_2SO_4$ for up to 672 h at 550 °C | A sufficient in-flight oxidation during spraying was shown to be beneficial to reduce corrosion rate of the coatings. Cr-rich oxides formed around splats during spraying seem to block intersplat corrosion attack in the coatings | 67 |
| 2018 | AISI 304 stainless steels | Ni30Al | HVOF | 5 vol.% $O_2$ + 500 vppm HCl + $N_2$ at 700 °C for up to 250 h, with and without KCl salt | Severe corrosion was observed with the fast-growing alumina at the coating/substrate interface initiating from sample edges. The formation of volatile chlorine/chloride acted as a catalyst and promoted the growth of alumina | 8 |
| 2018 | ASME P92 | Ni50Cr | Cold spray, HVOGF HVOLF | 5 vol.% $O_2$ + 500 vppm HCl + $N_2$ at 700 °C for up to 250 h, with and without KCl salt | There was no continuous oxide scale when KCl was not present as a deposit, and the oxide scale deteriorated further due to the presence of KCl. These phenomena indicate the detrimental effect of chlorine on oxide scales | 170 |
| 2018 | Steel | $Cr_3C_2$-50NiCrMoNb | HVOF, HVAF | Ambient air + 10-12%$H_2O$ with and without KCl salt, for 72 h at 550 °C | At the early stages of corrosion, the actual metal binder composition is probably the corrosion rate-controlling factor. At the last stages, formation of a network of fine secondary carbides precipitates and their fast degradation is the rate-controlling factor | 62 |
| 2018 | 16Mo3 | Ni21Cr7Al1Y and a proprietary SiO2-containing Ni21Cr9Mo coating | HVAF | 5 vol.% $O_2$ + 500 vppm HCl + $N_2$ at 600 °C for up to 168 h, with and without KCl salt | Both coatings were protective in the absence of KCl due to formation of a dense Cr-rich oxide scale. In the presence of KCl, $Cl^-/Cl_2$ diffused through a non-protective and porous NiCr2O4 scale formed on NiCrAlY, leading to formation of volatile $CrCl_3$ | 87 |
| 2018 | 16Mo3 | Ni21Cr, Ni5Al | HVAF | 5 vol.% $O_2$ + 500 vppm HCl + $N_2$ at 600 °C for up to 168 h, with and without KCl salt | Both alumina- and chromia-forming coatings were protective in the absence of KCl. With KCl, the alumina-forming Ni5Al coating presented a much better corrosion behavior | 88 |

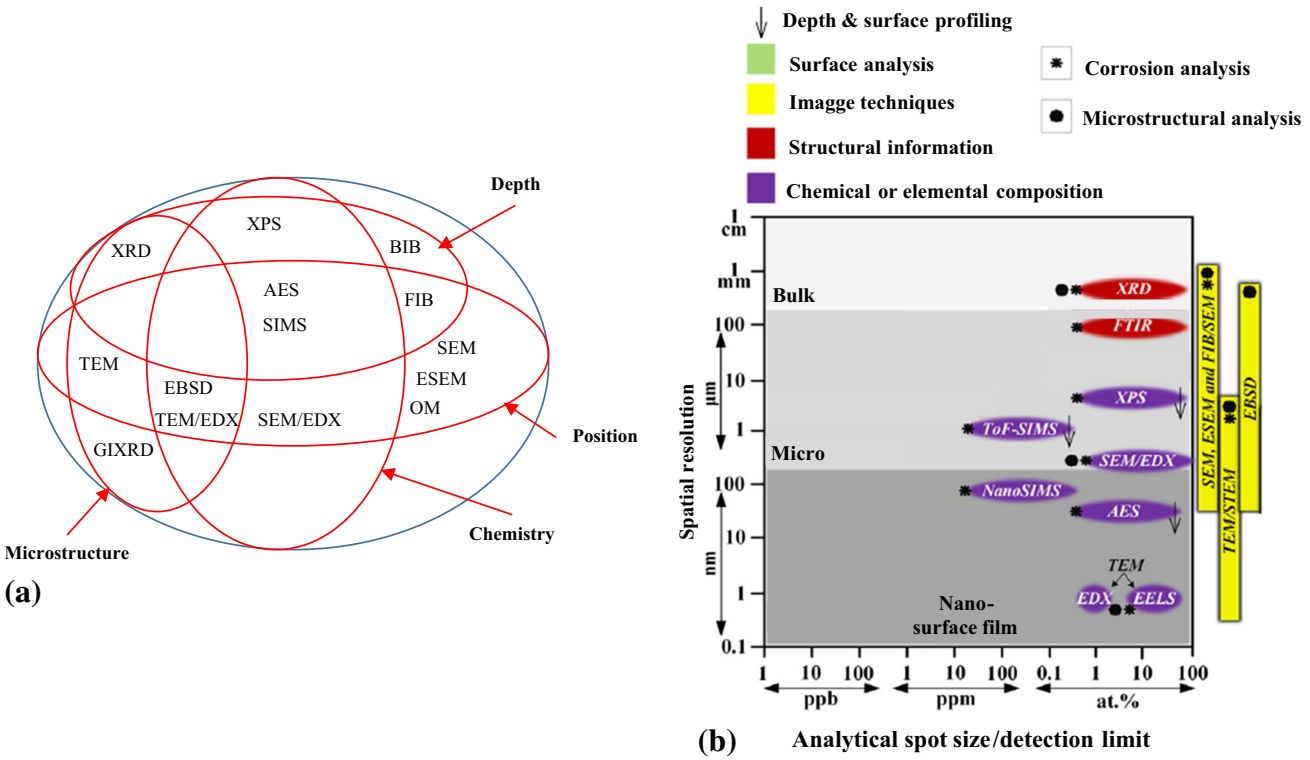


**Fig. 33** Comparison of different analytical tools. (a) An overview of the applications (structure/chemistry) and capabilities (depth/position) of the several analytical techniques that can be applied in Mg corrosion research, (b) detection limit versus spatial (lateral) resolution of the described methods, and (c) qualitative versus quantitative assessments of microstructure–corrosion relationships

occurs. The interest in in situ analysis as part of high-temperature coating research is currently increasing. This is because such investigations can be of great help in understanding of the dynamics of a corrosion process because corrosion-related changes can be observed as they occur, rather than after the conclusion of the experiment, as is usually the case (i.e., ex situ or post-analysis). Thus, in situ methods can be used to detect the formation of the initial corrosion products, which are converted into more stable compounds as the corrosion process proceeds. In addition, in situ methods allow observation of the corrosion process without disturbing it. To summarize, the functional difference between these methods stems from parameters such as the detection limit and spatial resolution (see Fig. 33), and also the nature of the information that each method can provide (Fig. 33). Note that not all the analytical tools that are used or have the potential to be used in the field are covered in this review.

## Ion Milling for Cross-Sectional Analysis

Plan-view SEM images and/or the data should be complemented by cross-sectional analysis. Cross sections can be produced either manually (through cutting, grinding, and polishing) or by using $Ga^+$ FIB milling or $Ar^+$ BIB milling (Ref 178). FIB milling tools, such as dual-beam FIB/SEM (Ref 179), are utilized in microstructural investigations, offering a combination of high-resolution imaging and flexible nano/micromachining capabilities that provide site-specific cross sections in the region of interest (5-200 μm width and 20-100 μm depth). The FIB technology has contributed significantly to the understanding of high-temperature corrosion-resistant coatings. Katranidis et al. (Ref 180) used plasma FIB-SEM to ion-mill and capture images from a volume of the coating, aiming to extract information and provide insights into the 3D structure of the coating and the pores. Pereira et al. (Ref 181) used a FIB to study the high-temperature oxidation behavior of laser cladding MCrAlY-coatings, whereas Song et al. (Ref 182) utilized a FIB to evaluate the growth mechanisms of thermally grown oxides on plasma-sprayed TBC. Sadeghimeresht et al. (Ref 97, 98) used the BIB technique to prepare wide cross sections of Ni, NiCr, and NiCoCrAlY coatings in the millimeter range.

It may be noted that FIB-prepared cross sections reveal much lower amounts of artifacts than manually prepared cross sections. Furthermore, the cross sections prepared by using FIBs through, e.g., the lift-out procedure, are in the form of smooth and damage-free thin foils, making it possible to examine the chemistry/composition of the corrosion products at a very high resolution. A BIB produces wide (1.5 mm width and several hundred microns

deep) and accurate cross sections of the corrosion products and the metal substrate with minimal amounts of artifacts, compared to mechanical grinding/polishing (Ref 179). Considering the large surface areas of the BIB-prepared cross sections, the method can in principle replace mechanical cross-sectioning, as it is very well suited for the study of localized corrosion in heavily corroded samples or when statistical treatment of the data is crucial.

There are, however, several parameters that affect the final polishing result, such as gun angle, milling voltage, milling time, modulation, and temperature. Besides, each sample, depending on the chemical composition and the existing phases, behaves differently when exposed to an ion beam. In this regard, selective etching limits the application of this method to some extent. Ion bombardment is quite a rough technique for materials (especially those that are at least as metallic as Fe). It can be implemented on surfaces near lattice defects, which especially affect surface-sensitive techniques like EBSD.

### Electron Backscatter Diffraction (EBSD)

EBSD is a SEM-based technique that provides information on crystallographic orientation/texture and grain size and can be used in the identification of phases, with the typical spatial resolution being approximately 20 nm (Ref 183). It can elucidate the relation between the microstructure and the corrosion behavior of coatings and has resulted in significant advances in the field. The EBSD method has been used to understand some crucial corrosion-related metallurgical aspects such as (dynamic and static) recovery and recrystallization, crystallographic texture, and the anisotropy caused by a strong texture. It can also be used to study oxide scale structures (Ref 184).

Mori et al. (Ref 185) used the EBSD technique for distinguishing $\beta$-grains, with BCC structure, more clearly from the $\gamma$-matrix, having FCC structure, of CoNiCrAlY coatings fabricated through warm spraying and HVOF processes. Tian et al. (Ref 186) used EBSD to examine the crystallographic relationship at the APS-deposited NiCr-Mo coating/substrate interface. It was shown that the grains of the first splat layer grew across the substrate grew epitaxially across the substrate, depending on the substrate material. This indicates that the Ni20Cr-20Mo splat crystallized hetero-epitaxially relative to the substrate. As a result, strong coating–substrate bonding with great adhesion was achieved. Manap et al. (Ref 187) studied the protectiveness of a TGO layer on cold-sprayed (CS) and low vacuum plasma-sprayed (LPPS) CoNiCrAlY coatings. EBSD was used to image the grain orientations of the CS and LPPS coatings after a short period of oxidation, as well as to image their microstructural evolution over a long period of oxidation; see Fig. 34. The grains in the CS coating became much coarser after the oxidation test, compared to those of the LPPS coating. The grain boundary energy and the stored deformation energy, as a result of severe plastic deformation and the grain refinement occurring during the CS deposition process, may be responsible for the larger grains observed in the CS bond coat during the oxidation process.

In summary, the EBSD technique has been used for phase recognition, grain-size analyses, and texture determination in thermal spray coatings. No study was performed to correlate the grain structure of a coating and its oxide scale. An alternative method of revealing the oxide grain size and shape is the FIB method.

### X-ray Diffractometry (XRD)

XRD has been widely employed for high-temperature corrosion-resistant coatings (Ref 188-191). XRD is very powerful for identifying crystalline compounds in, e.g., corrosion products. XRD can also easily distinguish between corrosion products having similar or identical chemical compositions. It can also be used for analyzing corrosion product mixtures.

Sadeghimeresht et al. (Ref 88) showed that the HVAF process did not affect the phase compositions of the feedstock powders, based on XRD analysis. The formation of a few in situ oxides could likely be due to (a) the powder particles being exposed to high temperatures in an oxidizing ambient air environment during the spraying process (Ref 192, 193) and/or (b) the oxygen pre-existing in the feedstock material (Ref 193). The influence of the former was minimal in the investigated samples, as the dwell time in the HVAF process was small and the temperature also very low (Ref 112). It was also shown that polished HVAF-sprayed coatings retained the solid-solution phase of the feedstock powders. The XRD patterns of the as-sprayed Ni-based coatings showed that the Ni peaks shifted toward shorter lattice parameters (i.e., higher $2\theta$ angles), which might be due to the residual stresses present in the coatings (macrostrain) (Ref 174). Peak broadening of the HVAF-sprayed coatings is observed relative to the powders, and can be due to three primary factors: (a) the presence of a microstrain due to the plastic deformation occurring during the HVAF spraying process (Ref 113), (b) reduction in crystallite size, and (c) instrumental broadening, which is a function of beam size, sample to detector distance, air scattering, etc. (Ref 195). While the level of microstrain can be studied through a line profile analysis, numerous methods have been developed to quantify the crystal size and residual strain, which is not within the scope of this study.

There are a few challenges with XRD measurements. First is the x-ray penetration depth into the material. In

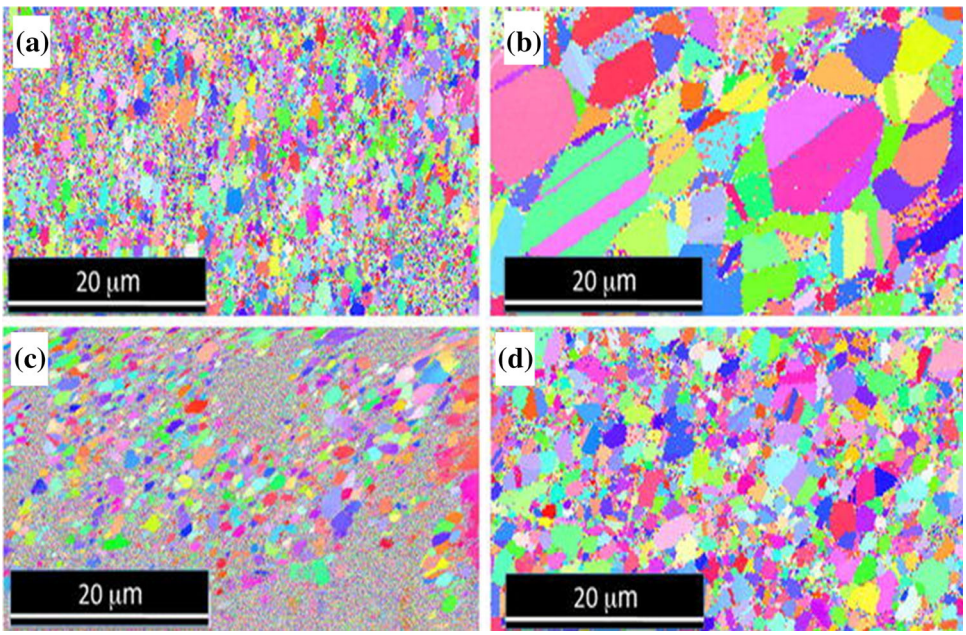


**Fig. 34** EBSD maps of the cross sections of the bond coats of (a, b) CS and (c, d) LPPS specimens after (a, c) 1 h and (b, d) 800 h of oxidation (Ref 187). Reprinted with permission from Elsevier

particular, for the coatings exposed to KCl salt, the thickness of the corrosion product plus the deposit is almost greater than 10 μm, which is much above the identification limit of XRD. The second challenge is the inability of the XRD technique to provide information on the samples exposed to alkali chlorides, wherein volatile metallic chlorides can form. It is pertinent to mention that, before the XRD measurement, a calibration sample such as $LaB_6$ must be used to avoid peak broadening, due to instrumental parameters such as collimator size, detector resolution, and beam divergence.

### Three-Dimensional (3D)-Imaging/EDX/EBSD

The interplay between the corrosion media and the coating at high temperatures often produces a complex corrosion product, with the surface of the metal remaining being strongly convoluted, sometimes exhibiting localized corrosion pits that penetrate deep into the substrate. To investigate and characterize this type of corrosion attack, it is highly desirable to complement the "conventional" 2D techniques with 3D methods. Advanced SEM/FIB microscopes (dual-beam systems) equipped with EDX and EBSD detectors have been utilized to perform 3D microstructural studies on thermal spray coatings (Ref 184). Three-dimensional imaging, e.g., by using microtomography, has been developed to relate pore and crack interconnections, which is difficult through the 2D methods (Ref 196). The 3D approach allows the determination of the thermomechanical and electrical properties, primarily Young's Modulus, which can be compared to those obtained from the 2D approach. Three-dimensional imaging has also been used for failure analysis and deformation of TBCs through CT (Ref 197). However, very few papers deal with high-temperature corrosion of thermal spray coatings. The systematic use of 3D imaging to investigate the complex relation between an alloy microstructure and the corrosion is still in its infancy. However, 3D methods have great potential in corrosion research, especially for high-temperature thermal spray coatings.

### X-ray Photoelectron Spectroscopy (XPS)

In thermal spray coatings, the influence of protective-layer-forming elements such as Cr and Al can be studied by XPS, as this technique is a highly surface-sensitive research tool for corrosion science. It provides unambiguous information on the chemistry and the detailed mechanism of the corrosion process that occurs on the surface.

Viswanathan et al. (Ref 198) investigated the behavior of a solution precursor plasma-sprayed nanoceria coating in atmospheric air subjected to cyclic oxidation at 1000 °C by using XPS to obtain quantitative information on both the elemental and chemical states. XPS shows that the presence of $Ce^{3+}$ creates $O^{2-}$ vacancies that induce more inward diffusion of oxygen compared to its competing mechanism of outward diffusion of elements such as Cr and Fe that are present in the substrate. Such diffusion will help in avoiding void formation and will lead to a more adherent scale, as observed in the oxidation kinetics that shall be discussed later. XPS also showed the beneficial effect of Ce addition in high-temperature thermal spray

coatings as part of a more recent study by Singh et al. (Ref 199).

### Auger Electron Spectroscopy (AES)

Like XPS, AES is an analytical technique used to study the chemical composition of thin surface layers on metals/coatings. However, AES is inherently more useful than XPS in corrosion studies because of its higher lateral resolution. While both AES and XPS are electron spectroscopy methods, AES uses electrons as the excitation radiation instead of x-rays. Moreover, while the photoelectrons emitted in XPS are core electrons, Auger electrons are ejected as a result of de-excitation of an ionized atom to its ground state (Ref 200). With a lateral resolution in the range 10-100 nm, AES is very suitable for high-resolution surface chemistry analysis, which is often required in corrosion studies. Still, AES exhibits depth resolution (a few nanometers) and sensitivity (0.1 at.%) that are similar to those of XPS. Similar to XPS, AES is often combined with ion sputtering to obtain depth profiles. Porcayo-Calderón et al. (Ref 132) studied the electrochemical behavior of HVOF-sprayed Ni20Cr coatings in $ZnCl_2$-KCl at high temperatures and proposed the use of complementary techniques, e.g., SEM and AES, among others, to clarify both the morphology after the attack and the chemical composition and distribution of the elements present. A combination of these methods provides the information required to understand the reactions occurring on a surface. With high-resolution Auger spectroscopy, it is possible to detect the elements present on a surface. Moreover, it is possible to track the differences in the chemical state of the elements found in different locations on a surface.

### Secondary Ion Mass Spectrometry (SIMS)

SIMS features a unique combination of extremely high sensitivity for all the elements from hydrogen to uranium, high lateral resolution imaging ($\sim$ 40 nm), and very low background, which permits a high dynamic range ($>$ 5 decades) (Ref 201). One important drawback is that the compositional information obtained is not quantitative. ToF–SIMS (time-of-flight secondary ion mass spectrometry) is a high-vacuum technique that focuses a pulsed beam of ions (often Cs or Ga) onto a specimen surface, thus creating secondary ions through a sputtering process. The ions generated from the sample surface are then accelerated into a "flight tube," and their mass is calculated by measuring the time taken to reach the detector (time-of-flight) (Ref 202). It provides the oxide composition, and the $^{16}O/^{18}O$ sequential oxidation can be used to evaluate the oxide growth mechanisms. The analysis of a single compound in SIMS generates an assortment of atomic and molecular ions that is characteristic of that compound. Hence, SIMS inherently can provide chemical information of a surface (Ref 203, 204). The analyzed surface is abraded during SIMS analysis and by increasing the ion current, the technique can provide depth profiles. Despite its several attractive capabilities, ToF–SIMS has been little used for high-temperature corrosion resistance coatings.

Wu et al. (Ref 204) studied the distributions of the elements in HVAF-sprayed Fe-based amorphous coatings that were characterized by SIMS. The localized Cr depletion of the coating was analyzed by SIMS to reveal that the depletion was caused by the defects in the coatings, e.g., pores, oxides, and crystalline phases, which are thought to be the dominant reason for the decrease in the corrosion resistance of the coatings.

### Transmission Electron Microscopy (TEM)

While the spatial resolutions of AES, XPS, and SIMS continue to improve, atomic scale analysis can only be performed by using TEM combined with EDX or electron energy loss spectroscopy (EELS). TEM is used to characterize the microstructure and the chemistry of materials at the nanoscale. In TEM, a fast-moving electron, of wavelength much less than 1 Å, is transmitted through a thin sample (Ref 205). TEM has a far better resolution than conventional SEM imaging and is extremely useful for determining the crystal structure, crystallographic orientation, and chemical composition of microstructural features and corrosion layers. The TEM analysis of FIB-prepared thin foils allows researchers to investigate a surface film locally and with a minimum amount of artifacts. Owing to its capabilities and increased availability, the use of TEM in high-temperature corrosion-resistant coatings has grown rapidly. Poza et al. (Ref 206) used TEM to investigate the fine microstructural evolution of TGO during isothermal oxidation to explain the macroscopic oxidation behavior. The Al-rich oxides present within the bond coat were disclosed by TEM, as polycrystalline areas were formed by the small $\alpha$-$Al_2O_3$ crystals. Zou et al. (Ref 207) utilized TEM to study the phase constituents and the microstructure of an HVAF-sprayed nanostructured NiCrCoAlY-$TiB_2$ coating exposed to high temperatures, ranging from 600 to 1000 °C.

### Fourier-Transform Infrared (FTIR) Spectroscopy

In IR spectroscopy, IR radiation is passed through a sample and the absorption spectrum is recorded. Its interaction with a vibrating molecule or solid causes certain wavelengths of the radiation to be absorbed. For absorption, the vibration must experience a change in its dipole moment.

In corrosion research, FTIR spectroscopy is often used in the specular reflectance mode or diffuse reflectance mode. FTIR is very surface sensitive, being able to detect much less than a monolayer of a compound on a surface. Importantly, the measurements are performed under ambient conditions, suggesting that it is ideal for, e.g., in situ atmospheric corrosion experiments (Ref 208). IR spectra can be recorded from surfaces with a lateral resolution, which depends on the wavelength, which is of the order of 10 μm (FTIR microscopy). FTIR is a valuable complementary technique that allows the detection of small amounts of corrosion products that are liable to decompose in vacuum or upon exposure, e.g., to an electron beam. Aguero et al. (Ref 67) performed a screening laboratory test to investigate the biomass corrosion behavior of HVOF-sprayed Ni-based coatings in contact with KCl/$K_2SO_4$ at 550 °C under an oxy-fuel combustion atmosphere by using FTIR.

### Raman Spectroscopy

Raman spectroscopy is a technique that can fingerprint molecules by sensing the vibrational modes of molecular bonds (Ref 209). As such, Raman spectroscopy is an appropriate technique to study metal surfaces and, in particular, coating layers and corrosion products. It has been used for decades as a nondestructive technique for determining the stresses developed in oxide scales based on the shifts in the bands of the Raman spectra of specimens with pressure (Ref 210). The salient features of this technique are: (1) It does not require a special environment, and (2) it offers a high resolution. An important advantage of Raman spectroscopy is that it is a nondestructive technique that allows for in situ identification of corrosion products. Lee et al. (Ref 211) used Raman spectroscopy for the evaluation of the phases present in a passive film formed on Al coating that was produced by arc thermal metal spraying. Subanovic et al. (Ref 212) investigated the effect of manufacturing-related parameters on the oxidation properties of MCrAlYHf bond coats. Raman spectroscopy was applied to identify the oxides formed on the surface of the heat-treated specimen. The oxide formed on the surface was mainly yttria, but hafnia and occasionally some yttrium aluminates could also be observed. Ding et al. (Ref 213) suggested that the limit of detection of the XRD method employed is typically 1-2 wt.%. Therefore, very small quantities of corrosion products cannot be identified. It was proposed that more surface-sensitive techniques, such as Raman spectroscopy, are needed to clarify whether small amounts of corrosion products can form. Chen et al. (Ref 214) investigated the chemo-mechanical coupling oxidation behavior of CoNiCrAlY coating, which is widely used as the bond coat in TBC systems. Oxidation experiments were performed at 1000 °C on both load-free and tension-loaded specimens. Microscopic examination was also performed by using SEM and Raman spectroscopy. In the oxide scale of the load-free specimen, both α-alumina and θ-alumina were present when the duration of oxidation was short ($\leq$ 15 h), and the θ-alumina transformed to α-alumina after 20 h of oxidation. By contrast, in the tension-loaded specimen, mixed α-alumina and θ-alumina were found even after oxidation for 20-60 h. This phenomenon suggests that the tensile load can delay the phase transformation of the fast-growing θ-alumina to the slow-growing α-alumina. Gil et al. (Ref 215) used Raman spectroscopy to study the compound type, distribution, and morphology of the Y-rich oxide particles in MCrAlY-coatings during various stages of manufacturing and oxidation exposure. Phase analysis of the Y-rich oxide compounds, based on the wavelength-resolved Raman spectra, is possible. The results of Raman spectroscopy studies indicate that the type of the Y-rich oxide phases present after heat treatment can be correlated with the content and/or the reservoir of metallic Y observed in the coating. The distribution of the Y-rich oxide precipitates formed during manufacturing has been shown to affect the growth rate and the mechanical stability of the alumina scales during service. The Y oxide distribution in the MCrAlY-coatings, therefore, represents a factor that influences the lifetimes of overlay coatings and TBC. Zhu et al. (Ref 210) showed that Raman spectroscopy can be used to determine the stresses present in chromia scales formed at 900 and 1000 °C on NiCoCrAlY. The residual stresses within the chromia layer that were obtained (−1680 MPa by micro-Raman spectroscopy and −2060 MPa by XRD analysis) are in good agreement with the numerical modeling results ($\sim$ −1800 MPa) (Ref 216, 217).

### Environmental Scanning Electron Microscope (ESEM)

The ESEM provides almost the same sort of information as the SEM. Nevertheless, it offers several advantages over conventional SEMs. First, difficult specimens, including wet and insulating ones, can be investigated in an ESEM. The ESEM permits this by enabling a gaseous environment, e.g., water vapor, to be present in the instrument chamber while retaining its rather high resolution. Moreover, ESEM investigations can be carried out in a variety of conditions: (i) temperatures ranging from 30 to 1500 °C, (ii) pressures of up to 10 Torr or 6700 Pa, and (iii) up to 99% RH (Ref 218). These capabilities offer an exceptional

opportunity to view the dynamic processes occurring on material surfaces "live" and in a time-resolved manner. Viewing the initial stages of the interactions between the surfaces and their surrounding environmental contaminations, e.g., gaseous species and alkali salts, is one of the practical applications of in situ ESEM. In spite of these benefits, it is only lately that this technique has started to create an impact in corrosion science research.

Boudi et al. (Ref 219) studied the microstructure of the HVOF-sprayed Alloy 625 coating/substrate interface by using ESEM after performing tensile tests. The technique showed that the coating structure and composition are highly nonuniform at the microscopic scale. The microscopic chemical inhomogeneity observed in the coating is attributed to the presence of numerous dark inclusions and grain boundaries, which show segregations of Cr, Nb, and oxygen in the Ni-rich matrix.

### Electron Probe Microanalysis (EPMA)

EPMA works by bombarding a micro-volume of a sample with a focused electron beam (typical energy = 5-30 keV) and collecting the x-ray photons thus emitted by the various elemental species present in the specimen (Ref 220). Because the wavelengths of these x-rays are characteristic of the emitting species, the sample composition can be easily identified by recording the wavelength-dispersive spectroscopy (WDS) patterns. These spectrometers operate based on Bragg's law and use various moveable, shaped monocrystals as monochromators. EPMA is a fully qualitative and quantitative nondestructive method of elemental analysis of micron-sized volumes of the surfaces of materials, with a sensitivity of the order of parts per million. EPMA provides much better results than standard SEM/EDX systems. Because of the internal properties of WDS, the general sensitivity, the analysis of light elements, and the risk of an erroneous interpretation of the qualitative spectra are all superior in the case of EPMA compared to SEM/EDX. The spectral resolution and the detector dead time are much better than those of EDX. The excitation beam regulation system and the sophisticated sample stage capabilities guarantee that this technique provides outstanding stability and measurement repeatability.

EPMA has been used in many studies on high-temperature corrosion of thermal spray coatings (Ref 221-223) to analyze the corrosion products formed on the surface and the distribution of elements. EPMA can be performed on the cross sections of scales to reveal any changes in the microstructure and the chemistry of the coating and the underlying substrate upon oxidization in steam and air at elevated temperatures (Ref 224).

## Outlook

The present review mainly aims to understand the effect of coating microstructure, composition, and architecture on high-temperature corrosion behavior. There is still much work to be performed, both on the fundamental level to follow and understand specific reactions and mechanisms and in the more complex atmosphere of boilers in actual operation, where economic and environmental factors call for improved alloy performances.

### Understanding Corrosion Mechanisms

Despite the considerable work performed over the past 20 years, there has been no definitive experiment that accurately simulates the complex operating conditions prevailing in a real boiler. Many effects have been identified, but none can explain all of the aspects observed in the actual boiler exposures. Clarification of the observations has impacts on the design of new coatings and the corrosion behavior of coatings employed in engineering applications. Therefore, more work aimed at identifying the mechanism is warranted.

Owing to sintering of the salt, the exchange between the furnace atmosphere and the atmosphere under the deposit is limited, which retrospectively confirmed the presence of low $O_2$ partial pressures even above the corrosion products (Ref 225). Thus, the conditions at the scale interface between the deposit and the corrosion scale are completely different from those found at the deposit/fluent gas interface. The gas transport restrictions due to the reactions within the deposit are considered to strongly influence the corrosion involving Cl. Such findings are highly relevant for the testing of, e.g., alternative materials or new coatings to simulate the corrosion attack in the presence of WtE salts and ashes.

The permeability of oxide scales such as alumina or chromia to gaseous species such as CO, $SO_2$, HCl, or/and $H_2O$ is an important, but poorly understood phenomenon. The nature of the transporting species (ionic or molecular) has not been fully understood. For instance, the reasons for their slower penetration through alumina than chromia are not well understood. High-temperature adsorption experiments in mixed-gas atmospheres might contribute to an understanding of the complex interaction effects reported. It is generally agreed that alumina scales are much better barriers to secondary oxidants than chromia, but this observation is unexplained. An improved understanding of the detailed structures of the grain boundaries in the two oxides is required. It is likely that progress will result from both improved characterization and atomistic modeling.

The multiple ways in which water vapor interacts with oxides have made understanding of the overall situation elusive. The different behaviors of coatings in pure steam and air–steam mixtures have further complicated the set of observations. A part of the difficulty in arriving at an understanding is the sensitivity of the oxidation result in small differences in exposure conditions. A review (Ref 226) of a comparative testing exercise of P92 alloy samples exposed at 650 °C for 1000 h in different laboratories revealed variations in scale thickness of 40-240 nm. The additional changes observed were associated with the steam pressure, flow rate, diluent argon levels, and cooling procedures employed after the experiment. Similar constraints can be imposed during the evaluation of the thermal spray coatings.

More specifically, when chromia scales are formed, the presence of water vapor improves scale-alloy adhesion. In the case of alumina scales, spallation is promoted by the presence of water vapor (Ref 227). In addition, the presence of water vapor alters the rates at which transient alumina phases grow and are transformed, thereby modifying the oxidation rate (Ref 228). A systematic investigation of the interactive effects of water vapor and reactive element additions on the cyclic oxidation of different chromia and alumina formers is highly desirable.

## Novel Coating Compositions

Apart from already investigated materials such as Ni-based superalloys, intermetallics such as (Ti, Ni, Fe or Nb)$Al_3$, (Ti, Ni, Fe or Nb)Al, or (Ti, Ni, Fe or Nb)$_3$Al (Ref 75, 229-233) as well as high-entropy (HE) coatings such as CoCrFeNi, CoCrFeNiCu or CuNiSiTiZr, $Al_{2-}$ $CrFeNiCoCuTi_x$ (Ref 234-236) are the candidate materials when higher efficiency of the boiler at higher temperatures/pressures is of interest.

Intermetallics have been recently developed owing to their specific properties (Ref 237). For instance, aluminides are of particular interest because they have high melting points, low densities, and considerable resistance to high-temperature corrosive atmospheres. Their interesting properties make them important materials for aeronautical applications (Ref 238), and an attractive candidate for boiler applications. Most alloys and superalloys have to be used at temperatures lower than 0.4 $T_m$ ($T_m$ being the melting point in K) because of their creep capacities, whereas ceramics and intermetallics are capable of functioning at higher temperatures, although their cost and the difficulties due to their development can limit their use. The development of aluminides is based on the huge Al "reservoir" that they offer, compared to classical alumina-forming materials (typically Fe-20Cr-5Al). Indeed, when FeCrAl is subjected to long-term oxidation at high temperatures, the consumption of Al leads to its depletion in the underlying substrate (Ref 239). As a consequence, when the Al content decreases to a critical level, around 1.7 wt.% in FeCrAl alloys (Ref 240), no more protective alumina can grow. Cr and/or Fe oxide formation then becomes predominant and promotes significant degradation of the materials. Increasing the Al content has spectacular effects on the long-term high-temperature performance of the materials (Ref 241). So, the main reason why metal has been developed is their potential Al "reservoir" which guarantees the formation of protective alumina scales, even after long exposures at high temperatures or after repeated thermal cycling. However, adding more than 5% of Al in metals considerably decreases their mechanical properties, especially at ambient temperature. Most aluminides then become brittle, which is an issue during machining and shaping. This problem is reduced by the additions of minor elements (such as B, Zr, $Y_2O_3$, Cr, Ce, and Nb), which improve the room temperature mechanical properties (Ref 242). Two other solutions can be considered to improve the mechanical properties of aluminides: modification of their microstructures by using innovative processes such as combustion synthesis or self-heat-sustaining (SHS) (Ref 243), as well as application of the intermetallic compounds directly on a metal or alloy surface as diffusion coatings (Ref 244).

As a result of extensive research activity on intermetallics, there is currently a high level of freedom in controlling the microstructure, adjusting the alloying additions, and choosing the suitable surface treatment. This allows us to fabricate parts with the desired mechanical properties and sufficient resistance to environmental attack at the laboratory level. Tests under exact and specified application conditions are necessary for individual parts, which are under mechanical stresses and exposed to severe conditions of varying temperatures and gas compositions. These conditions would be very different from those of the laboratory tests, where the gas composition is usually constant, there is no mechanical loading, and the temperature change is regular even during cyclic oxidation. The oxidation temperatures observed in many studies have been a little higher than the practical values, even though data over a wide range of temperatures are needed for assessing the activation energy or performing a mechanistic study. In other words, there is a need for more practical experience and, by collecting, examining and/or dissecting the problems arising from practical usage, more efficient development of individual components or parts is possible. On the other hand, it can be said from a scientific viewpoint that data on fundamental parameters are lacking. For instance, the influence of additional elements on the diffusivity and activity of the relevant elements is poorly known. Phase equilibrium diagrams of tertiary and quaternary systems

are very few. These are indispensable for a theoretical understanding of the phase relations. The mechanism of the influence of combined addition of alloying elements is unclear, although the most suitable combination would represent an optimization of production cost, environmental protection, and high performance.

HE coatings are another set of materials that have not yet been fully explored. Compared with conventional alloys, high-entropy alloys are composed of five or more alloying elements whose concentrations are with a near equimolar ratio to the alloys. It was confirmed that high-entropy alloys possessed simple solid-solution structure rather than complex phases or intermetallic compounds due to the high mixing entropies and accompanied sluggish cooperative diffusion, which avoids the brittleness of compounds. Based on the contribution of above structural and compositional features, good properties such as strength, good thermal stability and oxidation were reported for high-entropy alloys (Ref 245). The oxidation performance of atmospheric plasma-sprayed $Ni_{0.2}Co_{0.6}Fe_{0.2}CrSi_{0.2}AlTi_{0.2}$ HE coating has been investigated (Ref 246). It was revealed that the initial weight gain of the HE coating at 1100 °C was higher than that of the conventional MCrAlY coating. This is attributed to the Ti present within the HE coatings, which would oxidize rapidly to form $TiO_2$ at high temperatures, resulting in the initial weight gain. However, the weight gain of the HE coating virtually stopped after heating for 50 h and that of the MCrAlY coating increased slowly until 168 h suggesting the formation of a stable, impervious and protective oxide scale.

## Novel Coating Microstructure/Architecture

### *Tailored Coating Architecture: Multilayer Coatings*

Multifunctional multilayer systems can be used in many industrial applications, including aerospace, automotive, chemical, and petrochemical industries (Ref 247-251). These systems are a particular category of composite coatings, in which each layer has a particular functionality with precisely engineered microstructure and composition to improve the mechanical and physical properties and in turn the functional performance of the system (Ref 252-256). For boiler application, as a completely defect-free coating is needed which is difficult to produce, the alternative is to compensate for the presence of pores by adding a fully dense intermediate (metallic) layer between the substrate and the cermet top coating, which might benefit from the combined effect of both the excellent corrosion resistance of the underlying layer and the high wear resistance of the top coating. The selection of the right composition for the top and bond coats, depending on the corrosivity of the environment, is of high importance. Such a coating configuration can be a practical solution to extend the lifetimes of substrate materials and increase their performance.

### Oxide Dispersion-Strengthened (ODS) Coatings

Although ODS alloys are not commonly used in coating applications, they have long been used for high-temperature structural applications owing to their superior creep properties. Such dispersoids can be added to the feedstock material via mechanical or metallurgical alloying, or they can be produced during the spraying process by altering the process parameters. Another approach is to add them by using a hybrid spraying process (Ref 257). This process was already used (Ref 258) to fabricate composite coatings containing dispersoids. The metallic matrix alloys are fused through the wire arcing component of the process, whereas the ultrafine particles are synthesized *in-flight* by the HVOF obtained from the liquid precursors. These particulate-dispersed high-temperature composite coatings were fabricated by using the liquid precursors of $SiO_2$, $Cr_2O_3$, and $Al_2O_3$ and the wire feedstock of 55/45 NiCr in one step.

## Fabrication of Metal Matrix Composites (MMCs) Through Hybrid Spraying Techniques

MMC coatings have been widely developed and used for many high-temperature materials. The idea of MMCs was implemented to facilitate deposition of brittle materials. MMC is a composite material with at least two constituent parts, one being metal and the other being a different metal or other material. In recent years, thermal spraying has emerged among the manufacturing processes of MMC. Blending different powders and thermal spraying them on the substrate is the widely applied method. As the low deposition temperature can be achieved by the thermal spray techniques such as HVAF, or cold spray, there are no significant reactions during the spraying of mixed powders. There are other advantages such as lower oxygen content and higher density for the obtained coating. These advantages help to reduce shrinkage during any subsequent heat treatment (Ref 259-262).

The development of such coating systems seems to be the most viable method to overcome the interactions between a filler and the matrix and the degradation of composite materials in aggressive environments. However, the current efforts in this regard are not adequate for oxidation protection, though some surface treatment techniques have been established and applied to Ni-, Fe-, or Ti-based MMCs to protect them against corrosion attack in high-temperature environments (Ref 259).

*Nanocrystalline Coatings*

Nanostructured materials have attracted considerable attention over the last two decades. Nanocrystalline materials are single- or multiphase polycrystals with grain sizes in the nanometer range (typically below 100 nm in at least one dimension). In such materials, a large fraction of atoms (up to $\sim$ 50%) is located at the grain boundaries or interphase boundaries. Since they possess numerous boundaries, these materials are well known to display unique and generally improved physical, chemical, and mechanical properties compared to their conventional coarse-grained (normally micro-grained) polycrystalline counterparts. For example, nanocrystalline materials may exhibit higher thermal expansion coefficient, electrical resistivity and diffusivity, lower thermal conductivity, reduced density and elastic modulus, and increased hardness/strength, toughness/ductility, and abrasion wear resistance (Ref 160, 263, 264). Thus, nanocrystalline materials are promising for application in a wide variety of technological areas such as electronics, catalysis, ceramics, magnetic data storage, and structural components.

Due to the current difficulty in industrial-scale fabrication of bulk nanocrystalline materials with desirable properties at a reasonable cost, nanocrystalline coatings have been regarded as a preferred choice to improve the service properties of many base materials. Metal surface nanocrystallization is usually realized through techniques that can cause severe plastic deformation of the metals present in the surface layer. The techniques commonly used include surface mechanical attrition, shot peening, particle impact, circulation rolling, etc. The effects of these surface modification treatments on the mechanical properties of various metals have been extensively investigated. In addition, nanostructured surface layers can be produced by using different coating and deposition techniques such as APS, HVOF, HVAF, solution precursor plasma spraying, and suspension plasma spraying (Ref 265-267). The oxidation performances of these coatings strongly depend on their compositions and microstructures.

Based on our knowledge of the oxidation of nanocrystalline coatings, their excellent oxidation resistance can be primarily attributed to two aspects: (1) rapid formation of an external scale of chromia and/or alumina as a result of the existence of abundant grain boundaries, which function as sites for nucleation of chromia and alumina upon the onset of oxidation and thereafter provide a sufficient flux of Cr or Al to the oxide–coating interface for the rapid lateral growth of the oxide nuclei to form a continuous layer and (2) increased adhesion of the scale to the substrate, due to the modified mechanism for relaxation of scale stresses generated during oxidation and cooling, as well as due to retardation or prevention of vacancy condensation, or S segregation at the scale–coating interface. Therefore, the oxidation resistance may be greatly increased by a nanostructured coating, without the need for increasing the content of Cr or/and Al in the coatings. The service life of a thin coating is controlled not only by oxidation but also by the diffusion of the protective scale-forming element into the substrate. Although the coating may be oxidation-resistant initially, it may not be able to form a continuous surface oxide layer during long-term exposure if the element content drops below a critical level. In this case, breakaway oxidation, due to the formation of non-protective oxides, and significant internal oxidation attack may occur. Since it has a composition similar to that of the underlying metal, the interdiffusion occurring between the surface nanocrystallized layer (or nanostructured coatings such as those prepared by magnetron sputtering) and the substrate can be completely prevented. This is one of the main advantages of nanocrystalline coatings for high-temperature applications.

## Variations in Environmental Test Conditions

The corrosion behavior of thermal spray coatings has been mainly investigated in ambient air, HCl, and $H_2O$-laden environments at 400-900 °C for a short time (usually less than a week). An extensive corrosion-testing matrix should be considered in the future to establish the relationships between the process parameters, microstructure, properties, and corrosion performance. In this fashion, the corrosion performance of a coating used in different types of boilers or that deposited on different parts of a boiler can be determined. Laboratory corrosion tests performed under various environments (reducing or sulfidizing, depending on the application), different temperatures, and longer times could be highly beneficial. Long-term exposures in full-scale boilers under various conditions are recommended to evaluate the reliabilities of such coatings.

Since KCl deposit has proven to be very detrimental from a corrosion point of view, laboratory studies on coating performances in the presence of molten and solid chlorides are also highly interesting. The future work should especially focus on corrosion attack in gas atmospheres similar to those encountered by full-scale boilers, since the reactions taking place on superheater tubes may unintentionally be accelerated or retarded in the laboratory if certain components are excluded from the test atmosphere.

From full-scale investigations in biomass-fired power plants, it has been observed that a slight temperature increase above the typical steam temperature of 540 °C (which approximately corresponds to a surface metal temperature of 560 °C) can result in significantly increased corrosion rates. However, as the steam temperature in

actual superheaters can vary significantly owing to the fluctuating operating conditions, studies under controlled conditions are important to obtain a proper understanding of the influence of temperature on the corrosion of superheaters during biomass firing. From isothermal laboratory studies of KCl-coated AISI 304 austenitic stainless steel in an oxidizing atmosphere (5% $O_2$ + 40% $H_2O$), at temperatures between 400 and 600 °C (Ref 268), it has been suggested that the temperature dependence of the reaction between the deposits and the initial oxide formed on the superheater surfaces (Eq 19), as well as the ability of the ensuing oxide to offer protection, governs the alkali chloride-induced corrosion under different temperature conditions.

$$(Cr_xFe_{1-x})_2O_3(s) + 4x\mathrm{KCl}(s) + \frac{3}{2}xO_2(s) + 2xH_2O(g) = (1-x)Fe_2O_3(s) + 2x\mathrm{K_2CrO_4}(s) + 4x\mathrm{HCl}(g) \quad \text{(Eq 19)}$$

## Post-Treatment of Coatings

It is recommended that post-spray treatments are investigated for different purposes. For instance, a mechanical treatment such as shot peening can be used for grain-size control to unify the diffusion of the protective scale-forming elements toward the surface. Heat treatment can be implemented to pre-oxidize the coating to ensure the formation of a uniform and highly protective $\alpha$-$Al_2O_3$ on the surface. Moreover, heat treatment of thermal spray coatings has been reported to improve the corrosion resistance of thermal spray coatings by changing the microstructure form lamellar to bulk-like (Ref 269-271). In addition, better corrosion resistance of heat-treated coating may be attributed to the rapid formation of oxides at the coating splat boundaries and within open pores due to penetration of the oxidizing species along with the splat boundaries/open pores during heat treatment of the coated sample in an oxidizing environment (Ref 269).

Since the splat boundaries and the interconnected pores can serve as short-circuit diffusion paths for corrosive species, sealing methods have been developed. The sealing techniques include (i) impregnation of materials to fill the pores and cracks, and (ii) partial melting or sintering of the coating at the upper layer to reduce the number of open pores at the coating surface and increase the cohesion among the splats. Inorganic sealants such as Al phosphates, chromic acid, and sol–gel type solutions are primarily used for high-temperature applications, where the coatings are exposed to aggressive gases and molten salts. Several studies also reported reduced pore content and enhanced corrosion resistance of coatings treated by laser glazing. It is true that owing to the current advancements in thermal spray technologies, dense coatings without any need for post-processing can be deployed but it should be noted that this is possible only if the process parameters are carefully screened. Oksa et al. (Ref 156) investigated thermally sprayed coatings sealed with different commercial sealing agents and subjected to laser treatment. The coatings were tested after sealing by simulating fluidized bed boiler superheater conditions. The corrosion was investigated through a short-term immersion test in an alkali chloride–alkali sulfate melt that simulated superheater corrosion. The tested coatings were HVOF-sprayed NiCr and $Cr_3C_2$-25%NiCr. The protective effects of five different sealing treatments were investigated, including different commercial paints and laser fusion. No severe corrosion was observed in the tested material, and no corrosive elements were found on the coating–substrate interface. Unsealed coatings corroded slightly, and corrosive elements were detected on the lamellar boundaries. Some of the tested sealants protected the coatings adequately during the short-term alkali chloride–alkali sulfate exposure test. The best sealant contained Al oxide and Al phosphate. It endured well and protected the coating excellently. Laser-treated coatings revealed good corrosion resistance during a short-term test. However, the laser-treatment parameters should be modified to obtain a distinct melted and resolidified layer with improved resistance to both corrosion and erosion.

## Electrochemical Investigation

Molten-salt corrosion processes are electrochemical, where the salt, as an ionic conductor, allows the investigation of these processes to be carried out by using electrochemical techniques such as polarization, or EIS. Such techniques have been widely used in the study of aqueous corrosion, and have proved effective in determining and understanding of the mechanisms and kinetics of corrosion processes (Ref 272-275). Only a limited number of studies have been conducted on molten-salt corrosion, which is typically observed in biomass/waste-fired boilers (Ref 276). Moreover, the development of these techniques can result in the availability of online monitoring instruments for the assessment of electrochemical corrosion of boiler components.

## Memory Effect Due to Prior Exposure

The corrosion rates of boiler components may be affected by an earlier fuel mix, i.e., by the corrosion history of the boiler (in terms of previous deposit buildup and oxide scale formation) (Ref 277). Thus, fuel can not only influence the present corrosion rate but also leave a memory effect that influences the future corrosion rate (Ref 278). For instance,

if a boiler is first operated with non-corrosive fuels, relatively benign ash deposits will be formed on the surfaces of the heat exchangers, and the corrosion attack can be expected to be mild. If the boiler is subsequently operated with a fuel mix that is more aggressive (e.g., has a high content of alkali chlorides), aggressive ash deposits may begin forming. However, this deposit will form on top of the earlier benign deposit. Since the earlier deposit separates the material surface and this new (corrosive) deposit, it can be regarded as exhibiting some corrosion resistance.

### Self-healing

Coatings can exhibit a spontaneous "self-healing" property for self-repair in case failure occurs due to cracking or spallation of the layer (Ref 279-281). Therefore, the coating needs to act as a reservoir for the highly oxidizable metallic constituent(s) for early development of the protective scale. Self-healing may represent an innovation approach to problems with porous coatings, because the porous structure of coatings prepared by APS is inevitable, and the pores in coatings provide fast-diffusion paths for corrosive ions transportation. If the pores and cracks are filled by a self-healing agent, the diffusion of oxygen should be much slower (Ref 282). Lightweight self-healing ceramic composites for application in high-temperature aircraft engines were studied by Raj et al. (Ref 283). It was found that SiC and its oxides had sufficient plasticity to reduce crack propagation and self-healing capabilities, filling surface-connected cracks to prevent oxygen ingress. Wang et al. (Ref 284) also investigated a self-healing YSZ-La-Mo-Si heterogeneous coating fabricated by APS to protect carbon/carbon (C/C) composites from oxidation and showed that the pores of the coating surface had a mean size in the nanometer range ($< 1$ μm), which can be healed under high-temperature conditions, due to the formation of new phases, including $Mo_5Si_3$ and $MoO_3$, attributed to the reaction of present phases in the coating with $O_2$ in air at high temperatures. Meanwhile, a part of the $ZrO_2$ present was completely transformed from the tetragonal phase to the monoclinic phase, and simultaneously, the rest of the $ZrO_2$ phase was fully converted to $ZrSiO_4$. The conversion of the raw coating materials into $SiO_2$, $La_2O_3$, $ZrSiO_4$, and $Y_2SiO_5$ resulted in volume expansion and the formation of a Zr-Y-La-Si-O oxide scale. Such volume expansion of the solid phase led to compressive stress that weakened the thermal stress generated during the oxidation process. The presence of compressive stress and the Zr-Y-La-Si-O oxide scale is conducive for healing the microcracks and pores present in the coating, thus protecting the coating from oxidation. Without the compressive stress, the thermal stress resulting from a mismatch in the CTE between the coating and the substrate initiated cracks that eventually destroyed the integrity of the coating.

### Modeling

As has been demonstrated conclusively, ion transport in chromia and alumina is predominantly a grain boundary process. What is now needed is a modeling capability, particularly based on an atomic-level description of the movement of individual species along with a boundary. Since the boundaries are surfaces, they will be surrounded by narrow space–charge regions. Moreover, as transport occurs within the same narrow zones, the space–charge effects cannot be ignored. Experimental measurements of the grain boundary diffusion parameters have been applied to the growth of NiO scales (Ref 285).

Modeling of $Cr_2O_3$ and $Al_2O_3$ is more difficult because of the increased importance of impurity effects. As already discussed, alloying elements, reactive metals, and gas-phase constituents all segregate at the grain boundaries. The interactions between these various species and with the oxide constituents also need to be modeled. The application of high-resolution microscopy techniques, including atom probe tomography, to grain boundaries dosed with different mixtures of segregant species seems likely to be rewarding.

## Concluding Remarks

The second part of the review paper addresses the high-temperature corrosion behavior of thermal spray coatings in harsh corrosion-prone environments and provides a comprehensive overview of the underlying high-temperature corrosion mechanisms that lead to the failure of the coatings. Various types of coatings in different corrosive environments including ambient air, HCl- and moisture-laden with the addition of corrosive salts that are typical of biomass-fired boilers were discussed. Despite some variations in the microstructure of the coatings produced by different processes, thermal spray coatings play a vital role in protecting the substrate materials and alloys from high-temperature corrosion. A dense and defect-free coating that shows high integrity with the substrate material has proved to be effective in such corrosive environments. Due to the presence of many corrosive species like Cl in the environment, the chromia-forming coatings cannot show their excellent characteristics to protect the underlying material. As long as the formation of an α-alumina is promoted on the surface (by heat treatment, and mechanical working, etc.), the alumina-forming coatings can be a better solution in such environments. Regardless of the cost, nanostructured coatings or coatings containing rare-earth elements

have also applications in this particular area but still a lot of effort and different combinations of coatings have been explored.

There are opportunities to develop new theories and methodologies to evaluate the microstructure, properties, and performance of alumina- or chromia-forming thermal spray coatings in the presence of various corrosive species like water vapor or HCl. While the current corrosion theories can be applied on thermal spray coatings, the fundamental differences between the alloys and thermal spray coatings need to be understood.

Regarding characterization of the pre- and post-exposed coatings, in general, the weight change measurement technique is economical and has become popular as a way of generating comparative alloy performance data under more realistic exposure conditions. However, it is necessary to use a combination of this measurement with more advanced analytical tools to overcome the difficulties. The functional differences between the characterization techniques in terms of detection limit and spatial resolution were discussed in the review.

Challenges also remain in improving the productivities of thermal spray processes, enhancing the performances of thermal spray coatings, lowering the high cost of producing quality metal powders, and making the equipment more affordable. Many unique technical capabilities such as spraying in small-diameter pipes, onsite spraying of boiler components, and repairing the worn coatings provide unprecedented business opportunities for thermal spraying. A more comprehensive understanding of the thermal spray processes and the innovations in these areas are needed for greater technological adaptation of the thermal spray processes.

**Acknowledgments** Open Access funding provided by University West. Financial support of the Knowledge Foundation for the SCoPe Project (RUN 20160201) and Västra Götalandsregionen (VGR) for the PROSAM Project (RUN 2016-01489) is highly acknowledged.



**Data availability** All data included in this study are available upon request by contact with the corresponding author.

## References

1. P. Fauchais and A. Vardelle, "Thermal Sprayed Coatings Used Against Corrosion and Corrosive Wear," in *Advanced plasma spray applications*, InTech, 2012
2. K. Szymański, A. Hernas, G. Moskal, and H. Myalska, Thermally Sprayed Coatings Resistant to Erosion and Corrosion for Power Plant Boilers—A Review, *Surf. Coat. Technol.*, 2015, **268**, p 153-164
3. D. Mudgal, S. Singh, and S. Prakash, Corrosion Problems in Incinerators and Biomass-Fuel-Fired Boilers, *Int. J. Corros.* 2014, **2014**
4. S.A. Galedari, A. Mahdavi, F. Azarmi, Y. Huang, and A. McDonald, A Comprehensive Review of Corrosion Resistance of Thermally-Sprayed and Thermally-Diffused Protective Coatings on Steel Structures, *J. Therm. Spray Technol.*, 2019, **28**(4), p 645-677
5. R. Viswanathan, K. Coleman, and U. Rao, Materials for Ultra-Supercritical Coal-Fired Power Plant Boilers, *Int. J. Press. Vessels Pip.*, 2006, **83**(11-12), p 778-783
6. T. Sharobem and M. J. Castaldi, The Effect of SO2/HCl Ratio on Superheater High Temperature Corrosion, Presented at the 20th Annual North American Waste-to-Energy Conference, NAWTEC 2012, 2012, p 23-27
7. X. Ren, E. Rokni, Y. Liu, and Y.A. Levendis, Reduction of HCl Emissions from Combustion of Biomass by Alkali Carbonate Sorbents or by Thermal Pretreatment, *J. Energy Eng.*, 2018, **144**(4), p 04018045
8. M. Bai, L. Reddy, and T. Hussain, Experimental and Thermodynamic Investigations on the Chlorine-Induced Corrosion of HVOF Thermal Sprayed NiAl Coatings and 304 Stainless Steels at 700 °C, *Corros. Sci.*, 2018, **135**, p 147-157
9. D.L. Wu, K.V. Dahl, T.L. Christiansen, M. Montgomery, and J. Hald, Microstructural Investigations of Ni and Ni2Al3 Coatings Exposed in Biomass Power Plants, *Mater. High Temp.*, 2018, **35**(1-3), p 255-266
10. Y.C. Malede, M. Montgomery, K.V. Dahl, and J. Hald, Effect of Microstructure on KCl Corrosion Attack of Modified AISI, 310 Steel, *Mater. High Temp.*, 2018, **35**(1-3), p 243-254
11. S.C. Okoro, M. Montgomery, F.J. Frandsen, and K. Pantleon, Influence of Preoxidation on High-Temperature Corrosion of a FeCrAl Alloy Under Conditions Relevant to Biomass Firing, *Oxid. Met.*, 2018, **89**(1-2), p 99-122
12. M. Spiegel, A. Zahs, and H.J. Grabke, Fundamental Aspects of Chlorine induced corrosion in power plants, *Mater. High Temp.*, 2003, **20**(2), p 153-159
13. J. Pettersson, H. Asteman, J.-E. Svensson, and L.-G. Johansson, KCl Induced Corrosion of a 304-type Austenitic Stainless Steel at 600 °C; The Role of Potassium, *Oxid. Met.*, 2005, **64**(1-2), p 23-41
14. G. Gao, F.H. Stott, J.L. Dawson, and D.M. Farrell, Electrochemical Monitoring of High-Temperature Molten-Salt Corrosion, *Oxid. Met.*, 1990, **33**(1-2), p 79-94
15. Y. Kawahara, Role of Molten Phase Content of Deposits for High-Temperature Corrosion in Waste Incineration Environment, *Mater. High Temp.*, 1997, **14**(3), p 269-276
16. H.P. Nielsen, F.J. Frandsen, K. Dam-Johansen, and L.L. Baxter, Implications of Chlorine-Associated Corrosion on the Operation of Biomass-Fired Boilers, *Prog. Energy Combust. Sci.*, 2000, **26**(3), p 283-298
17. J. Kalivodova, D. Baxter, M. Schütze, and V. Rohr, Gaseous Corrosion of Alloys and Novel Coatings in Simulated Environments for Coal, Waste and Biomass Boilers, *Mater. Corros.*, 2005, **56**(12), p 882-889
18. Y.Y. Lee and M.J. McNallan, Ignition of Nickel in Environments Containing Oxygen and Chlorine, *Metall. Trans. A Phys. Metall. Mater. Sci.*, 1987, **18A**(6), p 1099-1107
19. A. Zahs, M. Spiegel, and H.J. Grabke, Chloridation and Oxidation of iron, Chromium, Nickel and Their Alloys in Chloridizing and Oxidizing Atmospheres at 400-700 °C, *Corros. Sci.*, 2000, **42**(6), p 1093-1122

20. M. Spiegel, Reactions Between Gas Phase, Deposits and Metallic Materials in Chlorine Containing Atmospheres, *Mater. High Temp.*, 1997, **14**(3), p 221-226
21. N. Folkeson, T. Jonsson, M. Halvarsson, L.-G. Johansson, and J.-E. Svensson, The Influence of Small Amounts of KCl(s) on the High Temperature Corrosion of a Fe-2.25Cr-1Mo Steel at 400 and 500 °C, *Mater. Corros.*, 2011, **62**(7), p 606-615
22. C. Pettersson, J. Pettersson, H. Asteman, J.-E. Svensson, and L.-G. Johansson, KCl-Induced High Temperature Corrosion of the Austenitic Fe-Cr-Ni Alloys 304L and Sanicro 28 at 600 °C, *Corros. Sci.*, 2006, **48**(6), p 1368-1378
23. Y. Shinata, Accelerated Oxidation Rate of Chromium Induced by Sodium Chloride, *Oxid. Met.*, 1987, **27**(5-6), p 315-332
24. T. Ishitsuka and K. Nose, Stability of Protective Oxide Films in Waste Incineration Environment—Solubility Measurement of Oxides in Molten Chlorides, *Corros. Sci.*, 2002, **44**(2), p 247-263
25. A. Zahs, M. Spiegel, and H. Grabke, The Influence of Alloying Elements on the Chlorine-Induced High Temperature Corrosion of Fe-Cr Alloys in Oxidizing Atmospheres, *Mater. Corros.*, 1999, **50**(10), p 561-578
26. M. Spiegel, The Role of Molten Salts in the Corrosion of Metals in Waste Incineration Plants, *Molten Salt Forum*, 2003, **7**, p 253-268
27. D. Bankiewicz, Corrosion Behaviour of Boiler Tube Materials During Combustion of Fuels Containing Zn and Pb, Ph.D. thesis, Åbo Akademi University, 2012
28. S.C. Cha and M. Spiegel, Local Reactions of KCl Particles with Iron, Nickel and Chromium Surfaces, *Mater. Corros.*, 2006, **57**(2), p 159-164
29. P. Viklund, Superheater Corrosion in Biomass and Waste Fired Boilers: Characterisation, Causes and Prevention of Chlorine-Induced Corrosion, PhD Thesis, KTH Royal Institute of Technology, 2013
30. D. Lindberg, M. Becidan, and L. Sørum, High Efficiency Waste-to-Energy Plants—Effect of Ash Deposit Chemistry on Corrosion at Increased Superheater Temperatures, *Energy Fuels*, 2010, **24**(10), p 5387-5395
31. A. Talus, R. Norling, L. Wickström, and A. Hjörnhede, Effect of Lead Content in Used Wood Fuel on Furnace Wall Corrosion of 16Mo3, 304L and Alloy 625, *Oxid. Met.*, 2017, **87**(5-6), p 813-824
32. H. Kinnunen et al., High-Temperature Corrosion Due to Lead Chloride Mixtures Simulating Fireside Deposits in Boilers Firing Recycled Wood, *Fuel Process. Technol.*, 2017, **167**, p 306-313
33. H. Kinnunen et al., The Influence of Flue Gas Temperature on Lead Chloride Induced High Temperature Corrosion, *Fuel*, 2017, **196**, p 241-251
34. D. Bankiewicz, S. Enestam, P. Yrjas, and M. Hupa, Experimental Studies of Zn and Pb Induced High Temperature Corrosion of Two Commercial Boiler Steels, *Fuel Process. Technol.*, 2013, **105**, p 89-97
35. S. Enestam, R. Backman, K. Mäkelä, and M. Hupa, Evaluation of the Condensation Behavior of Lead and Zinc in BFB Combustion of Recovered Waste Wood, *Fuel Process. Technol.*, 2013, **105**, p 161-169
36. J. Niemi, H. Kinnunen, D. Lindberg, and S. Enestam, Interactions of $PbCl_2$ with Alkali Salts in Ash Deposits and Effects on Boiler Corrosion, *Energy Fuels*, 2018, **32**(8), p 8519-8529
37. D. J. Young, Chapter 11—Effects of Water Vapour on Oxidation, in *High Temperature Oxidation and Corrosion of Metals*, 2nd edn. Elsevier, 2016, p 549-601
38. C.T. Fujii and R.A. Meussner, The Mechanism of the High-Temperature Oxidation of Iron-Chromium Alloys in Water Vapor, *J. Electrochem. Soc.*, 1964, **111**(11), p 1215-1221
39. A. Galerie, S. Henry, Y. Wouters, M. Mermoux, J.-P. Petit, and L. Antoni, Mechanisms of Chromia Scale Failure During the Course of 15-18Cr Ferritic Stainless Steel Oxidation in Water Vapour, *Mater. High Temp.*, 2005, **22**(1-2), p 105-112
40. H. Asteman, J.-E. Svensson, and L.-G. Johansson, Evidence for Chromium Evaporation Influencing the Oxidation of 304L: The Effect of Temperature and Flow Rate, *Oxid. Met.*, 2002, **57**(3-4), p 193-216
41. J. Ehlers et al., Enhanced Oxidation of the 9%Cr Steel P91 in Water Vapour Containing Environments, *Corros. Sci.*, 2006, **48**(11), p 3428-3454
42. D.J. Young, J. Zurek, L. Singheiser, and W.J. Quadakkers, Temperature Dependence of Oxide Scale Formation on High-Cr Ferritic Steels in Ar-H2-$H_2O$, *Corros. Sci.*, 2011, **53**(6), p 2131-2141
43. J. Zurek et al., Growth and Adherence of Chromia Based Surface Scales on Ni-Base Alloys in High- and low-pO2 Gases, *Mater. Sci. Eng. A*, 2008, **477**(1), p 259-270
44. E. Essuman et al., Protective and Non-protective Scale Formation of NiCr Alloys in Water Vapour Containing High- and Low-pO2 Gases, *Corros. Sci.*, 2008, **50**(6), p 1753-1760
45. W.J. Quadakkers, J. Żurek, and M. Hänsel, Effect of Water Vapor on High-Temperature oxidation of FeCr Alloys, *JOM*, 2009, **61**(7), p 44-50
46. M. Schütze, D. Renusch, and M. Schorr, Parameters Determining the Breakaway Oxidation Behaviour of Ferritic Martensitic 9%Cr Steels in Environments Containing $H_2O$, *Corros. Eng. Sci. Technol.*, 2004, **39**(2), p 157-166
47. M. Schütze, M. Schorr, D.P. Renusch, A. Donchev, and J.P.T. Vossen, The Role of Alloy Composition, Environment and Stresses for the Oxidation Resistance of Modern 9% Cr Steels for Fossil Power Stations, *Mater. Res.*, 2004, **7**(1), p 111-123
48. G. Hultquist, B. Tveten, and E. Hörnlund, Hydrogen in Chromium: Influence on the High-Temperature Oxidation Kinetics in $H_2O$, Oxide-Growth Mechanisms, and Scale Adherence, *Oxid. Met.*, 2000, **54**(1), p 1-10
49. L. Mikkelsen and S. Linderoth, High Temperature Oxidation of Fe-Cr Alloy in $O_2$-$H_2$-$H_2O$ Atmospheres; Microstructure and Kinetics, *Mater. Sci. Eng. A*, 2003, **361**(1), p 198-212
50. M. Hänsel, L. Garcia-Fresnillo, S.L. Tobing, and V. Shemet, Effect of $H_2/H_2O$ Ratio on Thermally Grown Chromia Scales Formed on Ni25Cr Alloy in Ar-$H_2$-$H_2O$ Atmospheres at 1000 °C, *Mater. High Temp.*, 2012, **29**(3), p 187-192
51. T. Jonsson et al., Oxidation of Fe-10Cr in $O_2$ and in $O_2 + H_2O$ Environment at 600 °C: A Microstructural Investigation, *Corros. Sci.*, 2013, **75**, p 326-336
52. D.J. Young, *High Temperature Oxidation and Corrosion of Metals*, Vol 1, Elsevier, Amsterdam, 2008
53. S. Andersson et al., Sulfur Recirculation for Increased Electricity Production in Waste-to-Energy Plants, *Waste Manag.*, 2014, **34**(1), p 67-78
54. L.P. Belo et al., High-Temperature Conversion of $SO_2$ to $SO_3$: Homogeneous Experiments and Catalytic Effect of Fly Ash from Air and Oxy-Fuel Firing, *Energy Fuels*, 2014, **28**(11), p 7243-7251
55. M. Oksa, T. Varis, and K. Ruusuvuori, Performance Testing of Iron Based Thermally Sprayed HVOF Coatings in a Biomass-Fired Fluidised Bed Boiler, *Surf. Coat. Technol.*, 2014, **251**, p 191-200
56. M. Stauber Alfredsson, Effects of Different Fuels on Combustion Boiler Processes: The Analysis of Alternative Fuel Mixtures, PhD thesis, KTH Royal Institute of Technology, 2018
57. R. Jafari, E. Sadeghimeresht, T.S. Farahani, M. Huhtakangas, N. Markocsan, and S. Joshi, KCl-Induced High-Temperature Corrosion Behavior of HVAF-Sprayed Ni-Based Coatings in Ambient Air, *J. Therm. Spray Technol.*, 2018, **27**(3), p 500-511

58. E. Sadeghimeresht, N. Markocsan, M. Huhtakangas, and S. Joshi, Isothermal Oxidation of HVAF-Sprayed Ni-Based Chromia, Alumina and Mixed-Oxide Scale Forming Coatings in Ambient Air, *Surf. Coat. Technol.*, 2017, **316**, p 10-21
59. T.S. Bedi, S.S. Aulakh, and G. Kaushal, Corrosion Studies on HVOF Sprayed Ni-20Cr and Ni-50Cr Coatings on ASTM A213 TP347H Boiler Steel at 7000 °C, *Asian Rev. Mech. Eng.*, 2013, **2**(2), p 56-60
60. H. Singh, M. Kaur, and S. Prakash, High-Temperature Exposure Studies of HVOF-Sprayed Cr3C2-25 (NiCr)/(WC-Co) Coating, *J. Therm. Spray Technol.*, 2016, **25**(6), p 1192-1207
61. B. Song, M. Bai, K.T. Voisey, and T. Hussain, Role of Oxides and Porosity on High-Temperature Oxidation of Liquid-Fueled HVOF Thermal-Sprayed Ni50Cr Coatings, *J. Therm. Spray Technol.*, 2017, **26**(3), p 554-568
62. D. Fantozzi, V. Matikainen, M. Uusitalo, H. Koivuluoto, and P. Vuoristo, Effect of Carbide Dissolution on Chlorine Induced High Temperature Corrosion of HVOF and HVAF Sprayed $Cr_3C_2$-NiCrMoNb Coatings, *J. Therm. Spray Technol.*, 2018, **27**(1-2), p 220-231
63. C. Jiang et al., The Corrosion Behaviours of Plasma-Sprayed Fe-Based Amorphous Coatings, *Surf. Eng.*, 2018, **34**(8), p 634-639
64. E. Sadeghi and S. Joshi, Chlorine-Induced High-Temperature Corrosion and Erosion-Corrosion of HVAF and HVOF-Sprayed Amorphous Fe-Based Coatings, *Surf. Coat. Technol.*, 2019, **371**, p 20-35
65. R.K. Kumar, M. Kamaraj, S. Seetharamu, T. Pramod, and P. Sampathkumaran, Effect of Spray Particle Velocity on Cavitation Erosion Resistance Characteristics of HVOF and HVAF Processed 86WC-10Co4Cr Hydro Turbine Coatings, *J. Therm. Spray Technol.*, 2016, **25**(6) p 1-14
66. P. Alnegren, Oxidation Behavior of Selected FeCr Alloys in Environments Relevant for Solid Oxide Electrolysis Applications, *Chalmers studentarbeten*, 2012. http://studentarbeten.chalmers.se. Accessed 03 Apr 2018
67. A. Agüero, I. Baráibar, M. Gutiérrez, M. Hernández, R. Muelas, and S. Rodríguez, Biomass Corrosion Behavior of Steels and Coatings in Contact with KCl/K2SO4 at 550 °C Under an Oxy-Fuel Combustion Atmosphere: A Screening Laboratory Test, *Surf. Coat. Technol.*, 2018, **350**, p 188-200
68. T. Varis et al., High Temperature Corrosion of Thermally Sprayed NiCr and FeCr Coatings Covered with a KCl–$K_2SO_4$ Salt Mixture, *Surf. Coat. Technol.*, 2015, **265**, p 235-243
69. A.J. López, M. Proy, V. Utrilla, E. Otero, and J. Rams, High-Temperature Corrosion Behavior of Ni-50Cr Coating Deposited by High Velocity Oxygen-Fuel Technique on Low Alloy Ferritic Steel, *Mater. Des.*, 2014, **59**, p 94-102
70. M. Kumar, H. Singh, and N. Singh, Study of Ni-20Cr Coatings for High Temperature Applications—A Review, *Arch. Metall. Mater.*, 2013, **58**(2), p 523-528
71. E. Sadeghimeresht, Ni-Based Coatings for High Temperature Corrosion Protection, Ph.D. thesis, University West, 2018
72. E. Sadeghimeresht, J. Eklund, J.P. Simon, J. Liske, N. Markocsan, and S. Joshi, Effect of Water Vapor on the Oxidation Behavior of HVAF-Sprayed NiCr and NiCrAlY Coatings, *Mater. Corros.*, 2018, **69**(10), p 1431-1440
73. E. Sadeghimeresht, J. Eklund, J. Phother Simon, J. Liske, N. Markocsan, and S.V. Joshi, HVAF Spraying for Biomass Boiler Applications: Oxidation Behavior of Ni-Based Coatings in Moisture-Laden Environment, presented at the International Thermal Spray Conference & Exposition, ITSC 2017, Düsseldorf, Germany, June 7-9, 2017, 2017
74. E. Sadeghimeresht, J. Eklund, J. Phother Simon, J. Lyske, N. Markocsan, and S. V. Joshi, Oxidation Behaviour of HVAF-Sprayed NiCr Coating in Moisture-Laden Environment, presented at the international Thermal Spray Conference and Exposition, ITSC 2017; Dusseldorf; Germany; 7 June 2017 through 9 June 2017, 2017, vol 2, p 644-646
75. T. Sundararajan, S. Kuroda, and F. Abe, Steam Oxidation Resistance of Two-Layered Ni-Cr and Al APS Coating for USC Boiler Applications, *Corros. Sci.*, 2005, **47**(5), p 1129-1147
76. M. Oksa, S. Tuurna, and T. Varis, Increased Lifetime for Biomass and Waste to Energy Power Plant Boilers with HVOF Coatings: High Temperature Corrosion Testing Under Chlorine-Containing Molten Salt, *J. Therm. Spray Technol.*, 2013, **22**(5), p 783-796
77. N. Hussain, K.A. Shahid, I.H. Khan, and S. Rahman, Oxidation of High-Temperature Alloys (Superalloys) at Elevated Temperatures in Air: I, *Oxid. Met.*, 1994, **41**(3-4), p 251-269
78. N. Hussain, A.H. Qureshi, K.A. Shahid, N.A. Chughtai, and F.A. Khalid, High-Temperature Oxidation Behavior of HASTELLOY C-4 in Steam, *Oxid. Met.*, 2004, **61**(5-6), p 355-364
79. C. Zhou, J. Yu, S. Gong, and H. Xu, Influence of Water Vapor on the Isothermal Oxidation Behavior of Low Pressure Plasma Sprayed NiCrAlY Coating at High Temperature, *Surf. Coat. Technol.*, 2002, **161**(1), p 86-91
81. L. Intiso, L.-G. Johansson, S. Canovic, S. Bellini, J.-E. Svensson, and M. Halvarsson, Oxidation Behaviour of Sanicro 25 (42Fe22Cr25NiWCuNbN) in $O_2$/$H_2O$ Mixture at 600 °C, *Oxid. Met.*, 2012, **77**(5-6), p 209-235
82. N.K. Othman, N. Othman, J. Zhang, and D.J. Young, Effects of Water Vapour on Isothermal Oxidation of Chromia-Forming Alloys in Ar/O2 and Ar/H2 Atmospheres, *Corros. Sci.*, 2009, **51**(12), p 3039-3049
83. A. Galerie, Y. Wouters, and M. Caillet, The Kinetic Behaviour of Metals in Water Vapour at High Temperatures: Can General Rules Be Proposed?, *Mater. Sci. Forum*, 2001, **369-372**, p 231-238
84. M.A. Uusitalo, P.M.J. Vuoristo, and T.A. Mäntylä, High Temperature Corrosion of Coatings and Boiler Steels in Oxidizing Chlorine-Containing Atmosphere, *Mater. Sci. Eng. A*, 2003, **346**(1), p 168-177
85. S. Paul and M.D.F. Harvey, Corrosion Testing of Ni Alloy HVOF Coatings in High Temperature Environments for Biomass Applications, *J. Therm. Spray Technol.*, 2013, **22**(2-3), p 316-327
86. L. Reddy, P. Shipway, C. Davis, and T. Hussain, HVOF and Laser-Cladded Fe-Cr-B Coating in Simulated Biomass Combustion: Microstructure and Fireside Corrosion, *Oxid. Met.*, 2017, **87**(5-6), p 825-835
87. E. Sadeghimeresht, L. Reddy, T. Hussain, M. Huhtakangas, N. Markocsan, and S. Joshi, Influence of KCl and HCl on High Temperature Corrosion of HVAF-Sprayed NiCrAlY and NiCrMo Coatings, *Mater. Des.*, 2018, **148**, p 17-29
88. E. Sadeghimeresht, L. Reddy, T. Hussain, N. Markocsan, and S. Joshi, Chlorine-Induced High Temperature Corrosion of HVAF-Sprayed Ni-Based Alumina and Chromia Forming Coatings, *Corros. Sci.*, 2018, **132**, p 170-184
89. Y. Shu, F. Wang, and W. Wu, Corrosion Behavior of Pure Cr with a Solid NaCl Deposit in $O_2$ Plus Water Vapor, *Oxid. Met.*, 2000, **54**(5-6), p 457-471
90. N. Israelsson et al., A Microstructural and Kinetic Investigation of the KCl-Induced Corrosion of an FeCrAl Alloy at 600 °C, *Oxid. Met.*, 2015, **84**(1-2), p 105-127
91. R. Bender and M. Schütze, The Role of Alloying Elements in Commercial Alloys for Corrosion Resistance in Oxidizing-Chloridizing Atmospheres Part I: Literature Evaluation and Thermodynamic Calculations on Phase Stabilities, *Mater. Corros.*, 2003, **54**(8), p 567-586
92. Y.S. Li and M. Spiegel, Internal Oxidation of Fe-Al Alloys in a KCl-Air Atmosphere at 650 °C, *Oxid. Met.*, 2004, **61**(3-4), p 303-322

93. N. Israelsson, K.A. Unocic, K. Hellström, J.-E. Svensson, and L.-G. Johansson, Cyclic Corrosion and Chlorination of an FeCrAl Alloy in the Presence of KCl, *Oxid. Met.*, 2015, **84**(3-4), p 269-290
94. J. Eklund, J. Phother, E. Sadeghi, S. Joshi, and J. Liske, High-Temperature Corrosion of HVAF-Sprayed Ni-Based Coatings for Boiler Applications, *Oxid. Met.*, 2019, **91**(5-6), p 729-747
95. K.N. Strafford, P.K. Datta, and G. Forster, High-Temperature Chloridation of Binary Fe·Cr Alloys at 1000 °C, *Mater. Sci. Eng. A*, 1989, **120-121**, p 61-68
96. H. Chu, P.K. Datta, and K.N. Strafford, Corrosion Behavior of Fe(Ni)CrAIX Alloys in an HCl-$H_2O$-$H_2$ Gas Mixture at 800 °C, *Oxid. Met.*, 1995, **43**(5-6), p 491-508
97. E. Sadeghimeresht, H. Hooshyar, N. Markocsan, S. Joshi, and P. Nylén, Oxidation Behavior of HVAF-Sprayed NiCoCrAlY Coating in $H_2$-$H_2O$ Environment, *Oxid. Met.*, 2016, **86**(3-4), p 299-314
98. E. Sadeghimeresht, N. Markocsan, and S. Joshi, Isothermal Oxidation Behavior of HVAF-Sprayed Ni and NiCr Coatings in $H_2$-$H_2O$ Environment, *Surf. Coat. Technol.*, 2017, **317**, p 17-25
99. M.A. Uusitalo, P.M.J. Vuoristo, and T.A. Mäntylä, High Temperature Corrosion of Coatings and Boiler Steels in Reducing Chlorine-Containing Atmosphere, *Surf. Coat. Technol.*, 2002, **161**(2-3), p 275-285
100. E. Sadeghi, N. Markocsan, T. Hussain, M. Huhtakangas, and S. Joshi, Effect of SiO2 Dispersion on Chlorine-Induced High-Temperature Corrosion of High-Velocity Air-Fuel Sprayed NiCrMo Coating, *CORROSION*, 2018, p 984-1000
101. G. Hou, Y. Ja, X. Zhao, H. Zhou, and J. Chen, Effect of Alumina Dispersion on Oxidation Behavior as Well as Friction and Wear Behavior of HVOF-Sprayed CoCrAlYTaCSi Coating at Elevated Temperature Up To 1000 °C, *Acta Mater.*, 2015, **95**(Supplement C), p 164-175
102. T. Huang, J. Bergholz, G. Mauer, R. Vassen, D. Naumenko, and W.J. Quadakkers, Effect of Test Atmosphere Composition on High-Temperature Oxidation Behaviour of CoNiCrAlY Coatings Produced from Conventional and ODS Powders, *Mater. High Temp.*, 2017, **35**(3) p 97-107
103. K.A. Unocic, et al., High-Temperature Behavior of Oxide Dispersion Strengthening CoNiCrAlY, *Mater. High Temp.*, 2017, **35**(3) p 108-119
104. K. Arnold, G. Tatlock, C. Kenel, A. Colella, and P. Matteazzi, High Temperature Isothermal Oxidation Behaviour of an Oxide Dispersion Strengthened Derivative of IN625, *Mater. High Temp.*, 2018, **35**(1-3), p 141-150
105. J. Stringer, B.A. Wilcox, and R.I. Jaffee, The High-Temperature Oxidation of Nickel-20 wt.% Chromium Alloys Containing Dispersed Oxide Phases, *Oxid. Met.*, 1972, **5**(1), p 11-47
106. C.S. Giggins and F.S. Pettit, The Oxidation of TD NiC (Ni-20Cr-2 vol pct ThO2) Between 900° and 1200 °C, *MT*, 1971, **2**(4), p 1071-1078
107. B.A. Pint, Study of the Reactive Element Effect in ODS Iron-Base Alumina Formers, *Mater. Sci. Forum*, 1997, **251-254**, p 397-404
108. J. Guilemany, J. Fernández, and J. Delgado, Electrochemical Measurements and Characterisation of a Thermal Sprayed HVOF Cr3C2 Coating in a Corrosive Environment, in *ITSC*, Düsseldorf, Germany, p 474-478
109. J.M. Guilemany, J. Fernández, J. Delgado, A.V. Benedetti, and F. Climent, Effects of Thickness Coating on the Electrochemical Behaviour of Thermal Spray Cr3C2-NiCr Coatings, *Surf. Coat. Technol.*, 2002, **153**(2-3), p 107-113
110. A.P. Wang, T. Zhang, and J.Q. Wang, Ni-Based Fully Amorphous Metallic Coating with High Corrosion Resistance, *Philos. Mag. Lett.*, 2006, **86**(1), p 5-11
111. S.D. Zhang, W.L. Zhang, S.G. Wang, X.J. Gu, and J.Q. Wang, Characterisation of Three-Dimensional Porosity in an Fe-Based Amorphous Coating and Its Correlation with Corrosion Behaviour, *Corros. Sci.*, 2015, **93**, p 211-221
112. E. Sadeghimeresht, N. Markocsan, P. Nylén, and S. Björklund, Corrosion Performance of Bi-Layer Ni/Cr2C3-NiCr HVAF Thermal Spray Coating, *Appl. Surf. Sci.*, 2016, **369**, p 470-481
113. E. Sadeghimeresht, N. Markocsan, and P. Nylén, Microstructural and Electrochemical Characterization of Ni-Based Bi-Layer Coatings Produced by the HVAF Process, *Surf. Coat. Technol.*, 2016, **304**, p 606-619
114. E. Sadeghimeresht, N. Markocsan, and P. Nylén, Microstructure Effect of Intermediate Coat Layer on Corrosion Behavior of HVAF-Sprayed Bi-Layer Coatings, *J. Therm. Spray Technol.*, 2017, **26**(1-2), p 243-253
115. E. Sadeghimeresht, N. Markocsan, and P. Nylen, Corrosion Behavior of HVAF-Sprayed Bi-Layer Coatings: Effect of Intermediate Layer's Microstructure and Composition, in *DIVA*, 2017, p 1-1
116. E. Sadeghimeresht and N. Markocsan, Electrochemical Behavior of Bilayer Thermal-Spray Coatings in Low-Temperature Corrosion Protection, *Coatings*, 2017, **7**(10), p 162
117. E. Sadeghimeresht, N. Markocsan, and P. Nylén, Microstructural Characteristics and Corrosion Behavior of HVAF- and HVOF-Sprayed Fe-Based Coatings, *Surf. Coat. Technol.*, 2017, **318**, p 365-373
118. E. Sadeghimeresht, N. Markocsan, and P. Nylén, Duplex Thermal Spray Coatings: A Critical Approach to Extend the Service-Life of Metallic Components, presented at the ITSC 2016, International Thermal Spray Conference, Shanghai, P.R. China, May 10-12, 2016
119. E. Sadeghimeresht, Corrosion Behavior of HVAF-Sprayed Bi-Layer Coatings, Licentiate thesis, University West, 2016
120. E. Sadeghimeresht, N. Markocsan, and P. Nylen, Corrosion Behavior of HVAF-Sprayed Bi-Layer Coatings: Effect of Intermediate Layer&Apos;S Microstructure and Chemical Composition, presented at the International Thermal Spray Conference & Exposition, ITSC 2017, Düsseldorf, Germany, June 7-9, 2017, 2, p 941-945
121. D. Wu, K.V. Dahl, J.L. Madsen, T.L. Christiansen, M. Montgomery, and J. Hald, Effects of Different Fuel Specifications and Operation Conditions on the Performance of Coated and Uncoated Superheater Tubes in Two Different Biomass-Fired Boilers, *ACS Appl. Energy Mater.*, 2018, **1**(4), p 1463-1475
122. S.-H. Lee, N.J. Themelis, and M.J. Castaldi, High-Temperature Corrosion in Waste-to-Energy Boilers, *J. Therm. Spray Technol.*, 2007, **16**(1), p 104-110
123. P. Rademakers, W. Hesseling, and J. Van de Wetering, Review on Corrosion in Waste Incinerators, and Possible Effect of Bromine, *TNO Ind. Technol.*, p 18-25, 2002
124. Y. Kawahara, High Temperature Corrosion Mechanisms and Effect of Alloying Elements for Materials Used in Waste Incineration Environment, *Corros. Sci.*, 2002, **44**(2), p 223-245
125. S.M. Jiang, H.Q. Li, J. Ma, C.Z. Xu, J. Gong, and C. Sun, High Temperature Corrosion Behaviour of a Gradient NiCoCrAlYSi Coating II: Oxidation and Hot Corrosion, *Corros. Sci.*, 2010, **52**(7), p 2316-2322
126. B.S. Covino, G.R. Holcomb, S.D. Cramer, S.J. Bullard, M. Ziomek-Moroz, and M.L. White, Corrosion in a Temperature Gradient, in *17th Annual Conference on Fossil Energy Materials, Baltimore, MD (US)*, 2003, 4, p 04
127. Y. Kawahara, K. Takahashi, Y. Nakagawa, T. Hosoda, and T. Mizuko, Demonstration Test of New Corrosion-Resistant Superheater Tubings in a High Efficiency Waste-to-Energy Plant, in *CORROSION 2000*, 2000

128. B.-J. Skrifvars, R. Backman, M. Hupa, K. Salmenoja, and E. Vakkilainen, Corrosion of Superheater Steel Materials Under Alkali Salt Deposits Part 1: The Effect of Salt Deposit Composition and Temperature, *Corros. Sci.*, 2008, **50**(5), p 1274-1282
129. S. Enestam, D. Bankiewicz, J. Tuiremo, K. Mäkelä, and M. Hupa, Are NaCl and KCl Equally Corrosive on Superheater Materials of Steam Boilers?, *Fuel*, 2013, **104**, p 294-306
130. H.J. Grabke, E. Reese, and M. Spiegel, The Effects of Chlorides, Hydrogen Chloride, and Sulfur Dioxide in the Oxidation of Steels Below Deposits, *Corros. Sci.*, 1995, **37**(7), p 1023-1043
131. R. Jafari and E. Sadeghi, High-Temperature Corrosion Performance of HVAF-Sprayed NiCr, NiAl, and NiCrAlY Coatings with Alkali Sulfate/Chloride Exposed to Ambient Air, *Corros. Sci.*, 2019, **160**, p 108066-108078
132. J. Porcayo-Calderón, O. Sotelo-Mazón, M. Casales-Diaz, J.A. Ascencio-Gutierrez, V.M. Salinas-Bravo, and L. Martinez-Gomez, Electrochemical Study of Ni20Cr Coatings Applied by HVOF Process in ZnCl2-KCl at High Temperatures, *J. Anal. Methods Chem.*, 2014, **2014**, p 1-10
133. M. Oksa, P. Auerkari, J. Salonen, and T. Varis, Nickel-Based HVOF Coatings Promoting High Temperature Corrosion Resistance of Biomass-Fired Power Plant Boilers, *Fuel Process. Technol.*, 2014, **125**, p 236-245
134. A. Karimi, R. Soltani, M. Ghambari, and H. Fallahdoost, High Temperature Oxidation Resistance of Plasma Sprayed and Surface Treated YSZ Coating on Hastelloy X, *Surf. Coat. Technol.*, 2017, **321**, p 378-385
135. Y.H. Sohn, J.H. Kim, E.H. Jordan, and M. Gell, Thermal Cycling of EB-PVD/MCrAlY Thermal Barrier Coatings: I. Microstructural Development and Spallation Mechanisms, *Surf. Coat. Technol.*, 2001, **146-147**, p 70-78
136. D. Monceau, F. Crabos, A. Malié, and B. Pieraggi, Effects of Bond-Coat Preoxidation and Surface Finish on Isothermal and Cyclic Oxidation, High Temperature Corrosion and Thermal Shock Resistance of TBC Systems, *Materials Science Forum*, 2001. https://www.scientific.net/MSF.369-372.607. Accessed 17 Aug 2018
137. D. Monceau, K. Bouhanek, R. Peraldi, A. Malie, and B. Pieraggi, Transition in High-Temperature Oxidation Kinetics of Pd-Modified Aluminide Coatings: Role of Oxygen Partial Pressure, Heating Rate, and Surface Treatment, *J. Mater. Res.*, 2000, **15**(3), p 665-675
138. J.A. Haynes, M.J. Lance, B.A. Pint, and I.G. Wright, Characterization of Commercial EB-PVD TBC Systems with CVD (Ni, Pt)Al Bond Coatings, *Surf. Coat. Technol.*, 2001, **146-147**, p 140-146
139. S. Laxman, B. Franke, B.W. Kempshall, Y.H. Sohn, L.A. Giannuzzi, and K.S. Murphy, Phase Transformations of Thermally Grown Oxide on (Ni, Pt)Al Bondcoat During Electron Beam Physical Vapor Deposition and Subsequent Oxidation, *Surf. Coat. Technol.*, 2004, **177-178**, p 121-130
140. A.V. Put, D. Oquab, E. Péré, A. Raffaitin, and D. Monceau, Beneficial Effect of Pt and of Pre-Oxidation on the Oxidation Behaviour of an NiCoCrAlYTa Bond-Coating for Thermal Barrier Coating Systems, *Oxid. Met.*, 2011, **75**(5-6), p 247-279
141. V.K. Tolpygo, D.R. Clarke, and K.S. Murphy, The Effect of Grit Blasting on the Oxidation Behavior of a Platinum-Modified Nickel-Aluminide Coating, *Metall. Mater. Trans. A*, 2001, **32**(6), p 1467-1478
142. R. Goyal, B.S. Sidhu, and V. Chawla, Improving the High-Temperature Oxidation Resistance of ASME-SA213-T11 Boiler Tube Steel by Plasma Spraying with CNT-Reinforced Alumina Coatings, *Anti Corros. Methods Mater.*, 2018, **65**(2), p 217-223
143. P. Zhang, et al., Effects of Surface Finish on the Initial Oxidation of HVAF-Sprayed NiCoCrAlY Coatings, *Surf. Coat. Technol.*, 2019, **364**, p 43-56
144. S. Deng, P. Wang, Y. He, and J. Zhang, Surface Microstructure and High Temperature Oxidation Resistance of Thermal Sprayed NiCoCrAlY Bond-Coat Modified by Cathode Plasma Electrolysis, *J. Mater. Sci. Technol.*, 2017, **33**(9), p 1055-1060
145. E. Fernández, J.R. García, J.M. Cuetos, and V. Higuera, Behaviour of Laser Treated Cr, Ni Coatings in the Oxidative Atmosphere of a Steam Boiler, *Surf. Coat. Technol.*, 2005, **195**(1), p 1-7
146. E. Sadeghimeresht, N. Markocsan, and P. Nylén, A Comparative Study of Corrosion Resistance for HVAF-Sprayed Fe- and Co-Based Coatings, *Coatings*, 2016, **6**(2), p 16
147. International Organization for Standardization. ISO 17224:2015 Corrosion of Metals and Alloys—Test Method for High Temperature Corrosion Testing of Metallic Materials by Application of a Deposit of Salt, Ash, Or Other Substances. First Edition 2015-04-15. ISO 17224:2015(E)
148. Y. Kawahara, Evaluation of High-Temperature Corrosion Life Using Temperature Gradient Corrosion Test with Thermal Cycle Component in Waste Combustion Environments, *Mater. Corros.*, 2006, **57**(1), p 60-72
149. M. Oksa, J. Metsäjoki, and J. Kärki, Thermal Spray Coatings for High-Temperature Corrosion Protection in Biomass Co-Fired Boilers, *J. Therm. Spray Technol.*, 2014, **24**(1-2), p 194-205
150. M. Oksa, J. Metsäjoki, and J. Kärki, Corrosion Testing of Thermal Spray Coatings in a Biomass Co-Firing Power Plant, *Coatings*, 2016, **6**(4), p 65
151. N. Bala, H. Singh, S. Prakash, and J. Karthikeyan, Investigations on the Behavior of HVOF and Cold Sprayed Ni-20Cr Coating on T22 Boiler Steel in Actual Boiler Environment, *J. Therm. Spray Technol.*, 2012, **21**(1), p 144-158
152. N. Bala, H. Singh, and S. Prakash, Performance of Cold Sprayed Ni Based Coatings in Actual Boiler Environment, *Surf. Coat. Technol.*, 2017, **318**, p 50-61
153. S.C. Kung and W.T. Bakker, Furnace Wall Corrosion in Reducing—Sulfidizing Combustion Gas, *Mater. High Temp.*, 1997, **14**(2), p 175-182
154. M.A. Uusitalo, P.M.J. Vuoristo, and T.A. Mäntylä, High Temperature Corrosion of Coatings and Boiler Steels in Reducing Chlorine-Containing Atmosphere, *Surf. Coat. Technol.*, 2002, **161**(2), p 275-285
156. M. Oksa, E. Turunen, and T. Varis, Sealing of Thermally Sprayed Coatings, *Surf. Eng.*, 2004, **20**(4), p 251-254
157. D.J. Branagan, M. Breitsameter, B.E. Meacham, and V. Belashchenko, High-Performance Nanoscale Composite Coatings for Boiler Applications, *J. Therm. Spray Technol.*, 2005, **14**(2), p 196-204
158. D. Rezakhani, Corrosion Behaviours of Several Thermal Spray Coatings Used on Boiler Tubes at Elevated Temperatures, *Anti Corros. Methods Mater.*, 2007, **54**(4), p 237-243
159. X.Q. Ma, D.W. Gandy, and G.J. Frederick, Innovation of Ultrafine Structured Alloy Coatings Having Superior Mechanical Properties and High Temperature Corrosion Resistance, *J. Therm. Spray Technol.*, 2008, **17**(5-6), p 933-941
160. K. Tao, X. Zhou, H. Cui, and J. Zhang, Microhardness Variation in Heat-Treated Conventional and Nanostructured NiCrC Coatings Prepared by HVAF Spraying, *Surf. Coat. Technol.*, 2009, **203**(10-11), p 1406-1414
161. M. Torrell, S. Dosta, J.R. Miguel, and J.M. Guilemany, Optimisation of HVOF Thermal Spray Coatings for Their Implementation as MSWI, Superheater Protectors, *Corros. Eng. Sci. Technol.*, 2010, **45**(1), p 84-93
162. G. Kaushal, H. Singh, and S. Prakash, Comparative High Temperature Analysis of HVOF-Sprayed and Detonation Gun

Sprayed Ni-20Cr Coating in Laboratory and Actual Boiler Environments, *Oxid. Met.*, 2011, **76**(3-4), p 169-191
166. M. Oksa, J. Metsäjoki, and J. Kärki, Thermal Spray Coatings for High-Temperature Corrosion Protection in Biomass Co-fired Boilers, *J. Therm. Spray Technol.*, 2015, **24**(1-2), p 194-205
170. B. Song, K.T. Voisey, and T. Hussain, High Temperature Chlorine-Induced Corrosion of Ni50Cr Coating: HVOLF, HVOGF, Cold Spray and Laser Cladding, *Surf. Coat. Technol.*, 2018, **337**, p 357-369
173. M.A. Uusitalo, P.M.J. Vuoristo, and T.A. Mäntylä, High Temperature Corrosion of Coatings and Boiler Steels Below Chlorine-Containing Salt Deposits, *Corros. Sci.*, 2004, **46**(6), p 1311-1331
174. B. Song, Z. Pala, K.T. Voisey, and T. Hussain, Gas and Liquid-Fuelled HVOF Spraying of Ni50Cr Coating: Microstructure and High Temperature Oxidation, *Surf. Coat. Technol.*, 2017, **318**, p 224-232
175. D. Fantozzi, V. Matikainen, M. Uusitalo, H. Koivuluoto, and P. Vuoristo, Chlorine Induced High-Temperature Corrosion Mechanisms in HVOF and HVAF Sprayed Cr3C2-Based Hardmetal Coatings, *Corros. Sci.*, 2019, **160**, p 108-166
176. J. Lehmusto, P. Yrjas, and L. Hupa, Pre-oxidation as a Means to Increase Corrosion Resistance of Commercial Superheater Steels, *Oxid. Met.*, 2019, **91**(3), p 311-326
177. J. Lehmusto, D. Lindberg, P. Yrjas, B.-J. Skrifvars, and M. Hupa, Studies on the Partial Reactions Between Potassium Chloride and Metallic Chromium Concerning Corrosion at Elevated Temperatures, *Oxid. Met.*, 2012, **77**(3), p 129-148
178. L.A. Giannuzzi, Ed., *Introduction to Focused Ion Beams: Instrumentation, Theory*, Techniques and Practice. Springer, US, 2005
179. T.L. Burnett et al., Large Volume Serial Section Tomography by Xe Plasma FIB Dual Beam Microscopy, *Ultramicroscopy*, 2016, **161**, p 119-129
180. V. Katranidis, S. Gu, D.C. Cox, M.J. Whiting, and S. Kamnis, FIB-SEM Sectioning Study of Decarburization Products in the Microstructure of HVOF-Sprayed WC-Co Coatings, *J. Therm. Spray Technol.*, 2018, **27**(5), p 898-908
181. J.C. Pereira, J.C. Zambrano, M.J. Tobar, A. Yañez, and V. Amigó, High Temperature Oxidation Behavior of Laser Cladding MCrAlY Coatings on Austenitic Stainless Steel, *Surf. Coat. Technol.*, 2015, **270**, p 243-248
182. X. Song et al., Advanced Analysis on Growth Mechanisms of Thermally Grown Oxide at Elevated Temperature for Thermal Barrier Coatings, *Vacuum*, 2016, **134**, p 33-39
183. Y. Zou, W. Qin, E. Irissou, J.-G. Legoux, S. Yue, and J.A. Szpunar, Dynamic Recrystallization in the Particle/Particle Interfacial Region of Cold-Sprayed Nickel Coating: Electron Backscatter Diffraction Characterization, *Scr. Mater.*, 2009, **61**(9), p 899-902
184. D. Brandon and W.D. Kaplan, *Microstructural Characterization of Materials*, Wiley, Hoboken, 2013
185. T. Mori, S. Kuroda, H. Murakami, H. Katanoda, Y. Sakamoto, and S. Newman, Effects of Initial Oxidation on β Phase Depletion and Oxidation of CoNiCrAlY Bond Coatings Fabricated by Warm Spray and HVOF Processes, *Surf. Coat. Technol.*, 2013, **221**, p 59-69
186. J.-J. Tian, S.-W. Yao, X.-T. Luo, C.-X. Li, and C.-J. Li, An Effective Approach for Creating Metallurgical Self-Bonding in Plasma-Spraying of NiCr-Mo Coating by Designing Shell-Core-Structured Powders, *Acta Mater.*, 2016, **110**, p 19-30
187. A. Manap, A. Nakano, and K. Ogawa, The Protectiveness of Thermally Grown Oxides on Cold Sprayed CoNiCrAlY Bond Coat in Thermal Barrier Coating, *J. Therm. Spray Technol.*, 2012, **21**(3-4), p 586-596
188. W. Zhou, K. Zhou, C. Deng, K. Zeng, and Y. Li, Hot Corrosion Behaviour of HVOF-Sprayed Cr3C2-NiCrMoNbAl Coating, *Surf. Coat. Technol.*, 2017, **309**, p 849-859
189. W. Zhou, K. Zhou, C. Deng, K. Zeng, and Y. Li, Hot Corrosion Behavior of HVOF-Sprayed Cr3C2-WC-NiCoCrMo Coating, *Ceram. Int.*, 2017, **43**(12), p 9390-9400
190. D. Mudgal, L. Ahuja, S. Singh, and S. Prakash, Corrosion Behaviour of Cr3C2-NiCr Coated Superalloys Under Actual Medical Waste Incinerator, *Surf. Coat. Technol.*, 2017, **325**, p 145-156
191. H. Singh and H. Khosla, Comparative Evaluation of Performance of Cold Sprayed and Bare N06601 Superalloy in Medical Waste Incinerator at 900 °C, *Mater. Chem. Phys.*, 2017, **200**, p 57-69
192. M.H. Enayati, F. Karimzadeh, M. Tavoosi, B. Movahedi, and A. Tahvilian, Nanocrystalline NiAl Coating Prepared by HVOF Thermal Spraying, *J. Therm. Spray Technol.*, 2010, **20**(3), p 440-446
193. S.T. Bluni and A.R. Marder, Effects of Thermal Spray Coating Composition and Microstructure on Coating Response and Substrate Protection at High Temperatures, *CORROSION*, 1996, **52**(3), p 213-218
195. B.B. He, *Two-Dimensional X-ray diffraction*, Wiley, Hoboken, 2011
196. T. Wiederkehr, B. Klusemann, D. Gies, H. Müller, and B. Svendsen, An Image Morphing Method for 3D Reconstruction and FE-Analysis of Pore Networks in Thermal Spray Coatings, *Comput. Mater. Sci.*, 2010, **47**(4), p 881-889
197. N. Asadizanjani, S. Shahbazmohamadi, and E. H. Jordan, Investigation of Surface Geometry Thermal Barrier Coatings using Computed X-Ray Tomography, in *Developments in Strategic Materials and Computational Design V: A Collection of Papers Presented at the 38th International Conference on Advanced Ceramics and Composites January 27-31, 2014 Daytona Beach, Florida*, 2014, vol 35, p 175-187
198. V. Viswanathan, R. Filmalter, S. Patil, S. Deshpande, and S. Seal, High-Temperature Oxidation Behavior of Solution Precursor Plasma Sprayed Nanoceria Coating on Martensitic Steels, *J. Am. Ceram. Soc.*, 2007, **90**(3), p 870-877
199. V. Singh, *Rare Earth Oxide Coating with Controlled Chemistry Using Thermal Spray*, Electronic Theses and Dissertations, 2012
200. S. Hofmann, *Auger- and X-Ray Photoelectron Spectroscopy in Materials Science: A User-Oriented Guide*, Springer, Berlin, 2012
201. C.M. Mahoney, *Cluster Secondary Ion Mass Spectrometry: Principles and Applications*, Wiley, Hoboken, 2013
202. S. Fearn, *An Introduction to Time-of-Flight Secondary Ion Mass Spectrometry (ToF-SIMS) and Its Application to Materials Science*, Morgan & Claypool Publishers, San Rafael, 2015
203. S.D. Zhang, J. Wu, W.B. Qi, and J.Q. Wang, Effect of Porosity Defects on the Long-Term Corrosion Behaviour of Fe-Based Amorphous Alloy Coated Mild Steel, *Corros. Sci.*, 2016, **110**, p 57-70
204. J. Wu, S.D. Zhang, W.H. Sun, Y. Gao, and J.Q. Wang, Enhanced Corrosion Resistance in Fe-Based Amorphous Coatings Through Eliminating Cr-Depleted Zones, *Corros. Sci.*, 2018, **136**, p 161-173
205. D.B. Williams and C.B. Carter, *Transmission Electron Microscopy: A Textbook for Materials Science*, Springer, Berlin, 2009
206. P. Poza, J. Gómez-García, and C.J. Múnez, TEM Analysis of the Microstructure of Thermal Barrier Coatings After Isothermal Oxidation, *Acta Mater.*, 2012, **60**(20), p 7197-7206
207. Y.-M. Zou, Y.-S. Wu, J.-Z. Wang, Z.G. Qiu, and D.C. Zeng, Preparation, Mechanical Properties and Cyclic Oxidation Behavior of the Nanostructured NiCrCoAlY-TiB2 Coating, *Ceram. Int.*, 2018, **44**(16), p 19362-19369

208. P.R. Griffiths and J.A.D. Haseth, *Fourier Transform Infrared Spectrometry*, Wiley, Hoboken, 2007
209. J.R. Ferraro, *Introductory Raman Spectroscopy*, Elsevier, Amsterdam, 2003
210. C. Zhu, X. Wu, Y. Wu, and G. Liang, The Effect of Initial Oxidation on Long-Term Oxidation of NiCoCrAlY Alloy, *Engineering*, 2010, **02**, p 602
211. H.-S. Lee, J.K. Singh, M.A. Ismail, and C. Bhattacharya, Corrosion Resistance Properties of Aluminum Coating Applied by Arc Thermal Metal Spray in SAE J2334 Solution with Exposure Periods, *Metals*, 2016, **6**(3), p 55
212. M. Subanovic et al., Effect of Manufacturing Related Parameters on Oxidation Properties of MCrAlY-Bondcoats, *Mater. Corros.*, 2008, **59**(6), p 463-470
213. Y. Ding, T. Hussain, and D.G. McCartney, High-Temperature Oxidation of HVOF Thermally Sprayed NiCr-$Cr_3C_2$ Coatings: Microstructure and Kinetics, *J. Mater. Sci.*, 2015, **50**(20), p 6808-6821
214. Y. Chen, X. Fan, Y. Sun, and W. Zhang, Effect of Tensile Load on High Temperature Oxidation of CoNiCrAlY Coating, *Surf. Coat. Technol.*, 2018, **352**, p 399-405
215. A. Gil et al., Y-Rich Oxide Distribution in Plasma Sprayed MCrAlY-Coatings Studied by SEM with a Cathodoluminescence Detector and Raman Spectroscopy, *Surf. Coat. Technol.*, 2009, **204**(4), p 531-538
216. V. Teixeira, M. Andritschky, W. Fischer, H.P. Buchkremer, and D. Stöver, Effects of Deposition Temperature and Thermal Cycling on Residual Stress State in Zirconia-Based Thermal Barrier Coatings, *Surf. Coat. Technol.*, 1999, **120-121**, p 103-111
217. V. Teixeira, M. Andritschky, W. Fischer, and D. Stöver, Residual Stresses in PVD/Plasma Sprayed Thermal Barrier Multilayered Coatings at High Temperature, in *Advanced Multilayered and Fibre-Reinforced Composites*, Springer, Dordrecht, 1998, p 415-430
218. D. Stokes, *Principles and Practice of Variable Pressure/Environmental Scanning Electron Microscopy (VP-ESEM)*, Wiley, Hoboken, 2008
219. A.A. Boudi, M.S.J. Hashmi, and B.S. Yilbas, ESEM Evaluation of Inconel-625 Thermal Spray Coating (HVOF) Onto Stainless Steel and Carbon Steel Post Brine Exposure After Tensile Tests, *J. Mater. Process. Technol.*, 2006, **173**(1), p 44-52
220. S.J.B. Reed, Electron Probe Microanalysis, *Microprobe Techniques in the Earth Sciences*, P.J. Potts, J.F.W. Bowles, S.J.B. Reed, and M.R. Cave, Ed., Springer US, Boston, 1995, p 49-89
221. H. Singh, D. Puri, and S. Prakash, High Temperature Oxidation Behaviour of Plasma Sprayed NiCrAlY Coatings on Ni-Based Superalloys in Air, *Trans. Indian Inst. Met.*, 2005, **59**, p 215-227
222. P.-C. Tsai and C.-S. Hsu, High Temperature Corrosion Resistance and Microstructural Evaluation of Laser-Glazed Plasma-Sprayed Zirconia/MCrAlY Thermal Barrier Coatings, *Surf. Coat. Technol.*, 2004, **183**(1), p 29-34
223. H. Singh, D. Puri, and S. Prakash, Some Studies on Hot Corrosion Performance of Plasma Sprayed Coatings on a Fe-Based Superalloy, *Surf. Coat. Technol.*, 2005, **192**(1), p 27-38
224. T. Sundararajan, S. Kuroda, J. Kawakita, and S. Seal, High Temperature Corrosion of Nanoceria Coated 9Cr-1Mo Ferritic Steel in Air and Steam, *Surf. Coat. Technol.*, 2006, **201**(6), p 2124-2130
225. L. Krumm and M. C. Galetz, Impact of Deposits and Their Morphology on the Active Corrosion of Iron in Chlorine- and Sulfur-Containing Atmospheres in the Temperature Range of 350-500 °C, *Oxid Met.*, 2018, **90**(3-4), p 365-381
226. S. Osgerby and T. Fry, Laboratory Test Procedures for Exposure to High Temperature Steam Atmospheres, *Measurement Good Practice Guide No. 74, National Physical Laboratory, Teddington*, vol. 74, 2005
227. S.R.J. Saunders, M. Monteiro, and F. Rizzo, The Oxidation Behaviour of Metals and Alloys at High Temperatures in Atmospheres Containing Water Vapour: A Review, *Prog. Mater Sci.*, 2008, **53**(5), p 775-837
228. D.J. Young, D. Naumenko, L. Niewolak, E. Wessel, L. Singheiser, and W.J. Quadakkers, Oxidation Kinetics of Y-Doped FeCrAl-Alloys in Low and High pO2 Gases, *Mater. Corros.*, 2010, **61**(10), p 838-844
229. C. Shen, Z. Pan, Y. Ma, D. Cuiuri, and H. Li, Fabrication of Iron-Rich Fe-Al Intermetallics Using the Wire-Arc Additive Manufacturing Process, *Addit. Manuf.*, 2015, **7**, p 20-26
230. S.-G. Liu, J.-M. Wu, S.-C. Zhang, S.-J. Rong, and Z.-Z. Li, High Temperature Erosion Properties of Arc-Sprayed Coatings Using Various Cored Wires Containing Ti-Al Intermetallics, *Wear*, 2007, **262**(5), p 555-561
231. B. Xu, Z. Zhu, S. Ma, W. Zhang, and W. Liu, Sliding Wear Behavior of Fe-Al and Fe-Al/WC Coatings Prepared by High Velocity Arc Spraying, *Wear*, 2004, **257**(11), p 1089-1095
232. C. Senderowski, Z. Bojar, W. Wołczyński, and A. Pawłowski, Microstructure Characterization of D-Gun Sprayed Fe-Al Intermetallic Coatings, *Intermetallics*, 2010, **18**(7), p 1405-1409
233. J.A. Hearley, J.A. Little, and A.J. Sturgeon, The Erosion Behaviour of NiAl Intermetallic Coatings Produced by High Velocity Oxy-Fuel Thermal Spraying, *Wear*, 1999, **233-235**, p 328-333
234. C. Shang, E. Axinte, W. Ge, Z. Zhang, and Y. Wang, High-Entropy Alloy Coatings with Excellent Mechanical, Corrosion Resistance and Magnetic Properties Prepared by Mechanical Alloying and Hot Pressing Sintering, *Surf. Interfaces*, 2017, **9**, p 36-43
235. X.-R. Wang, Z.-Q. Wang, P. He, T.-S. Lin, and Y. Shi, Microstructure and Wear Properties of CuNiSiTiZr High-Entropy Alloy Coatings on TC11 Titanium Alloy Produced by Electrospark—Computer Numerical Control Deposition Process, *Surf. Coat. Technol.*, 2015, **283**, p 156-161
236. X.W. Qiu, Y.P. Zhang, and C.G. Liu, Effect of Ti Content on Structure and Properties of Al2CrFeNiCoCuTix High-Entropy Alloy Coatings, *J. Alloys Compd.*, 2014, **585**, p 282-286
237. M.P. Brady and P.F. Tortorelli, Alloy Design of Intermetallics for Protective Scale Formation and for Use as Precursors for Complex Ceramic Phase Surfaces, *Intermetallics*, 2004, **12**(7), p 779-789
238. A. Lasalmonie, Intermetallics: Why is it so Difficult to Introduce Them in Gas Turbine Engines?, *Intermetallics*, 2006, **14**(10), p 1123-1129
239. B. Lesage, L. Maréchal, A.M. Huntz, and R. Molins, Aluminium Depletion in FeCrAl Alloys During Oxidation, *Defect Diffus. Forum*, 2001, **194**, p 1707-1712
240. G. Merceron, R. Molins, and J.L. Strudel, Oxidation Behaviour and Microstructural Evolution of FeCrAl ODS Alloys at High Temperature, *Mater. High Temp.*, 2000, **17**(1), p 149-157
241. F. Lang, Z. Yu, S. Gedevanishvili, S.C. Deevi, and T. Narita, Isothermal Oxidation Behavior of a Sheet Alloy of Fe-40at.% Al at Temperatures Between 1073 and 1473 K, *Intermetallics*, 2003, **11**(7), p 697-705
242. R. Sakidja, J.S. Park, J. Hamann, and J.H. Perepezko, Synthesis of Oxidation Resistant Silicide Coatings on Mo-Si-B Alloys, *Scr. Mater.*, 2005, **53**(6), p 723-728
243. E. Gaffet and G. Le Caër, Mechanical Processing for Nanomaterials, in *Encyclopedia of nanoscience and Nanotechnology*, vol. 5, American Scientific Publishers Stevenson Ranch, calif, USA, 2004, p 91-129
244. P. Juzoń, M. Ziemnicka, S. Chevalier, K. Przybylski, and J.P. Larpin, Improving Fe3Al Alloy Resistance Against High

Temperature Oxidation by Pack Cementation process, *Appl. Surf. Sci.*, 2007, **253**(11), p 4928-4934
245. Y. Liu, C. Cheng, J. Shang, R. Wang, P. Li, and J. Zhao, Oxidation Behavior of High-Entropy Alloys AlxCoCrFeNi (x = 0.15, 0.4) in Supercritical Water and Comparison with HR3C Steel, *Trans. Nonferrous Met. Soc. China*, 2015, **25**(4), p 1341-1351
246. W.-L. Hsu, H. Murakami, J.-W. Yeh, A.-C. Yeh, and K. Shimoda, On the Study of Thermal-Sprayed Ni0.2Co0.6-Fe0.2CrSi0.2AlTi0.2 HEA Overlay Coating, *Surf. Coat. Technol.*, 2017, **316**, p 71-74
247. S.R. Cross, R. Woollam, S. Shademan, and C.A. Schuh, Computational Design and Optimization of Multilayered And Functionally Graded Corrosion Coatings, *Corros. Sci.*, 2013, **77**, p 297-307
248. S. Nath, I. Manna, and J.D. Majumdar, Kinetics and Mechanism of Isothermal Oxidation of Compositionally Graded Yttria Stabilized Zirconia (YSZ) Based Thermal Barrier Coating, *Corros. Sci.*, 2014, **88**, p 10-22
249. Z. Bergant, U. Trdan, and J. Grum, Effect of High-Temperature Furnace Treatment on the Microstructure and Corrosion Behavior of NiCrBSi Flame-Sprayed Coatings, *Corros. Sci.*, 2014, **88**, p 372-386
250. X. Chen, Y. Zhao, L. Gu, B. Zou, Y. Wang, and X. Cao, Hot Corrosion Behaviour of Plasma Sprayed YSZ/$LaMgAl_{11}O_{19}$ Composite Coatings in Molten Sulfate-Vanadate Salt, *Corros. Sci.*, 2011, **53**(6), p 2335-2343
251. G. Sreedhar and V.S. Raja, Hot Corrosion of YSZ/Al 2 O 3 Dispersed NiCrAlY Plasma-Sprayed Coatings in $Na_2SO_4$-10wt.% NaCl Melt, *Corros. Sci.*, 2010, **52**(8), p 2592-2602
252. C.R.C. Lima, N. Cinca, and J.M. Guilemany, Study of the High Temperature Oxidation Performance of Thermal Barrier Coatings with HVOF Sprayed Bond Coat and Incorporating a PVD Ceramic Interlayer, *Ceram. Int.*, 2012, **38**(8), p 6423-6429
253. S. Stewart, R. Ahmed, and T. Itsukaichi, Contact Fatigue Failure Evaluation of Post-treated WC-NiCrBSi Functionally Graded Thermal Spray Coatings, *Wear*, 2004, **257**(9), p 962-983
254. U. Schulz, M. Peters, F.-W. Bach, and G. Tegeder, Graded Coatings for Thermal, Wear and Corrosion Barriers, *Mater. Sci. Eng. A*, 2003, **362**(1), p 61-80
255. M. Bhattacharyya, A.N. Kumar, and S. Kapuria, Synthesis and Characterization of Al/SiC and Ni/$Al_2O_3$ Functionally Graded Materials, *Mater. Sci. Eng. A*, 2008, **487**(1), p 524-535
256. A. Valarezo et al., Damage Tolerant Functionally Graded WC-Co/Stainless Steel HVOF Coatings, *Surf. Coat. Technol.*, 2010, **205**(7), p 2197-2208
257. S. Björklund, S. Goel, and S. Joshi, Function-Dependent Coating Architectures by Hybrid Powder-Suspension Plasma Spraying: Injector Design, Processing and Concept Validation, *Mater. Des.*, 2018, **142**, p 56-65
258. P.S. Mohanty, A.D. Roche, R.K. Guduru, and V. Varadaraajan, Ultrafine Particulate Dispersed High-Temperature Coatings by Hybrid Spray Process, *J. Therm. Spray Technol.*, 2010, **19**(1-2), p 484-494
259. A. Moridi, S.M. Hassani-Gangaraj, M. Guagliano, and M. Dao, Cold Spray Coating: Review of Material Systems and Future Perspectives, *Surf. Eng.*, 2014, **30**(6), p 369-395
260. A. Bahrami, N. Soltani, M.I. Pech-Canul, and C.A. Gutiérrez, Development of Metal-Matrix Composites from Industrial/Agricultural Waste Materials and Their Derivatives, *Crit. Rev. Environ. Sci. Technol.*, 2016, **46**(2), p 143-208
261. S. Matthews, B. James, and M. Hyland, High Temperature Erosion-Oxidation of $Cr_3C_2$-NiCr Thermal Spray Coatings Under Simulated Turbine Conditions, *Corros. Sci.*, 2013, **70**, p 203-211
262. A. Martínez-Villafañe, F.H. Stott, J.G. Chacon-Nava, and G.C. Wood, Enhanced Oxygen Diffusion Along Internal Oxide-Metal Matrix Interfaces in Ni-Al Alloys During Internal Oxidation, *Oxid. Met.*, 2002, **57**(3), p 267-279
263. C.-J. Li, G.-J. Yang, P.-H. Gao, J. Ma, Y.-Y. Wang, and C.-X. Li, Characterization of Nanostructured WC-Co Deposited by Cold Spraying, *J. Therm. Spray Technol.*, 2007, **16**(5-6), p 1011-1020
264. K. Tao, X.-L. Zhou, H. Cui, and J.-S. Zhang, Oxidation and Hot Corrosion Behaviors of HVAF-Sprayed Conventional and Nanostructured NiCrC Coatings, *Trans. Nonferrous Met. Soc. China*, 2009, **19**(5), p 1151-1160
265. Y. Wu, P. Lin, G. Xie, J. Hu, and M. Cao, Formation of Amorphous and Nanocrystalline Phases in High Velocity Oxy-Fuel Thermally Sprayed a Fe-Cr-Si-B-Mn Alloy, *Mater. Sci. Eng. A*, 2006, **430**(1-2), p 34-39
266. W. Guo et al., Fabrication and Characterization of Thermal-Sprayed Fe-Based Amorphous/Nanocrystalline Composite Coatings: An Overview, *J. Therm. Spray Technol.*, 2014, **23**(7), p 1157-1180
267. M.L. Lau, H.G. Jiang, W. Nüchter, and E.J. Lavernia, Thermal Spraying of Nanocrystalline Ni Coatings, *physica status solidi (a)*, 1998, **166**(1), p 257-268
268. J. Pettersson, J.-E. Svensson, and L.-G. Johansson, KCl-Induced Corrosion of a 304-Type Austenitic Stainless Steel in $O_2$ and in $O_2 + H_2O$ Environment: The Influence of Temperature, *Oxid. Met.*, 2009, **72**(3-4), p 159-177
269. S.S. Chatha, H.S. Sidhu, and B.S. Sidhu, The Effects of Post-treatment on the Hot Corrosion Behavior of the HVOF-Sprayed Cr3C2-NiCr Coating, *Surf. Coat. Technol.*, 2012, **206**(19), p 4212-4224
270. G. Bolelli, L. Lusvarghi, and M. Barletta, Heat Treatment Effects on the Corrosion Resistance of Some HVOF-Sprayed Metal Alloy Coatings, *Surf. Coat. Technol.*, 2008, **202**(19), p 4839-4847
271. D. Das, R. Balasubramaniam, and M.N. Mungole, Hot Corrosion of Carbon-Alloyed Fe3Al-Based Iron Aluminides, *Mater. Sci. Eng. A*, 2002, **338**(1), p 24-32
272. N. Espallargas, J. Berget, J.M. Guilemany, A.V. Benedetti, and P.H. Suegama, Cr3C2-NiCr and WC-Ni Thermal Spray Coatings as Alternatives to Hard Chromium for Erosion-Corrosion Resistance, *Surf. Coat. Technol.*, 2008, **202**(8), p 1405-1417
273. R.Q. Guo, C. Zhang, Q. Chen, Y. Yang, N. Li, and L. Liu, Study of Structure and Corrosion Resistance of Fe-Based Amorphous Coatings Prepared by HVAF and HVOF, *Corros. Sci.*, 2011, **53**(7), p 2351-2356
274. J.M. Guilemany, N. Espallargas, P.H. Suegama, and A.V. Benedetti, Comparative Study of Cr3C2-NiCr Coatings Obtained by HVOF and Hard Chromium Coatings, *Corros. Sci.*, 2006, **48**(10), p 2998-3013
275. V. Swaminathan, H. Zeng, D. Lawrynowicz, Z. Zhang, and J.L. Gilbert, Electrochemical Investigation of Chromium Nanocarbide Coated Ti-6Al-4V and Co-Cr-Mo Alloy Substrates, *Electrochim. Acta*, 2012, **59**, p 387-397
276. J. Porcayo-Calderon, O. Sotelo-Mazon, V.M. Salinas-Bravo, C.D. Arrieta-Gonzalez, J.J. Ramos-Hernandez, and C. Cuevas-Arteaga, Electrochemical Performance of Ni20Cr Coatings Applied by Combustion Powder Spray in ZnCl2-KCl Molten Salts, *Int. J. Electrochem. Sci.*, 2012, **7**(2), p 1134-1148
277. S.C. Okoro, M. Montgomery, F.J. Frandsen, and K. Pantleon, Time and Temperature Effects on Alkali Chloride Induced High Temperature Corrosion of Superheaters during Biomass Firing, *Energy Fuels*, 2018, **32**(7), p 7991-7999
278. M.D. Paz, D. Zhao, S. Karlsson, J. Liske, and T. Jonsson, Investigating Corrosion Memory: The Influence of Previous

Boiler Operation on Current Corrosion Rate, *Fuel Process. Technol.*, 2017, **156**, p 348-356
279. S.V. Lamaka, M.L. Zheludkevich, K.A. Yasakau, R. Serra, S.K. Poznyak, and M.G.S. Ferreira, Nanoporous Titania Interlayer as Reservoir of Corrosion Inhibitors for Coatings with Self-healing Ability, *Prog. Org. Coat.*, 2007, **58**(2-3), p 127-135
280. M. Nosonovsky, R. Amano, J.M. Lucci, and P.K. Rohatgi, Physical Chemistry of Self-organization and Self-healing in Metals, *Phys. Chem. Chem. Phys.*, 2009, **11**(41), p 9530-9536
281. D.V. Andreeva, D. Fix, H. Möhwald, and D.G. Shchukin, Self-healing Anticorrosion Coatings Based on pH-Sensitive Polyelectrolyte/Inhibitor Sandwichlike Nanostructures, *Adv. Mater.*, 2008, **20**(14), p 2789-2794
282. T. Ouyang et al., Enhancement of High Temperature Oxidation Resistance and Spallation Resistance of SiC-Self-healing Thermal Barrier Coatings, *Surf. Coat. Technol.*, 2016, **286**, p 365-375
283. S.V.S. Raj, M. Singh, and R.T. Bhatt, High Temperature Lightweight Self-Healing Ceramic Composites for Aircraft Engine Applications, Report (2014-218352), National Aeronautics and Space Administration (NASA), 2014
284. C. Wang, K. Li, X. Shi, J. Sun, Q. He, and C. Huo, Self-healing YSZ-La-Mo-Si Heterogeneous Coating Fabricated by Plasma Spraying to Protect Carbon/Carbon Composites from Oxidation, *Compos. B Eng.*, 2017, **125**, p 181-194
285. A. Atkinson, Surface and Interface Mass Transport in Ionic Materials, *Solid State Ion.*, 1988, **28-30**, p 1377-1387